

Towards high-resolution and high-contrast  
imaging in mid-infrared astronomy  
Integrated optics beam combiners for astrointerferometry

INAUGURAL-DISSERTATION

zur  
Erlangung des Doktorgrades  
der Mathematisch-Naturwissenschaftlichen Fakultät  
der Universität zu Köln



vorgelegt von

**Jan Tepper**  
geboren in Geseke

Köln 2017

Berichterstatter (Gutachter):  
Prof. dr. Lucas Labadie  
Prof. dr. ir. Paul H. M. van Loosdrecht

Tag der mündlichen Prüfung:  
Dezember 2017

## Abstract

Research in astronomical instrumentation is driven by open questions about the structure of our universe and its constituents, such as black holes, the interstellar medium, stars and planets. This work is focused on a particular observation technique called astronomical interferometry for the infrared. In contrast to conventional single telescopes, an astronomical interferometer consists of multiple individual telescopes whose light is combined. From the interferometric signals between pairs of telescopes, information about the spatial structure of the observed source can be extracted. The advantage of this technique is its superior angular resolution that is given by  $\lambda/(2B)$ , with  $\lambda$  being the observed wavelength and  $B$  the separation of the telescopes, compared to  $\lambda/D$  for a single telescope with  $D$  being the diameter of the telescope. Therefore, current interferometers with baselines of up to a few hundred meters surpass the resolution capabilities of the largest optical single telescopes ( $D \approx 10$  m) by more than an order of magnitude. Until now, astronomical interferometry has produced results with unprecedented resolution measuring the photospheres of stars, separations of binaries, the close environment of the black hole at the center of our galaxy and the birth regions of exoplanets. On the other hand, the astronomical interferometer is a highly complex apparatus that requires dedicated instrumentation efforts in order to combine and measure stabilized and finely calibrated interferometric signals arising from distant astronomical targets between telescopes more than a hundred meters apart. The precise measurement of the interferometric observables, visibility and phase, are the prerequisite in order to unambiguously reconstruct the morphology of the observed object.

This work is concerned with instrumentation for mid-infrared (mid-IR) astrointerferometry, in the following specified as the 3-5  $\mu\text{m}$  wavelength range. The mid-IR is a region of high scientific interest as it allows to probe cooler regions than stars such as planet forming regions. In fact, this region is considered to be the sweet spot for exoplanet detection due to the planets' stronger emission at these wavelengths and the decreased stellar flux leading to a favorable contrast. For this wavelength region, we aim to develop integrated optics chips to combine the light from the individual telescopes to read out their interferometric signals. Integrated optics chips, similarly to electronic integrated circuits for electrons, can route, split and combine photons in a palm-size device providing a compact and stable instrumental transfer function. Compared to conventional bulk optics beam combination designs, integrated optics deliver much more accurately calibrated interferometric observables. Such photonic devices have not been available in the mid-IR, which is why current facilities until now had to rely on classical bulk optics beam combination schemes, degrading the potential scientific return of the interferometer. The goal of this thesis is the characterization of several integrated optics chips for the mid-IR range using different materials and beam combination designs, and testing their critical properties for astronomical applications.

To this end, I set up an optical testbench in Cologne allowing the interferometric testing of integrated optics beam combiners in the mid-IR. In the first two publications, I characterize two-telescope integrated optics combiners and assess their relevant properties to astronomy such as transmission, modal behavior, splitting ratio as well as dispersion and polarization properties. Most importantly, I experimentally demonstrate for the first time that high interferometric contrasts ( $>93\%$ ) in integrated optics can indeed be achieved in the mid-IR over broad wavelength ranges. This characterization was carried out for two different integrated optics platforms, a chalcogenide glass (GLS) in the first paper and a fluoride glass (ZBLAN) in the second paper, with the second paper

putting an extra focus on the comparison between the two platforms. The ultimate goal is the on-chip combination of four or more telescopes. The third paper goes beyond classical two-telescope beam combiners and more advanced architectures such as so-called ABCD combiners and four-telescope discrete beam combiners are investigated. It is experimentally demonstrated that those couplers are suited for retrieving the visibilities between monochromatic input light fields. This proof-of-concept study paves the way towards a four-telescope combiner. Finally, on the basis of the experimental results, the feasibility and performance of a four-telescope integrated optics based beam combiner instrument is discussed.

## Zusammenfassung

Die Forschung in der astronomischen Instrumentierung wird von offenen Fragen über die Struktur unseres Universums und seiner Bestandteile wie schwarze Löcher, das interstellare Medium, Sterne und Planeten angetrieben. Diese Arbeit beschäftigt sich mit einer speziellen Beobachtungsmethode, die astronomische Interferometrie für Infrarot. Ein astronomisches Interferometer besteht im Gegensatz zu konventionellen einzelnen Teleskopen aus mehreren Teleskopen, deren Licht kombiniert wird. Aus den interferometrischen Signalen zwischen den Teleskopen können Informationen über die Struktur des beobachteten Objekts extrahiert werden. Der Vorteil dieser Technik liegt in ihrer überragenden Winkelauflösung, die durch  $\lambda/(2B)$  gegeben ist, wobei  $\lambda$  die beobachtete Wellenlänge und  $B$  der Abstand ('Baselines') der Teleskope ist, verglichen mit  $\lambda/D$  für ein einzelnes Teleskop, wobei  $D$  der Durchmesser des einzelnen Teleskops ist. Daher übertreffen derzeitige Interferometer mit Baselines von bis zu einigen hundert Metern die Auflösungsfähigkeiten der größten optischen Einzelteleskope ( $D \approx 10$  m) um mehr als eine Größenordnung. Bis jetzt hat die astronomische Interferometrie Ergebnisse mit einer beispiellosen Auflösung geliefert wie die Photosphären von Sternen, Separationen von Binärsystemen, die Umgebung des Schwarzen Lochs im Zentrum unserer Galaxie und die Geburtsregionen von Exoplaneten. Auf der anderen Seite ist das astronomische Interferometer ein hochkomplexer Apparat, der besondere Anstrengungen im Bereich der Instrumentierung erfordert, um stabilisierte und fein kalibrierte interferometrische Signale zu kombinieren und zu messen, die von entfernten astronomischen Objekten zwischen Teleskopen über hundert Meter voneinander entfernt aufgenommen werden. Die genaue Messung der interferometrischen Observablen, Kontrast und Phase, ist die Voraussetzung, um die Morphologie des beobachteten Objekts eindeutig rekonstruieren zu können.

Diese Arbeit befasst sich mit der Instrumentierung für die Astrominterferometrie im mittleren Infrarotbereich (mid-IR), im Folgenden als 3-5  $\mu$ m Wellenlängenbereich festgelegt. Der mid-IR Bereich ist eine Region von hohem wissenschaftlichem Interesse, da sie es ermöglicht, kühlere Regionen als Sterne zu erforschen wie zum Beispiel Planeten bildende Regionen. Tatsächlich wird diese Region aufgrund der stärkeren Emission der Planeten bei diesen Wellenlängen und der gleichzeitig verringerten stellaren Emission als günstiger Bereich für die Detektion von Exoplaneten angesehen. Für diesen Wellenlängenbereich wollen wir integrierte Optiken entwickeln, um das Licht der einzelnen Teleskope zu kombinieren, um ihre interferometrischen Signale auszulesen. Integrierte Optiken können, ähnlich wie elektronische integrierte Schaltkreise für Elektronen, Photonen in einem wenige Zentimeter großen Gerät leiten und kombinieren, was zu einem kompakten und stabileren Instrument führt. Im Vergleich zu konventionellen Bulk-Optik Setups, d.h. mithilfe von Strahlteilern, liefert die integrierte Optik genauer kalibrierte interferometrische Observablen. Solche photonischen Chips waren im mid-IR Bereich nicht verfügbar, weshalb bisherige Instrumente auf klassische Bulk-Optiken angewiesen waren, die die Leistung des Interferometers degradieren. Das Ziel dieser Arbeit ist die Charakterisierung mehrerer integrierter Optiken für den mid-IR Bereich unter Verwendung verschiedener Materialien und Strahlkombinationsdesigns.

Zu diesem Zweck habe ich in Köln eine optische Testbench eingerichtet, die interferometrische Tests von integrierten Optiken zum Kombinieren von Strahlen im mid-IR ermöglicht. In den ersten beiden Publikationen charakterisiere ich integrierte Optiken für die Kombination von zwei Teleskopen und teste ihre relevanten Eigenschaften für Astronomie wie Transmission, modales Verhalten, Teilungsverhältnis sowie Dispersions-

und Polarisationsseigenschaften. Insbesondere demonstriere ich zum ersten Mal experimentell, dass hohe Interferometrie-Kontraste ( $>93\%$ ) in integrierten Optiken im mid-IR über weite Wellenlängenbereiche erzielt werden können. Diese Charakterisierung wurde in den ersten zwei Veröffentlichungen für zwei verschiedene integrierte optische Plattformen, ein Chalkogenidglas (GLS) in der ersten Veröffentlichung und ein Fluoridglas (ZBLAN) in der zweiten Veröffentlichung durchgeführt, während in der zweiten Veröffentlichung der Vergleich zwischen den beiden Plattformen betont wird. Das ultimative Ziel ist die Kombination von vier oder mehr Teleskopen in einer integrierten Optik. Zu diesem Zweck gehen wir in der dritten Veröffentlichung über klassische zwei-Teleskop Kombiniierer hinaus und untersuchen weitergehende Konzepte wie sogenannte ABCD-Kombiniierer und diskrete vier-Teleskop Kombiniierer. Wir zeigen experimentell, dass diese Koppler geeignet sind, um die Kontraste zwischen monochromatischen Einganglichtfeldern zu rekonstruieren und ebenen mit dieser Proof-of-Concept-Studie den Weg zu einem Vier-Teleskop-Kombiniierer. Auf der Grundlage der experimentellen Ergebnisse wird schließlich die Durchführbarkeit und Performance eines auf integrierte Optik basierten interferometrischen Instruments diskutiert.

# Contents

<b>Contents</b>	<b>vii</b>
<b>1 Scientific motivation</b>	<b>3</b>
1.1 Circumstellar disks and planet formation . . . . .	4
1.2 Direct detection of exoplanets . . . . .	7
1.3 Active galactic nuclei . . . . .	9
<b>2 Astronomical interferometry</b>	<b>11</b>
2.1 Fundamentals of astronomical interferometry . . . . .	12
2.2 Spatial frequency sampling . . . . .	15
2.3 Bulk optics beam combination schemes . . . . .	17
2.4 Current and future landscape of interferometric facilities . . . . .	17
<b>3 Integrated optics and Ultrafast Laser Inscription</b>	<b>21</b>
3.1 Basics of optical waveguides . . . . .	21
3.2 Physics of Ultrafast Laser Inscription . . . . .	23
3.3 On-chip beam combination schemes . . . . .	27
3.4 Requirements of integrated optics chips in astronomy . . . . .	29
3.5 Previous and related works . . . . .	34
3.6 Applications beyond astronomy . . . . .	35
<b>4 Paper 1 (Tepper 2017a): Integrated optics prototype beam combiner for long baseline interferometry in the L and M bands</b>	<b>37</b>
<b>5 Paper 2 (Tepper 2017b): Ultrafast laser inscription in ZBLAN integrated optics chips for mid-IR beam combination in astronomical interferometry</b>	<b>47</b>
<b>6 Paper 3 (Diener 2017): Towards 3D-photonics, multi-telescope beam combiners for mid-infrared astrophysics</b>	<b>61</b>
<b>7 Conclusion &amp; Perspective</b>	<b>75</b>
<b>Bibliography</b>	<b>81</b>
<b>Acknowledgements</b>	<b>87</b>

<b>Declaration</b>	<b>89</b>
<b>Curriculum Vitae</b>	<b>93</b>

## OUTLINE AND OVERVIEW

This thesis is concerned with the characterization of integrated optics chips for the beam combination for high-resolution astronomical interferometry in the mid-IR wavelength range. In the first chapter, I will motivate this work from the astronomer's perspective and demonstrate why high-resolution observations in this wavelength domain are scientifically valuable. To this end, I will present three science cases, circumstellar disks, exoplanet detection and active galactic nuclei, in which this instrumental effort can help advance our current understanding. In the following chapter, I will explain the principle of astronomical interferometry and illustrate the effect of spatial frequency coverage on the image reconstruction. To convey an idea of classical beam combination without integrated optics, I will also depict conventional beam combiners based on bulk optics. Then, I will briefly mention the major interferometric facilities to show how this work fits into the current landscape of astronomical interferometers. In the third chapter, the principle of integrated optics and the manufacturing of integrated optics chips by Ultrafast Laser Inscription (ULI) will be explained. Then, I will demonstrate how ULI can be exploited to inscribe on-chip beam combiners and discuss what the specific requirements are that IO have to fulfill for this purpose. Last, I will recap previous works in the field of mid-IR integrated optics and mention applications of ULI beyond astronomy.

The main body of this work consists in three peer-reviewed papers that were published in the course of my PhD work. In the first paper ([Tepper et al. 2017a](#)), I characterize integrated optics based on a chalcogenide glass (GLS) for the combination of two telescopes manufactured by means of so-called positive writing. The second paper ([Tepper et al. 2017b](#)), provides a comparison to an alternative platform, that is depressed writing in a fluoride glass (ZBLAN). The two papers demonstrate the feasibility of on-chip interferometric beam combination over broad wavelength ranges while maintaining a high interferometric contrast. Additionally, both papers experimentally address the relevant properties of integrated optics for astronomical applications. The third paper ([Diener et al. 2017](#)) deals with more complex on-chip beam combining schemes such as the so-called ABCD combiners and zig-zag arrays for the combination of up to four telescopes.

In the final chapter, I will discuss the feasibility of a four-telescope on-chip beam combiner for the mid-IR. I will describe the routes I value most promising and point out the necessary actions to carry out a science-qualified instrument.



## Scientific motivation

Astronomical interferometry is an observational technique that allows to surpass the resolution limit of single telescopes by more than an order of magnitude. By combining the light from multiple telescopes separated by more than hundreds of meters, today’s largest interferometers can achieve angular resolutions of a few milliarcseconds<sup>1</sup>. For example, at typical distances of 100 parsecs<sup>2</sup> for nearby star forming regions, this angular resolution translates into physical sizes of a few astronomical units(AU)<sup>3</sup>. At such resolutions, exoplanetary systems and star forming regions can be studied at a totally different level of detail compared to resolutions of  $>10$  AU for single telescope at the same distance.

This work is concerned with the development of integrated optics beam combiners for mid-IR interferometry as opposed to classical bulk optics designs which will be discussed in detail in Chap. 3. This would enable delivering images in the astronomical L and M band with unprecedented resolution and dynamic range by means of interferometry. In this chapter, I want to point out why the mid-IR region is a scientifically interesting spectral region for high resolution astronomy. I will demonstrate this in the following on the basis of three selected science cases and refer to previous interferometric observations in the respective fields.

Throughout this thesis I will often refer to the infrared astronomical bands, which are wavelengths bands in which the atmosphere is transparent and that the non-astronomical reader may not be familiar with. Please see Fig. 1.1 for the nomenclature.

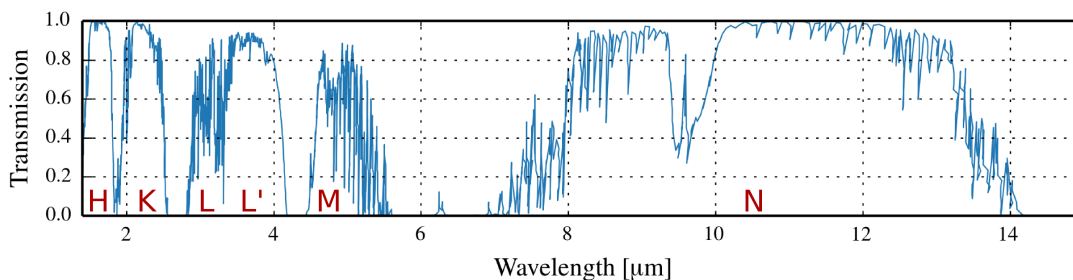


Figure 1.1: The infrared transmission of the earth’s atmosphere measured at Mauna Kea, Hawaii, at 4200 m and the nomenclature of the astronomical bands. The extinction is mostly due to water vapor and CO<sub>2</sub> absorption. The data is digitized from <https://www.hao.ucar.edu/people/phil-judge/collaborators/eclipse2017/eclipse2017.html>.

<sup>1</sup>One arcsecond is 1/3600 degree.

<sup>2</sup>One parsec (pc) is approximately  $3 \cdot 10^{16}$  m. At 1 parsec distance, 1 AU subtends an angle of 1 arcsecond.

<sup>3</sup>One astronomical unit (AU) is the distance between the sun and the earth and is approximately  $1.5 \cdot 10^{11}$  m.

## 1.1 Circumstellar disks and planet formation

Circumstellar (CS) disks are a ring- or donut-shaped accumulation of matter around a star and are interesting regions to study as they are the byproduct and reservoir of star formation as well as the birth place of planets. To date, there is no fully coherent theory of how the initial CS disk transforms into the planetary systems that we observationally find including our own. At first, I will explain the origin and evolution of CS disks as well as briefly mention some models of planet formation in CS disks. In the second part, I will present some exemplary observations and, then, illustrate how this instrumental work can pave the way to advancing our knowledge in these fields.

The birth of a star takes place on timescales of the order of 50 Myrs. Its evolution is depicted in Fig. 1.2 at different evolutionary stages. According to the widely accepted nebular hypothesis, stars are formed in collapsing dense clumps in giant molecular clouds (GMC)<sup>4</sup>. Such cores are initially stable, but as soon as the gravitational potential overcomes the internal gas and magnetic pressure<sup>5</sup>, material starts to fall into its center, where the so-called protostar, the kernel of a new star, is built up (Fig. 1.2c). For roughly 100,000 years, the protostar continues to accumulate mass from the surrounding envelope of gas and dust. Due to a nonzero net angular momentum of the initial cloud material, the whole system has flattened out and increased in angular velocity as it contracted. While slower particles fall into the star, faster particles may be able to occupy orbits at different distances depending on their speed. This results in a disk-like structure surrounding the prenatal star, which is then called circumstellar disk in general or protoplanetary disks at this particular evolutionary stage (Fig. 1.2d). CS disks have lifetimes of the order of 3-5 Myrs (Armitage 2010) and can be roughly classified according to their age as follows: protoplanetary disks in which most of the primordial  $H_2$  gas is present and planetesimals may start to form, transitional disks in which gaps and holes are present due to planets clearing out and/or photoevaporation and, finally, debris disks which only consist of planets/planetesimals and secondary dust produced by the collision of those (Wyatt et al. 2015). At the same time, the prenatal star further contracts under its own gravity until the star's temperature reaches about 10 MK and ignites nuclear fusion. The star has now entered the main sequence<sup>6</sup>.

Here, we focus on the CS disks, in particular their evolution and dust processing mechanisms within, as they reveal how planetary systems form. CS disks were first observed by the Hubble Space Telescope (HST) (McCaughrean & O'dell 1996) and have since been one of the most active areas in astronomical research. Figure 1.3a shows two exemplary images of circumstellar disks with face-on and edge-on views. Due to the difficulty in spatially resolving circumstellar disks, the limited number of observations and the highly complex ongoing physics, there is still no clear picture of the evolution of circumstellar disks.

CS disks are not trivial to model as they consist of gas, dust, planetesimals and asteroids at different temperatures which all interact with each other. Figure 1.3b schematically shows the spatial structure of a circumstellar disk and displays the large range of spatial scales involved. The radiation from the parent star heats up the surrounding disk, resulting in a temperature

<sup>4</sup>GMCs are regions denser than the surrounding interstellar medium in which the formation of molecules, mostly  $H_2$ , is possible. GMCs are not homogeneous but contain clumps and irregular cloud complexes.

<sup>5</sup>This limit is formally calculated by the Jeans Mass which takes into account the density, the temperature and the molecular weight of the particles.

<sup>6</sup>The main sequence is the common evolutionary track for most stars, in which hydrogen burning takes place.

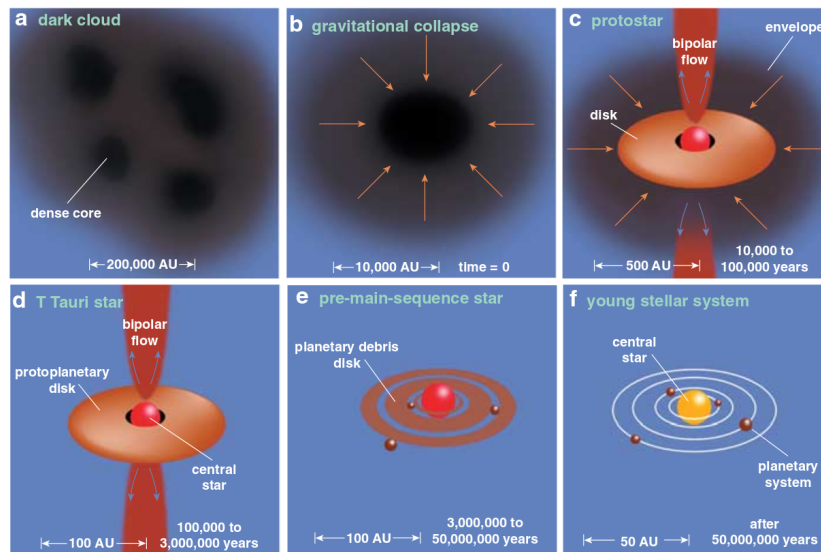


Figure 1.2: The formation of stars, disks and planets from a molecular cloud depicted at different evolutionary stages. Subfigures (a) and (b) depict the collapse of a dense core within a giant molecular cloud. Afterwards, the protostar is formed by further accretion of the surrounding material and bipolar jets emanate as powerful winds from the poles (c). Here, an early CS disk has already formed. Once the dusty envelope is dissipated (d), the object becomes visible in the optical and is then called a T Tauri star. In the pre-main-sequence (e), the star has acquired nearly all of its mass but has not yet started hydrogen fusion. In the disk, planetesimals may start to form while still being surrounded by dust. Finally, most of the dust is dissipated or has been accreted by the planets (e). Reprinted from [Greene \(2001\)](#).

gradient, with about 1500 K at the inner rim, across the disk. In particular, the process of planet formation within the CS disk and its conditions is not well understood. In the core-accretion model ([Pollack et al. 1996](#)), planets are believed to form from submicrometre-sized particles of dust and ice which collide and stick together due to electrostatic and gravitational forces as they become larger ([Dominik & Tielens 1997](#)). However, as soon as silicate grains grow beyond mm size (dcm size for icy grains), they start to bounce off each other and migrate quickly towards the center. Several solutions to this problem have been presented. [Kataoka et al. \(2013\)](#) argued that, beyond the snowline<sup>7</sup>, icy particles form fluffy aggregates which circumvent the bouncing barrier. However, this does not explain planet formation within the snowline. Another model could show that small particles can clump due to turbulences in the disk and then grow further due to their self-gravity ([Johansen et al. 2007](#)). Yet, the existence of initial turbulences in the disk is not established and the small particles must have already surpassed the bouncing barrier. Further models argue that particles may create turbulence themselves ([Weidenschilling 1995](#)) or clumps are built up by streaming instabilities ([Youdin & Goodman 2005](#)).

As the initial clumps and planetesimals are too small and too faint to be directly detected, it is necessary to address the mineralogy of the dust particles, i.e. composition, crystallinity and grain size distribution to advance our understanding on this matter. Whereas dust grains in the interstellar medium are mostly amorphous (<2% crystalline) and smaller than 0.1  $\mu\text{m}$

<sup>7</sup>The snowline is the distance from the parent star at which water condenses into icy grains.

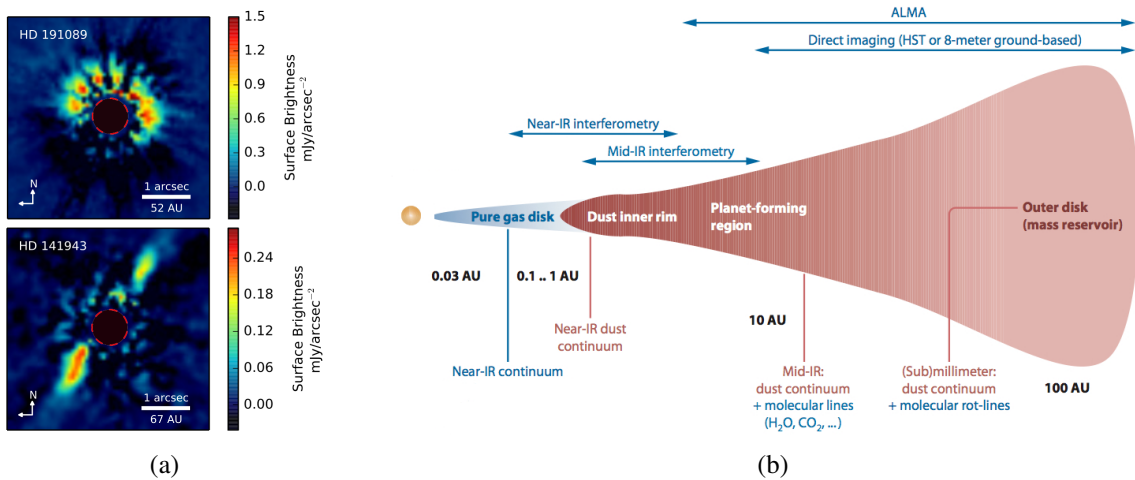


Figure 1.3: (a): Observations of circumstellar disks taken with the Hubble space telescope at  $1.1 \mu\text{m}$  using a coronagraph, an observational technique that blocks the bright stellar flux. The two images do not provide very high resolution but give an idea about how they appear as face-on (upper image) and edge-on (bottom image) depending on their orientation. Image reprinted from [Soummer et al. \(2014\)](#). (b): The sketch shows the spatial structure of a circumstellar disk. Above, the adequate observing techniques are depicted in order to resolve different regions. ALMA is an interferometer operating at radio wavelengths. The instrumentation presented in this thesis falls into the category of mid-IR interferometry. Image reprinted from [Dullemond & Monnier \(2010\)](#).

([Meeus 2011](#)), CS disks contain large amounts of crystalline dust (up to 95% and 40% in the inner and outer disk, respectively [van Boekel et al. 2004](#)) and inhabit planetesimals/planets. This transition is not well understood and it is not clear on which temporal and spatial scales it takes place. Yet, they are linked to fundamental questions in the planet formation process. For instance, the initial crystallization process requires high ( $>1000 \text{ K}$ ) temperatures but crystalline features have been detected in the outer, colder parts of the disks, which hints at radial mixing of the dust particles. Also, crystalline features have been detected in comets and are, therefore, believed to be among the building blocks of terrestrial planet formation. Thus, they can serve as tracers for potential planet forming regions in the disk.

We can see from this (not exhaustive) excursion into planet formation theory that improved observations of the planet forming regions are necessary in order to constrain or discriminate models. Typical distances for close circumstellar disks are 100 parsecs, so that observations with a single telescope can only assess the large scale ( $>10 \text{ AU}$ ) structure of the disks. However, the purely photometric and spectroscopic analysis, has been able to deliver information about the smaller spatial structures. CS disks show a radial temperature gradient which can be translated into peaks in the spectral emission through Wien's displacement law. As an example, the spectra of Herbig Ae/Be stars<sup>8</sup> show a peak in the near-infrared spectrum corresponding to  $1500 \text{ K}$ , which was then theoretically modeled by an inner hole in the disk of about  $0.1 \text{ AU}$  caused by the sublimation of dust at this temperature ([Hillenbrand et al. 1992](#)). Still, there is no definite way of telling solely from spectroscopic data whether this is true since also other models are able to reproduce the measured spectra.

<sup>8</sup>Herbig Ae/Be stars are pre main sequence stars but higher in mass than T Tauri stars.

Due to this degeneracy, directly resolving the spatial structures of the disk through astrometry is an inevitable technique in order to advance our picture of circumstellar disks. In particular, the potential formation of earth-like planets within the inner few AU makes such observation even more compelling. The interferometric instruments MIDI<sup>9</sup> (Leinert et al. 2003), AMBER<sup>10</sup> (Petrov et al. 2007) and PIONIER<sup>11</sup> (Le Bouquin et al. 2011) have demonstrated the high-resolution capabilities of the Very Large Telescope Interferometer (VLTI) in this field over the past 15 years.

Using the MIDI instrument, van Boekel et al. (2004) could measure the spectra around 10  $\mu\text{m}$  wavelength of the inner 1-2 AU of disks around Herbig Ae stars where Earth-like planets may form. This allowed for the first time to detect a gradient in the chemical composition of the dust in proto-planetary disks. More specifically, the fraction of crystalline material and large grains could be compared for the inner and outer regions. Their findings put further constraints on the planet formation theory and could determine that the crystallization process takes place in the inner region of the early (1 Myr) CS disk and is then distributed into the outer regions by radial mixing and/or shock processing.

As the evolution of planetary systems takes place on very long timescales, it is evidently necessary to observe a variety of systems in different evolutionary stages to obtain a complete picture on the process. One particularly interesting stage is the previously mentioned transitional disk in which larger bodies start to form and leave as a result a cleared out gap in the disk. Matter et al. (2016) used interferometric VLTI data combined with HERSCHEL/PACS<sup>12</sup> data to resolve the inner 0.1 to 10 AU to detect such a dust gap in the transitional disk of the Herbig star HD 139614 extending from 2.5 to 6 AU. Such work evidently puts constraints on the modeling of dust interaction in disks and demonstrates how earth-like planets may form.

The mid-IR beam combiner instrument proposed in this thesis will work in the L and M bands and will be able to combine four or more telescopes. This will close the spectral gap between AMBER and MIDI and increase the number of available telescopes (see Sec. 2.4 for an overview of current and planned instruments). Consequently, this will enable to access the critical spectral range for planet formation studies (see Fig. 1.3b) and provide a higher image reconstruction fidelity. This will permit to more accurately image the inner 10 AU and directly observe the conditions and tracers of planet formation.

## 1.2 Direct detection of exoplanets

Another, closely related, field of interest is the detection of exoplanets. Once the planetesimals have accreted more matter, they can be detected through various observational techniques. In this section, I will first briefly mention the established methods of exoplanet detection and then point out the exoplanet detection capabilities of interferometry in general and nulling interferometry in particular.

The first detection of an exoplanet orbiting a sun-like star was made by Mayor & Queloz (1995). The hot Jupiter<sup>13</sup>, called 51 Pegasi b, orbits its host star 51 Pegasi within 4.2 years and

<sup>9</sup>MIDI was a two-telescope combiner working in the N band that was decommissioned in 2015.

<sup>10</sup>AMBER is an operational three-telescope combiner for the H and K band.

<sup>11</sup>PIONIER is an operational four-telescope combiner for the H band.

<sup>12</sup>PACS is a photometer and spectrometer for the FIR installed at the HERSCHEL space observatory.

<sup>13</sup>Hot Jupiters are giant gas planets that are similar to Jupiter in their mass but orbit closer to their star and are, therefore, hotter.

is located 51 lightyears away from earth. Since then, 3664 planets (as of the 6th of September 2017) have been detected<sup>14</sup>, mostly by the space mission KEPLER (NASA). The vast majority (>97%) of exoplanets has been detected by indirect measurements such as transits or radial velocity (RV) measurements (Ollivier & Maurel 2014). The transit method relies on a dip in the stellar flux due to the transit of the planet in the line of sight. Statistically, this will rather probe planets that are close to the planet as they orbit faster and lie more often in the line of sight of the star as well as large planets. RV, on the other hand, infers the companion due to the Doppler shift in the stellar spectral lines caused by the Keplerian motion of the orbiting planet. This method can only detect massive planets that orbit close to rather low-mass parent stars, e.g. the earth in our solar system would be too low in mass at its distance given the Sun's mass. Also RV is restricted to cold stars, i.e. old stars, as the spectral lines of hot stars are too much broadened. In 2004, the first exoplanet, 2M1207b, with an orbit of 40 AU was imaged directly (Chauvin et al. 2004). Due to the limited angular resolution of single telescopes, as previously discussed, this method is obviously limited to exoplanets that are well separated (>10 AU) and therefore can hardly detect planets in the habitable zone<sup>15</sup>.

Exoplanet detection by interferometry could nicely complement these observing techniques and provide star/planet flux ratios as well as observe planets that do not transit in the line of the sight as needed transit detection. Due to its superior angular resolution, interferometry could in principle be used to directly detect earth-like planets in the habitable zone. Through spectral measurement of the light coming from the planet, its atmospheric chemical composition may be analyzed, which can be related to the planet's formation and potential extraterrestrial life.

Yet, there have been few (likely) successful attempts of directly detecting exoplanets using interferometry. Using non-redundant aperture masking<sup>16</sup>, Kraus & Ireland (2012) could demonstrate direct interferometric observations that were inconsistent with a single point source for the young star LkCa15 (distance 145 pc) and provided hints towards a protoplanet or several protoplanets in the middle of a disk gap at a separation of 16 AU. Yet, the obtained interferometric data over different wavelengths, namely L' and K band, were not fully consistent so that further observations will be necessary to unambiguously determine its true nature. Huélamo et al. (2011) also used aperture masking interferometry to study the T Cha system in the K<sub>S</sub> (2-2.35 μm) and L' band and detected a faint companion that may be a recently formed planet within the disk. Zhao et al. (2011) carried out an analysis on the precision requirements for hot Jupiter exoplanet detection by interferometry and could show that star/planet flux ratios up to  $2.1 \cdot 10^3$  could be detected using the CHARA array<sup>17</sup>.

However, long-baseline interferometry, that is the combination of multiple individual telescopes, could so far not directly detect any exoplanets. This is in part hampered by the fact that there is no long-baseline interferometric instrument at the VLTI working in the L and M bands at the moment. These spectral bands are favorable for exoplanet detection as the contrast between the bright stellar flux and the faint exoplanet flux decreases with longer

---

<sup>14</sup>a complete list of detected exoplanets is given in the Extrasolar Planets Encyclopedia under <http://exoplanet.eu/catalog/>.

<sup>15</sup>The habitable zone is the area around a star in which water can exist in its liquid form and, therefore, potentially hosts life. For a sun-like star this corresponds to a distance of about 0.9 - 1.7 AU (Kopparapu et al. 2013).

<sup>16</sup>Aperture masking is the masking of a *single* telescope with a few holes inside the aperture to operate it in interferometric mode, which allows to reach about twice its diffraction limit.

<sup>17</sup>CHARA is a six-telescope interferometer at Mount Wilson, California.

wavelengths. At even longer wavelengths around  $10\ \mu\text{m}$  (N band), the contrast becomes even more favorable but the thermal background of the sky increases and complicates observations. The existence of a mid-IR interferometric beam combiner would greatly improve the VLTI's exoplanet detection capabilities and complement the existing facilities.

Still, all direct methods suffer from the fact that the parent star is easily  $10^6$  times brighter than the emission from the planet. This is even more detrimental to interferometry than to single-dish observations, as the light is separated into several beams, integration times are shorter and the overall more complicated optical setup, which together further reduces the throughput. An interferometric solution to this problem is called nulling, where the light coming from the star is brought to destructively interfere and cancel out while the regions to be observed remain visible. The instrumental demands of nulling are extremely challenging as the rejection ratio needs to be on the order of  $10^{-6}$ , or in other words the instrumental contrast needs to be above 99.9999%. The largest ground-based nulling program was conducted at the KECK interferometer<sup>18</sup>, which was however not devoted to exoplanet observation but to the exozodiacal discs of main-sequence stars (Mennesson et al. 2014). Already the atmospheric turbulences make such an undertaking extremely challenging for ground based telescopes. Two large space missions equipped with a nuller called *Terrestrial Planet Finder* (NASA) and *DARWIN* (ESA) were considered but eventually canceled.

Currently, there are no activities towards a new space-based interferometer. However, replacing classical bulk optics beam combination setups, by miniaturized on-chip beam combination using integrated optics holds great potential for a such a project. The integrated optics chips developed in this thesis are not intended for nulling interferometry as this requires different and more stringent requirements which are beyond the short-term capabilities of this project. Nevertheless, it should be mentioned that mid-IR integrated optics beam combiners would be perfectly suitable for a future space mission. This is because, compared to bulk optics solutions, integrated optics need no further maintenance and alignment and have stable mechanical and thermal properties. Also, integrated optics have a small footprint and little weight which makes them an ideal candidate for space missions.

### 1.3 Active galactic nuclei

Mid-IR long-baseline interferometry can also be applied to extragalactic astronomy. Active galactic nuclei (AGN) are at the center of galaxies, which radiate strongly from gamma rays to radio wavelengths as a result of accretion of matter by a central supermassive black hole. This central engine is believed to be surrounded by a doughnut-shaped torus of gas and dust, which typically extends over 0.1 to 10 pc (Burtscher & Tristram 2013). Since the nearest AGNs are located a few Megaparsecs away, single-dish telescopes fail to resolve the dusty tori. AGNs are believed to be powered by the material accretion from the torus onto the supermassive black holes. Interestingly though, observations have so far revealed a large variety in the emission spectra of AGNs leading to the classification of Seyfert I, Seyfert II, Quasars and a few other types of galaxies (Antonucci 1993). Seyfert I type galaxies show both narrow and broadened spectral lines. The broad lines are believed to originate from fast moving (10,000 km/s) regions close to the accretion disk whereas the narrow features originate from slower (400 km/s) more outer regions extending to 100 parsecs. Seyfert II

---

<sup>18</sup>KECK interferometer is a two-telescope interferometer with 85 m separation located at Mauna Kea, Hawaii.

galaxies, on the other hand only exhibit narrow line regions. The physical explanation for this variety is based on different viewing angles, in the sense that the dusty torus obscures the inner broad-line region when the system is observed edge-on. However, since AGNs' torus cannot be resolved by single-dish observations, there has been much debate about the effect of line-of-sight orientation.

Interferometric observations, on the other hand, allow to resolve the inner parsecs. To this end, over the last ten years, several studies using the MIDI instrument were carried out, successfully resolving the inner parsecs of the dusty tori, which are summarized by [Burtscher & Tristram \(2013\)](#). This meta analysis found that the discrepancy of type I and II Seyferts cannot be fully attributed to the AGN orientation suggesting that actual different physical phenomena are at play.

In 2014, [Hönig et al. \(2014\)](#) could determine the distance of the supermassive black hole in the AGN of the galaxy NGC 4151. This estimate is based on the combination of interferometric data and a time lag between different emission lines. The interferometric data was provided by the KECK interferometer in the K-band and could determine the angular size of the dusty torus around the black hole while the time lag between the UV-optical emissions (from the close accretion disk) to the infrared emission (from the torus) can be used to determine its physical size. When the inner accretion disk emits in the UV-optical, it also heats up the surrounding dusty torus, which then re-emits in the infrared and creates a time-lag (10-100 days) between the two spectra from which the physical size can be calculated. Together with the angular size of the object, the distance was estimated to  $19.0^{+2.4}_{-2.6}$  Megaparsecs. Measuring this distance within reasonable error bars is critical to determine the mass of such black holes through reverberation mapping<sup>19</sup> for which the physical size of the torus is relevant.

A mid-IR four-telescope beam combiner would nicely complement the above mentioned MIDI observation data as it would add data in the L and M bands as well as provide more information on the spatial structure due to the double number of available telescopes, which is critical to understand the role of orientation. This would help to shed light on the origin of type I and type II AGNs. Additionally, it would allow to study the dust and gas morphology in order to better understand the physics of AGNs, for instance how the gas reservoir feeds the accretion disks around the black holes.

---

<sup>19</sup>Reverberation mapping is a primary technique for inferring the black hole's mass through surrounding gas motion and the shape of the AGN.

## Astronomical interferometry

Astronomical interferometry is a complex observing technique that allows to surpass the resolution capabilities of single telescopes by the coherent combination of multiple telescopes. As an example, Fig. 2.1 shows the Very Large Telescope Interferometer (VLTI) in Chile. In the first section, I will briefly present the principle of astronomical interferometry and the essential equations. In the following sections, I will illustrate the effect of a dense spatial frequency sampling on the reconstructed image and show types of interferometric beam combination based on bulk optics as they represent the classical alternative to on-chip beam combination as I propose in this thesis. Finally, I will briefly present the landscape of the current major interferometric facilities.



Figure 2.1: The Very Large Telescope Interferometer situated on Cerro Paranal in Chile at 2635 m elevation. The four large telescopes can be combined to operate as an interferometer. Their collected light is guided below ground (inserted black lines) to the beam combination lab. Here, the beams are superimposed and the interferometric pattern (inserted red fringes) between each pair of telescopes is detected. Picture taken by M. Struik (CERN)/ESO.

## 2.1 Fundamentals of astronomical interferometry

The theoretical basis for astrophysics is provided by the van Cittert-Zernike theorem (VCZ), which relates the spatial coherence of a source in the far-field to the Fourier transform of its angular brightness distribution. Before going straight to the VCZ, some preliminary concepts need to be developed. This section is based on [Glindemann \(2011\)](#), which I recommend for a more detailed description and further reading. A more intuitive approach is found in [Buscher \(2015\)](#) and [Millour \(2008\)](#).

In the following, the light field is represented by  $v(\vec{x}_i, t)$ , which denotes the optical disturbance at a certain position  $\vec{x}_i$  and time  $t$ . The optical disturbance is proportional to the electrical and magnetic field carried by the light wave and can therefore be interpreted as such. The correlation between the optical disturbances of the light field at positions  $\vec{x}_1$  and  $\vec{x}_2$  at times  $t$  and  $t + \tau$  is given by the mutual coherence function (MCF) as

$$\Gamma(\vec{x}_1, \vec{x}_2, \tau) := \lim_{T \rightarrow \infty} \int_{-T}^T v(\vec{x}_1, t + \tau) v^*(\vec{x}_2, t) dt, \quad (2.1)$$

in which  $*$  denotes complex conjugation. Since the oscillations of the electrical fields in the visible and infrared are too fast for any detector to be directly measured, we integrate over a measurement period  $2T$ . The intensities at each individual point  $\vec{x}_i$  can be expressed through the MCF by

$$I(\vec{x}_i) = I_i = \Gamma(\vec{x}_i, \vec{x}_i, 0). \quad (2.2)$$

Applied to astronomical interferometry, the points  $\vec{x}_1$  and  $\vec{x}_2$  refer to the locations of the telescopes and measure the MCF of the light field originated from the observed object as shown in Fig. 2.2. The telescope positions  $\vec{x}_1$  and  $\vec{x}_2$  define the so-called baseline vector  $\vec{B} = \vec{x}_1 - \vec{x}_2$ . The vector  $\vec{\alpha}'$  points at the individual contributions of the source with respect to the line of sight  $\vec{\alpha}$ . The light from the two telescopes is then combined to produce an interferometric signal from which the MCF can be determined. The essential statement of the VCZ is that the angular brightness distributions  $I_b(\vec{\alpha}')$  ('image') of the source can be related to the MCF/interferometric signal.

In the following, we will not consider the VCZ in its most general form but a special case which is the most convenient for the conditions of astrophysics observing a distant incoherent source. Therefore, the following assumptions are made:

- The angles between the vector pointing to the point of observation with the line of sight must be small (Fresnel approximation).
- The source must be incoherent.
- The observed spectral bandwidth  $\Delta\nu$  is much smaller than the average frequency  $\nu_0$  (Quasi-monochromatic approximation).
- The optical path difference (OPD) from the object to the recombination point between telescope 1 and 2 is much smaller than the coherence length  $l_c$ <sup>1</sup>

---

<sup>1</sup>The coherence length is the OPD after which the interferometric contrast has decreased to  $1/e$ .

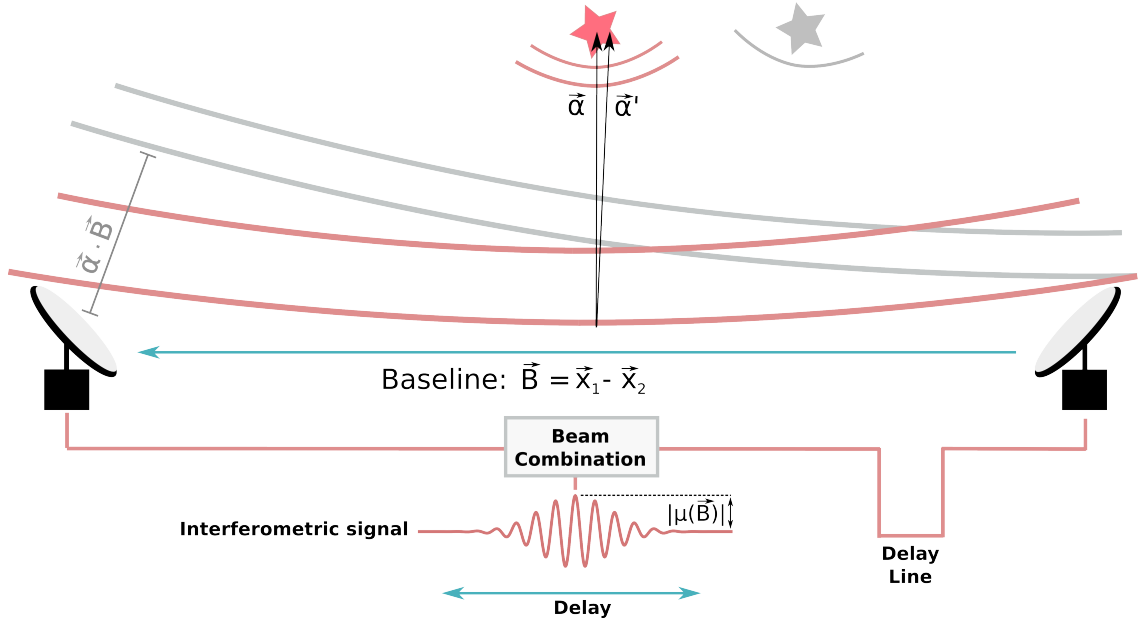


Figure 2.2: This sketch depicts the principle of stellar interferometry. A distant, incoherent source, here symbolized by the star, is observed at  $\vec{\alpha}$ , which is the vector of line of sight. With respect to the line of sight,  $\vec{\alpha}'$  directs at different points of the observed source. The telescopes form the baseline vector  $\vec{B} = \vec{x}_1 - \vec{x}_2$ . Before the light collected by the individual telescopes is combined, the optical paths must be equalized by a delay line. From the resulting interferogram, here depicted after photometric correction (Eq. 2.5), the absolute visibility  $|\mu(\vec{B})|$  can be extracted. In gray, the situation is depicted when the line of sight is not perpendicular to the baseline vector. As a result, an optical path difference  $\vec{\alpha} \cdot \vec{B}$  ('piston') is introduced and the effective baseline is  $|\vec{B}_{eff}| = |\vec{B}| \sin(\alpha)$  with  $\alpha$  being the angle between  $\vec{B}$  and the line of sight. The beam combination part is not further illustrated here but discussed in Sec. 2.3.

The VCZ then states that

$$\mu(\vec{B}) := \frac{\Gamma(\vec{B}, 0)}{\sqrt{I_1 I_2}} = \frac{\int I_b(\vec{\alpha}') e^{-ik(\vec{B} \cdot \vec{\alpha}')} d\vec{\alpha}'}{\int I_b(\vec{\alpha}') d\vec{\alpha}'} \quad (2.3)$$

The complex term  $\mu(\vec{B})$  is called the visibility function and is the normalized MCF at  $\tau = 0$  (in other words, at zero OPD) and is related to the angular brightness distribution  $I_b(\vec{\alpha}')$  by a Fourier transform. Note that the positions  $\vec{x}_1$  and  $\vec{x}_2$  have been replaced by their distance to each other,  $\vec{B}$ , as their absolute positions are irrelevant. The entity  $k$  is the wavevector. The absolute visibility  $|\mu(\vec{B})|$  is between 0 and 1, while being equal to 1 for a point-source.

Intuitively speaking, the observed object can be thought of as many point sources at  $\vec{\alpha}'$  each producing their own interferogram. However, due to their different positions  $\vec{\alpha}'$ , their interferograms are shifted with respect to each other reducing the overall visibility in a way which allows to retrieve spatial information of the source from the visibilities. In the particular case of a binary system, the two interferograms are exactly  $\pi$  phase shifted, so that they destructively interfere, i.e.  $\mu(\vec{B}) = 0$ , if the angular separation of the two stars is  $\lambda/(2|\vec{B}|)$ . This is where the resolution limit for interferometry stems from since two point sources can clearly be separated at this differential angle. In the example of a binary we see

that the measurement of the visibility between two telescopes (one baseline) can be sufficient to determine its projected separation. However, this implies the a priori assumption that the object is a binary with a given flux ratio and projection but unknown separation. In general, for more complex structures and in order to minimize the necessary a priori assumptions as well as to be able to unambiguously reconstruct  $I_b(\vec{\alpha}')$  for more complex objects, the visibility  $\mu(\vec{B})$  needs to be sampled at as many baselines  $\vec{B}$  as possible, i.e. increasing the number of telescopes as discussed in Sec. 2.2. By comparing the resolution limit,  $\lambda/(2|\vec{B}|)$ , of today's largest interferometers ( $|\vec{B}| > 200$  m) to the resolution of a single telescope<sup>2</sup>,  $1.22\lambda/D$ , with  $D$  being its diameter, we can see that interferometry surpasses the resolution of today's largest optical telescopes ( $D \approx 10$  m) easily by an order of magnitude. Interferometry can achieve larger resolutions without having to build larger telescopes but by increasing their separation.

The visibility  $\mu(\vec{B})$  can be extracted from the intensity  $I$  of the combined light from telescopes 1 and 2 as follows

$$I = I_1 + I_2 + 2\sqrt{I_1 I_2} \cdot |\mu(\vec{B})| \cos(\Phi(\vec{B}) - k\vec{\alpha} \cdot \vec{B}). \quad (2.4)$$

Here, the visibility function is split in its absolute value and phase  $\Phi(\vec{B})$ . The absolute value determines the amplitude of the interferometric part of the signal and the phase its position.

So far, we have assumed that  $\vec{B}$  is perpendicular to the line of sight. However, this is generally not the case and in particular this changes with time due to the rotation of the earth, as shown by the gray part in Fig. 2.2. Therefore, an additional phase is introduced called piston  $k\vec{\alpha} \cdot \vec{B}$ ,  $k$  being the wavevector. Since, by assumption, we operate in a small but finite bandwidth, it is crucial to measure the interferogram within the coherence length. Therefore, this piston needs to be corrected by delay lines that can span up to 100 m. Likewise, the baseline  $\vec{B}$  needs to be replaced by an effective baseline that is perpendicular to the line of sight.

The  $\Phi(\vec{B})$  term, on the other hand, is intrinsic to the source. Therefore,  $|\mu(\vec{B})|$  and  $\Phi(\vec{B})$  are the terms that the interferometrist is chasing in order to perform the Fourier transform in Eq. 2.3 to obtain  $I_b(\vec{\alpha}')$ . Measuring the absolute phase  $\Phi(\vec{B})$  is practically impossible. Although delay lines can compensate for the piston, it is impossible to disentangle the piston, which itself is influenced by atmospheric turbulences, from the intrinsic object phase  $\Phi(\vec{B})$ . However, by spectrally dispersing the signal, a gradient phase between the spectral channels can be measured. It should be noted that for more than two telescopes the so-called closure phase can be calculated, which is an observable that can be constructed in such a way that atmospheric turbulences cancel out. More information on this can be found in [Glindemann \(2011\)](#).

The maximum value<sup>3</sup> of Eq. (2.4) is given by  $I_{max} = I_1 + I_2 + 2\sqrt{I_1 I_2} \cdot |\mu(\vec{B})|$ . Therefore, recording  $I$  and the photometric signals  $I_1$  and  $I_2$ , the absolute value can be calculated by applying the so-called photometric correction

$$|\mu(\vec{B})| = \frac{I_{max} - I_1 - I_2}{2\sqrt{I_1 I_2}}. \quad (2.5)$$

If the photometric signals are not available, the raw visibility can be estimated from Eq. 2.4 by  $|\mu(\vec{B})_{raw}| = \frac{I_{max} - I_{min}}{I_{max} + I_{min}}$ . If  $I_1 = I_2$ , the raw visibility equals the photometrically corrected visibility.

<sup>2</sup>Here, according to the Rayleigh criterion, i.e. the first minimum of the PSF of a circular aperture.

<sup>3</sup>To emphasize again: Eq. 2.4 is a periodic function but stems from the quasi-monochromatic approximation. Actually, due to the finite bandwidths, the interferometric cosine term decreases in Eq. (2.4) so that a maximum around zero OPD ( $\tau = 0$ ) exists.

Otherwise, the raw visibility measures a lower value as it does not take into account the fringe decrease due to unbalanced photometries.

In reality, the measured visibility  $|\mu(\vec{B})|$  may be lowered due the so-called instrumental contrast  $C$ . That is because the instrument may reduce the contrast due to differential birefringence or dispersion (see Sec. 3.4) or atmospheric turbulences et cetera. Therefore, the interferometric term in Eq. 2.4 needs to be multiplied with  $C$ . In the publications where the goal is to determine the instrumental contrast  $C$ , our setup is such that the visibility is equal to 1. In that case, if  $|\mu| = 1$ , Eq. (2.5) measures the instrumental contrast  $C$ .

## 2.2 Spatial frequency sampling

In Eq. 2.3, the visibility function is related to the Fourier transform of the brightness distribution of the object. In other words, measurements of the visibility at baseline  $B$ , give access to the spatial frequency component  $B/\lambda$  per radiant of the object, commonly expressed as cycles per arcsecond. It is apparent that due to the limited number of telescopes the visibility function is irregularly and sparsely sampled at only a few baselines depending on the number and position of the telescopes. However, if the object is assumed to be ‘gray’, i.e. has a wavelength independent shape, different spectral channels can access further spatial frequencies as the wavevector appears as a variable in the Fourier transform. Additionally, due to the rotation of the earth, the projected baselines naturally change with time (‘supersynthesis’). As a result, the baseline sampling in the so-called u-v plane, that is the plane perpendicular to the line of sight, becomes more dense. Also, the VLTI features another set of four, smaller, telescopes (called auxiliary telescopes) which are movable in order to provide variable baselines. Still, due to its complexity and the necessary but carefully chosen a priori assumptions about the object, the process of image reconstruction from a limited set of visibility values has stimulated a field of its own (see [Éric Thiébaud & Young \(2017\)](#) for a recent review) with contributions from compressed sensing theory.

Figure 2.3 shows two state-of-the-art reconstructed images obtained by radio and optical/infrared interferometry along with their u-v coverage. Figure 2.3a shows the baseline coverage of ALMA, a radio interferometer<sup>4</sup>, using 44 antennas with separations between 150 and 16 km. Due to the high number of antennas and the earth’s rotation, the u-v plane is filled. As a consequence, the reconstructed image shown below exhibits remarkable detail such as gaps in the surrounding disk of the young star HL Tau. Figure 2.3b shows the u-v coverage of an observation using the four-telescope beam combiner PIONIER in the infrared. The axis are translated into spatial frequencies which demonstrates that, as described above, different spectral channels access different spatial frequencies. The reconstructed image below shows the dust sublimation front around the binary system IRAS 08544-4431.

---

<sup>4</sup>It is critical to note that radio interferometry is based on the same principle as optical/infrared interferometry but directly measures the electrical field of the incoming wavefront at each telescope which is possible due to the lower frequency in radio. This enables to position more antennas more spatially separated and correlate the signals afterwards in post-processing so that no beam combination setups are needed, whereas real-time correlation is required for optical/infrared interferometry.

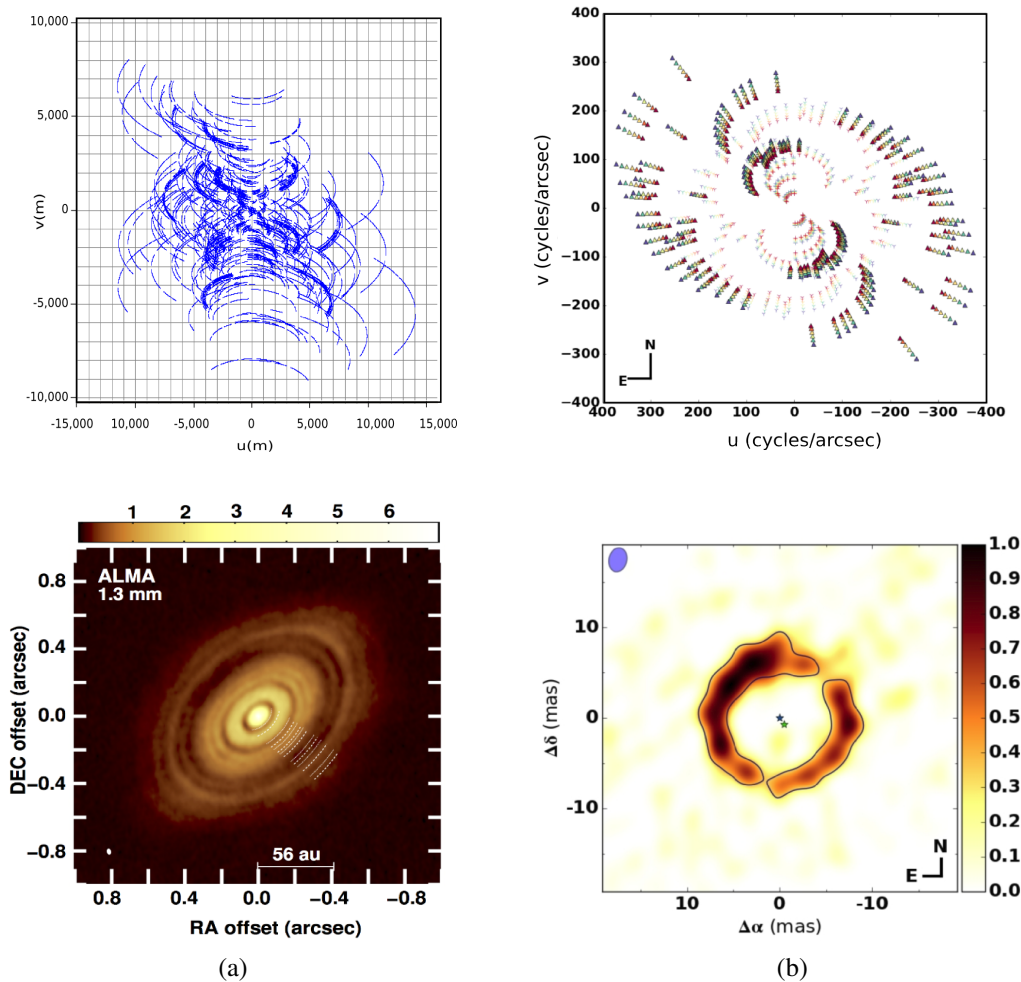


Figure 2.3: (a): Top, the baseline coverage in the  $u$ - $v$  plane of a radio interferometry observation by ALMA using 42 antennas showing the effect of the changing projected baselines due to the rotation of the earth. Below, the reconstructed image of the young star HL Tau.  $u$ - $v$  coverage data from <https://almascience.nrao.edu/alma-data/science-verification> and image credit [ALMA Partnership et al. \(2015\)](#); [Carrasco-González et al. \(2016\)](#). (b): Top, the  $u$ - $v$  coverage of an observation using the four-telescope combiner PIONIER at the VLTI. Here, the baselines are translated into spatial frequency components in cycles/arcsec. The different colors depict different wavelength channels from  $1.53 \mu\text{m}$  to  $1.77 \mu\text{m}$  and the shapes (tripod, triangle, plus) depict different observing times leading to different projected baselines. Below, the reconstructed image of the dust sublimation front around a binary system.  $u$ - $v$  coverage and image credit [Hillen et al. \(2016\)](#).

## 2.3 Bulk optics beam combination schemes

This thesis is concerned with the combination of beams arising from the different telescopes as shown in Fig. 2.2. Whereas this is relatively straightforward to achieve for two telescopes, it becomes more difficult when four or more telescopes need to be pairwise, simultaneously combined. In general, one distinguishes between the Fizeau configuration in which the individual telescopes can be treated as a larger masked telescope (‘homothetical mapping’) and the more widely used Michelson configuration which comprises all others, which will be briefly discussed below. More information on the other types of combination schemes can be found in [Minardi et al. \(2016\)](#); [Glindemann \(2011\)](#); [Mariotti \(1992\)](#).

Figure 2.4 shows two Michelson configurations, the multi-axial (a) and co-axial (b) combination. In the first type of configuration, the beams from the individual telescopes are focused onto the same point but with different tilt angles. Since the different angles correspond to different OPD, the interferometric signal can be read out spatially on the detector as shown in Fig. 2.4a. On the other hand, the co-axial scheme superposes the beams in such a way that the beams seem to propagate from the same direction. Since the angle between the two beams is zero, the fringe pattern is then scanned by applying an external delay line in one of the channels.

A further distinction needs to be made between all-in-one and pairwise beam combiners. Whereas in Fig. 2.4b the different baselines from the three telescopes, i.e.  $A+B$ ,  $A+C$  and  $B+C$ , are read out individually, all beams can also be superposed all together. Then the visibilities need to be disentangled in the Fourier space. This can be achieved by scanning the OPD in a unique way for each baselines so that the signals are separated in the Fourier space. The peaks in the Fourier space can then be related to the visibilities between the telescope pairs.

The two examples in Fig. 2.4 should simply convey an idea of the beam combination process without the use of integrated optics (IO) as it is discussed in Chap. 3. All beam combination schemes in single-mode IO can be classified as co-axial as single-mode waveguides only allow one propagation mode, i.e. differential angles are zero. Therefore, the input beams can be considered as parallel and perfectly superposed. It is clear from Fig. 2.4b that the extension of bulk optics beam combiners to the combination of more telescopes is not straightforward but requires complex and large optical setups. The advantages and disadvantages of IO compared to bulk optics solutions are discussed in sec. 3.4.

## 2.4 Current and future landscape of interferometric facilities

In this section, I want to briefly lay out how this work fits into the landscape of current interferometers. It should be noted that nearly all interferometric sites accommodate multiple back-end interferometric instruments. While the reflective telescopes themselves are achromatic by nature, different instruments need to be developed for different wavelength bands and science requirements.

One of the major, if not the major, institution in astronomical interferometry is the VLTI situated on Cerro Paranal in Chile sitting at 2635 m operated by the European Southern Observatory (ESO). Currently, AMBER (N band), PIONIER (H & K band) and GRAVITY

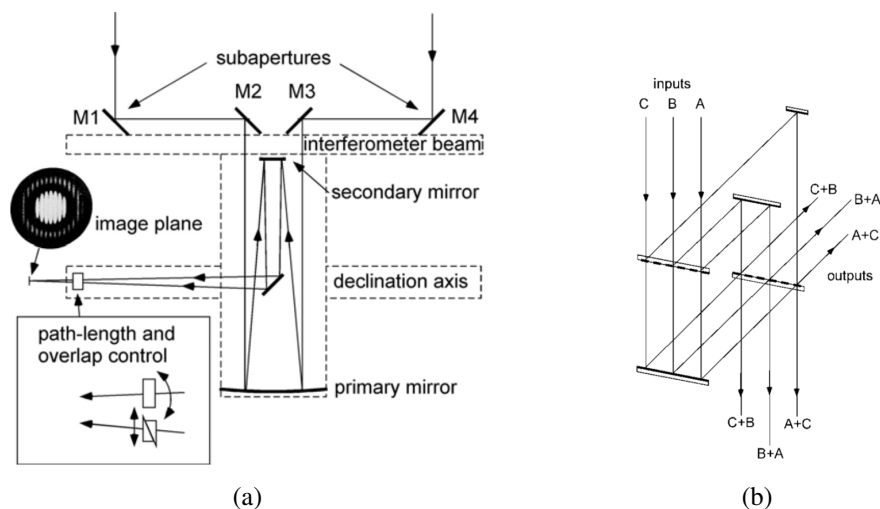


Figure 2.4: The sketches show two examples of beam combinations using bulk optics. (a): Multi-axial beam combination. The beams from the two telescopes are superposed with a nonzero angle and the interferometric pattern is spatially encoded. In the sketch it is assumed that the OPD due to the piston is already compensated for. (b): Co-axial pairwise beam combination for three telescopes using bulk optics. The beams are superposed using beamsplitters and run parallel. The individual point spread functions are imaged on top of each other and the interferometric pattern is temporally encoded by scanning the OPD by a delay line. Images taken from [Labeyrie et al. \(2006\)](#).

(K band) are operational instruments with MATISSE being the next instrument waiting to be commissioned. MATISSE is the only instrument that will cover the astronomical L and M bands. Although, IO have already been established as a reliable technology in the PIONIER and GRAVITY instruments, MATISSE relies on bulk optics combiners since mid-IR IO technologies were not mature enough at the time of its optical design.

On the US-funded side, CHARA (V, R, I, J, H & K band), KECK (H, K, L & N band) and the LBTI (L, M & N band) should be mentioned. CHARA is an array of six telescopes with the largest baselines of 330 m (i.e. highest angular resolution) but rather small 1 m telescopes, which limits its operation to rather bright sources. KECK, on other hand, consists of two 85 m separated 10.6 m telescopes and was largely used in nulling mode. However, since 2012 KECK is no longer operated as an interferometer but may be reactivated if funding is available. The LBTI consists of two relatively close (14.4 m separation) 8 m telescopes that can be operated in various modes such as nulling and Fizeau interferometry. However, its comparably small separation does not allow to reach angular resolutions such as the VLTI or CHARA.

Considering the previously mentioned advantage of densely sampled spatial frequencies, the Magdalena Ridge Observatory Interferometer (MROI) ([Creech-Eakman et al. 2016](#)) is a currently developed interferometer that will consist of ten telescopes with baselines between 7.8 and 340 m and will operate between 0.6 and 2.4  $\mu\text{m}$ . Even more ambitious, the recently founded Planet Formation Imager (PFI) project ([Monnier et al. 2016](#)) aims at approximately twenty telescopes with baselines of up to 20 km for the L, M and N band. However, at the moment this project is still far from being realized.

The beam combiners presented in this thesis are developed in the view of a potential new

#### 2.4. CURRENT AND FUTURE LANDSCAPE OF INTERFEROMETRIC FACILITIES<sup>19</sup>

instrument for the VLTI to obtain high angular resolution in the L and M bands combined with the light gathering capabilities of the VLTI. This region is not covered by any of the operational instruments but is targeted by the upcoming MATISSE instrument. However, empowered by the recent developments in mid-IR IO our aim is to equip the instrument with an IO beam combiner that as such provides higher accuracies on the interferometric observable  $\mu(\vec{B})$ .



## Integrated optics and Ultrafast Laser Inscription

Integrated optics (IO) can be viewed as the optical analogue of the electrical integrated circuit. Instead of electrons being conducted, photons are guided along so-called waveguides, similar as in an optical fiber, but on a chip with a fixed design. In recent years the coming together of astronomy and photonics has led to a new field coined astrophotonics in which photonic concepts are applied to astronomical instrumentation aiming at more stable and precise as well as smaller and flexible instruments<sup>1</sup>. In this work, we use the concept of IO for beam combination to replace bulk optics setups as in Fig 2.4 with on-chip solutions. See Fig. 1 in [Tepper et al. \(2017a\)](#) for a picture and sketch of such a chip.

In this chapter, I will first briefly introduce the optical waveguide and the coupling between them which is the basis for beam combination. Secondly, I will describe the manufacturing process of waveguides using Ultrafast Laser Inscription (ULI). Then, I will present different layouts for the on-chip combination and discuss their individual advantages and disadvantages as well as the stringent requirements that IO have to meet for astronomical beam combination. Here, I will mention the benefits and drawbacks of IO, in particular in comparison to bulk optics solutions. Finally, I will put this work into context by referencing to previous efforts in the field of mid-IR IO and point out some applications of ULI beyond astronomy.

### 3.1 Basics of optical waveguides

In this section, I will shortly recap some general properties of waveguides and mode coupling (see [Snyder & Love \(1983\)](#) for a textbook introduction). An optical waveguide is a medium (typically a cylindrical structure) of refractive index  $n_1$ , called the core in the following, embedded in another medium with refractive index  $n_2$ , called the cladding, with  $n_1 > n_2$ . This may either be realized in a flexible fiber or in a piece of bulk, then called integrated optics. The difference in refractive index is denoted by  $\Delta n = n_1 - n_2$ . Light can be guided in the core, which can be understood, on a lower level, by total internal reflection in the light ray picture. However, it is necessary to apply electromagnetic theory to understand essential features of waveguides. Solving the Helmholtz-equations, one finds that only a discrete number of modes is supported by the waveguide. The mode determines the radial intensity profile of the guided wave. The larger the difference in refractive index between the core and the cladding, the more confined the mode is in the core leading to reduced losses for curved waveguides ([Hunsberger 1982](#)). Importantly, a waveguide can be tailored in such a way to only support one mode

---

<sup>1</sup>see for example, Feature Issue: Bryant J. et al (Editors), 2017. Recent Advances in Astrophotonics, *Optics Express*, 25

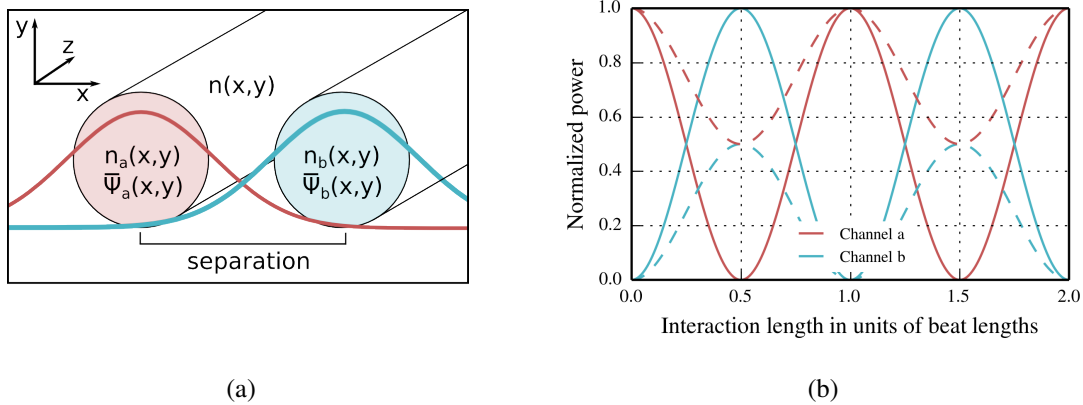


Figure 3.1: (a): The sketch shows the cross section of a composite waveguide of two identical waveguides. The red and blue curve, respectively, depict the mode of each waveguide in isolation. The cross-sections, separations and modes are not to scale but simply to illustrate. (b): The plot shows how power flows from one waveguide to the other as a function of the interaction length  $z$  for an identical pair of waveguides (solid lines) and for the asymmetrical coupler (dashed lines) with  $F = 0.5$ .

and is then said to operate single-mode, to which we will restrict ourselves in the following as it is the relevant case for interferometry (see Sec. 3.4). For cylindrical waveguides this fundamental mode takes the form of a near-Gaussian, as shown schematically in Fig. 3.1a or imaged in Fig. 5 in [Tepper et al. \(2017a\)](#). These modes cannot only be guided but also coupled to modes of neighboring or crossing waveguides, which is the basis for the on-chip beam combination, the key subject of this thesis. Different combining layouts are presented in Sec. 3.3. The basis for most combination schemes is evanescent mode coupling.

Evanescent coupling means that there is a nonzero flow of power between two waveguides although the cores of the waveguides do not overlap or come in physical contact, see Fig. 3.1a. Yet, the Gaussian-like mode field is not constrained to the region of the core but penetrates indefinitely into the cladding. Therefore, there is a nonzero interaction between neighboring waveguides depending on their separation and as a result power transfer may occur. In the following, I will treat the most simple case of two identical single-mode waveguides parallel to each other. Although the complete chip structures investigated in this thesis are more complex, they are still mainly based on evanescent coupling between parallel waveguides. The following mathematical treatment is adapted from [Snyder & Love \(1983\)](#).

The cross section of the composite two-waveguide structure is shown in Fig. 3.1a. Let  $n_a(x,y)$  and  $n_b(x,y)$  denote the refractive index profiles of each waveguide in isolation and  $n(x,y)$  the refractive index profile of the composite waveguide. In the perturbation analysis, it is assumed that the mode of the composite waveguide can be described by a superposition of the modes of each waveguide in isolation, denoted by  $\Psi_a(x,y)$  and  $\Psi_b(x,y)$ , respectively. This is true, if the waveguides are well separated, i.e. the mode of the one waveguide is weak in the cross section of the other waveguide, and if the waveguides are weakly guiding, i.e.  $\Delta n/n_2 \ll 1$ . All of the above restrictions are fulfilled by the waveguide structures in [Tepper et al. \(2017a\)](#) and [Diener et al. \(2017\)](#). Let  $P_a(z)$  and  $P_b(z)$  denote the power in the respective waveguides and let  $P_a(0) = 1$  and  $P_b(0) = 0$ , i.e. light is initially only injected into the first

port and the total injected power is normalized. The question now is how the power distributes in the two channels as a function of the interaction length  $z$ . Under the previous assumptions, it can be shown that the power in the respective channels follow the functions

$$P_a(z) = \cos^2(Cz) \quad \text{and} \quad P_b(z) = \sin^2(Cz) \quad (3.1)$$

as depicted in Fig. 3.1b, i.e. the power flows back and forth between the two waveguides. The difficulty is the calculation of the coupling coefficient  $C$ , which depends on the overlap of the unperturbed modes in the cross section of the second waveguide

$$C = k \frac{\int_{A_\infty} (n(x, y) - n_a(x, y)) \bar{\Psi}_a(x, y) \bar{\Psi}_b(x, y) dA}{\int_{A_\infty} \bar{\Psi}_a^2(x, y) dA} \quad (3.2)$$

in which  $k = 2\pi/\lambda$  denotes the wavevector and  $\lambda$  the free-space wavelength. In particular, it is difficult to evaluate these integrals as the cross sections  $n(x, y)$  of the laser-inscribed waveguides are not very accurately known. Still, it is insightful to notice that the power flow occurs back and forth with a so-called beating length, after which the total power is transmitted into the second waveguide and back again,  $z_b := \frac{2\pi}{C}$ . Also, it is important to note that  $C$  depends on  $k$  and that, therefore, the evanescent coupler is inherently a chromatic device. Often, a balanced 50/50 splitting is desired. This corresponds to an interaction length of  $(0.25 + 0.5l) \cdot z_b$ , with  $l = 0, 1, 2, \dots$ . The flattest wavelength response is achieved for  $l = 0$ . Since  $C$  is difficult to simulate, experimental parameter tests need to be carried out to find the right inscription parameters, waveguide separation and interaction length  $z$  to obtain the desired splitting ratio. Polarization effects were neglected in this analysis and can be found in the respective literature ([Snyder & Love 1983](#)).

It is shown that in ULI structures, the successive inscription of waveguides introduces stress in the substrate such that neighboring waveguides may not be fully identical and the description above no longer holds ([Diener et al. 2016](#)). As a consequence of that, Eqs. 3.1 are multiplied by a factor  $F$  ( $0 < F < 1$ ), which depends on the difference in propagation constants between the two waveguides (Eq. 29-8 in [Snyder & Love \(1983\)](#)). Thus, the power transfer is damped, see Fig. 3.1b.

## 3.2 Physics of Ultrafast Laser Inscription

In this subchapter, I will present how waveguides can be manufactured in dielectric bulk by means of Ultrafast Laser Inscription (ULI). The material for this subchapter was taken from [Osellame et al. \(2012\)](#) and [Gross & Withford \(2015\)](#), which I both recommend to the interested reader. The technique of ULI was originally proposed by [Glezer et al. \(1996\)](#) in the context of data storage and [Davis et al. \(1996\)](#) for the inscription of waveguides.

The manufacturing process of IO by ULI is depicted in Fig. 3.2. A femtosecond pulsed laser beam is tightly focused a few hundred micrometers beneath the surface of the substrate and introduces a localized, permanent structural change in the material. This may locally introduce a positive or negative change in refractive index  $\Delta n$  in the focal volume of the beam. By translating the substrate while being irradiated, any arbitrary line of refractive

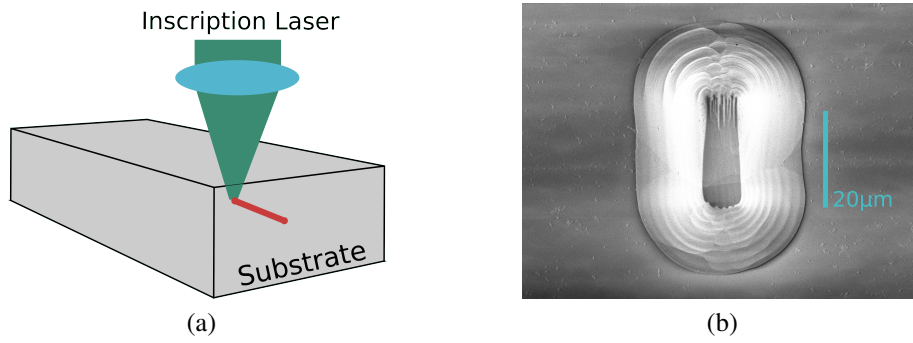


Figure 3.2: (a): The principle of ULI. An intense laser is focused beneath the sample's surface and introduces a structural modification, which may result in a change of refractive index. By translating the sample, waveguides (red line) can be inscribed. (b): SEM image of the modified cross-section. The waveguide was inscribed using the multipath technique, i.e. writing several adjacent tracks to create a homogeneous area. The white ring is a result of the polishing after inscription to make the cross-section visible. Image taken by Romina Diener, University of Jena.

index change can be inscribed in three dimensions. If the laser induces a positive change of refractive index, the core of the waveguide is written. If the laser induces a negative change, the cladding of the waveguide is written, so that the laser writes around a cylindrical core. In that case the core remains mostly unaffected .

In this work, I aim to exploit this technique and inscribe beam combiners in mid-IR transparent materials. It shall be noted that there is yet no complete theoretical picture of the interaction between the material and the laser pulses. So far, laser writing has relied on a more heuristic approach in finding the suitable inscription parameters. From experimental findings and from well-known nonlinear absorption processes, a notion of the underlying physics was constructed which will be briefly summarized in the following.

The structural change of the material due to high laser intensities ( $\approx 10\text{TW}/\text{cm}^2$ ) is based on strong nonlinear absorption. The physics of this process can be subdivided into three steps: the generation of free electron plasma, energy relaxation and the resulting modification of the material, which is schematically shown in Fig. 3.3. The initial generation of free electron plasma is a well understood process and is itself based on three nonlinear processes: multiphoton ionization, tunneling photoionization and avalanche photoionization. Multiphoton ionization is the dominant process for low laser intensities and high frequencies. The substrate material is chosen to be transparent at the inscription laser wavelength so that a single photon with frequency  $\nu$  does not carry sufficient energy to move a valence electron to the conduction band. Yet, the simultaneous absorption of  $n$  photons may occur and provide enough energy to promote an electron if  $nh\nu > E_{bandgap}$  with  $E_{bandgap}$  being the bandgap energy. At higher laser intensities and lower frequencies the potential barrier can be distorted by the electrical field carried by the laser light. This enables direct band to band transitions by quantum tunneling, which is then referred to as tunneling photoionization. Formally, the transition between the two regimes is described by the Keldysh parameter (Keldysh 1965)

$$\gamma = \frac{\nu}{e} \sqrt{\frac{m_e c n \epsilon_0 E_{bandgap}}{I}} \quad (3.3)$$

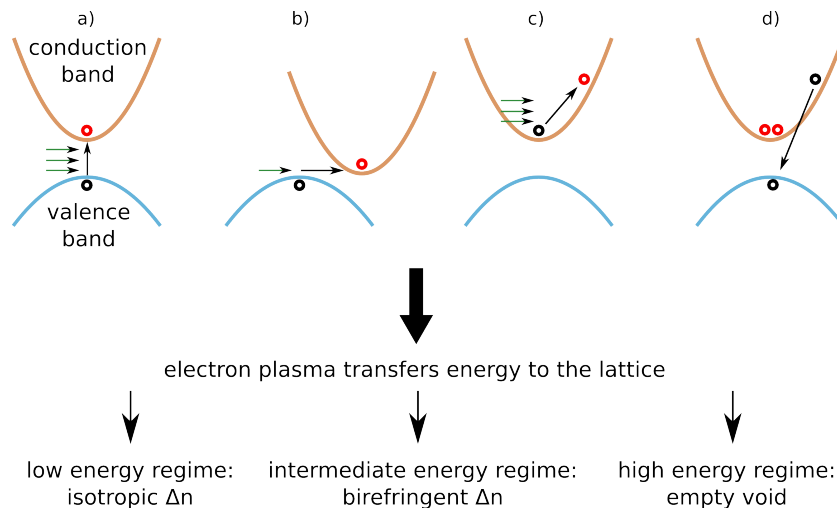


Figure 3.3: Processes following the laser irradiance. The black dot depicts the electron state before and the red after. Top row: Electrons are promoted to the conduction band by nonlinear absorption, multiphoton ionization (a) and quantum tunneling (b). Once the electron is in the conduction band, it can absorb further photons by free-carrier absorption (c). If the conduction band electron has an energy larger than the conduction band minimum plus the bandgap, it can promote another electron to the conduction band (d). Once sufficient electrons are in the conduction band, a highly absorptive plasma is created and optical breakdown occurs. As the plasma recombines, the electrons transfer their energy to the lattice. The bottom row depicts the different resulting structural modifications depending on the irradiance intensity. Adapted from [Osellame et al. \(2012\)](#).

in which  $\nu$  is the laser frequency,  $e$  the electron charge,  $m_e$  the effective electron mass,  $c$  the speed of light,  $n$  the refractive index of the material,  $\epsilon_0$  the free-space permittivity and  $I$  the laser intensity at the focus. For  $\gamma$  much greater than 1.5, multiphoton ionization dominates while for  $\gamma$  much less than 1.5 tunneling ionization occurs. [Schaffer et al. \(2001\)](#) could show that for waveguide inscription in fused silica and  $\text{CaF}_2$  at inscription wavelengths of 400 nm and 800 nm,  $\gamma$  is between 1.2 and 2.5, indicating that both processes are relevant for the generation of electrons in the conduction band.

Once electrons have been transferred to the conduction band by the two mechanisms described above, they can further absorb light by free carrier absorption. If such an electron has absorbed a sufficient number of photons, the energy of this electron can be larger than the conduction band minimum plus the bandgap and can ionize another electron from the valence band. The result are two electrons near the conduction band minimum. This process can repeat and amplify itself and is called photoionization avalanche. If the density of electrons in the conduction band reaches a critical value (about  $10^{21}/\text{cm}^3$  at  $1 \mu\text{m}$  laser wavelength), the plasma formed by the electrons becomes highly absorptive and optical breakdown occurs. In glass, this corresponds to a laser intensity of about  $10^{13} \text{ W}/\text{cm}^2$ . The electrons then pass their energy via electron-phonon interaction to the lattice, a process that occurs on timescales of 10 ps, much longer than the duration of the femtosecond laser pulses. As a consequence, a large amount of energy is deposited leading to a highly localized structural modification.

The structural modification and refractive index change caused by the lattice heating is not

well understood but can empirically be subdivided into three regimes that were experimentally found: a smooth refractive index change, a form birefringent refractive index modification and microexplosions causing empty voids in the material. Typically, these three regimes occur in this order with rising laser power (Itoh et al. 2006). In general, however, the laser and inscription parameters as well as the properties of the substrate material determine the type of modification.

In the case of the smooth refractive index change, a densification due to melting and/or the creation of color centers<sup>2</sup>(Dekker et al. 2010) lead to the change in refractive index, which can either be positive or negative in sign. This regime is found when the laser power is just above the threshold for optical breakdown (about  $10^{13}\text{W/cm}^2$ ) and is the preferred one for inscribing optical waveguides.

At higher intensities, a non-isotropic birefringent refractive index is found due to self-alignment of nanogratings perpendicular to the electrical field of the laser, which is discussed in Beresna et al. (2014). This may be explained by the interference of the laser field and the electron plasma wave (Shimotsuma et al. 2003). Such nanogratings in fused silica have been nicely imaged by Hnatovsky et al. (2006). Since the nanogratings are a potential source for uncontrolled birefringence, this regime is not ideal for writing beam combiners (c.f. Sec. 3.4).

At even higher laser intensities above  $10^{14}\text{W/cm}^2$  a shockwave from the focal point is created that leaves hollow cores. This regime was used by Glezer et al. (1996) for data storage inscription but is not suitable for inscribing optical waveguides.

Additionally, another important distinction needs to be made between the thermal and athermal regime. Although the duration of the laser femtosecond pulses is well below the time needed for the heat to diffuse away (few  $\mu\text{s}$ ), subsequent pulses may be within the relaxation time depending on the repetition rate of the laser (Gattass et al. 2006).

In the athermal regime, low repetition rates of a few kilohertz with high energy pulses of around  $1\ \mu\text{J}$  are used. In this pulse-by-pulse modification, the spatial extent of the modified region reflects the intensity distribution of the laser beam. Maintaining a smooth overlap between the consecutive pulses slows down the writing speed down to micrometers per second.

In the thermal regime, repetition rates between hundreds of kilohertz up to a few megahertz are used. Due to the insufficient time for the heat to diffuse, melting occurs and leads to circular cross sections larger than the dimensions of the laser focal spot (Itoh et al. (2006) and references therein). Due to the isotropic nature of the heat diffusion, the creates a circular cross-section. A high repetition rate offers faster writing as well as circular symmetric and low-loss waveguides and is therefore the preferred approach (Eaton et al. 2005).

The IO studied in this thesis are based on a chalcogenide glass GLS (Gallium Lanthanum Sulfide) and on a fluoride glass ZBLAN ( $\text{ZrF}_4\text{-BaF}_2\text{-LaF}_3\text{-AlF}_3\text{-NaF}$ ). Both chips were written in the thermal regime. The ZBLAN chip in Tepper et al. (2017b) and the GLS chips in Diener et al. (2017) were inscribed by the previously discussed smooth refractive index change. This is not fully clear for the GLS chips in Tepper et al. (2017a), however, the creation of nanogratings is excluded due to the circular polarization of the inscription laser. In the case of GLS the change in refractive index is positive, i.e. the core of the waveguide is written, and in the case of ZBLAN the change in refractive index is negative, the cladding is written.

---

<sup>2</sup>A color center is a crystallographic defect that absorbs visible light due to an anionic vacancy that is filled by one or more electrons.

Both chips are written using the so-called multipath technique, meaning that several tracks of laser damaged paths are inscribed in order to create a large and homogeneous area. More specifications on the inscription parameters can be found in the respective publication.

For completeness, it should be mentioned that IO can also be manufactured by other means than ULI. The most common approach is lithography in which a geometric pattern is created by exposing the light-sensitive substrate through a previously manufactured photomask. Lithography has the advantage that the complete waveguide structure is imprinted simultaneously and therefore cannot suffer from unstable conditions during the inscription process as it could be the case for ULI being a serial manufacturing process. Waveguides can also be manufactured by means of ion-exchange which can be subdivided into its most popular forms, titanium in-diffusion and proton-exchange. For infrared waveguides, this technique has been mostly applied to lithium niobate ( $\text{LiNbO}_3$ ). In Ti in-diffusion, a thin (10-100 nm) Ti film is deposited, which then diffuses over several hours at roughly 1000 K into the substrate. If 1D structures such as waveguides ought to be written, masking technology is needed for the inscription of channel waveguides similar to photolithography. In the proton-exchange process, lithium ions in  $\text{LiNbO}_3$  are replaced by protons. The fabrication technique is similar to Ti in-diffusion but proton-exchanged waveguides only support the extraordinary, i.e. parallel to the optical axis, polarization of the light. A more detailed description of this technology is found in [Korkishko & Fedorov \(1999\)](#). The advantages of lithography and ion-exchange is that larger  $\Delta n$  can be introduced, which results in better mode confinement and smaller losses. However, both lithography and ion-exchange are typically restricted to planar structures which, lead to undesired waveguide crossovers and strongly constrain the waveguide design. In particular, for the beam combination of multiple telescopes 3D arrays become more important (e.g. Fig. 3.4 bottom right) which are easily achievable by ULI. Furthermore, ULI is a relatively cheap technique once the femtosecond laser system is installed and does not need clean room facilities. Also, no masks need to be developed for inscribing the chip, which allows rapid and convenient testing of prototypes, which is suitable for the custom demands in astronomical applications.

### 3.3 On-chip beam combination schemes

After having explained how waveguides can be manufactured, I want to propose different types of beam combination layouts that can be inscribed into the substrate. Figure 3.4 shows an overview of different beam combination architectures for two- and four-telescope combination that are based on evanescent coupling and Y-Junctions which will be discussed in the following.

- Y-Junction (Fig. 3.4 top left): The Y-Junction is the most simple combiner. Its splitting ratio is achromatic but at least 50% of the light is radiated out at the junction and is therefore an inherently lossy device.
- $2 \times 2$  coupler (Fig. 3.4 top center): The  $2 \times 2$  coupler relies on evanescent coupling. As soon as the waveguides converge and run parallel with a decreased separation for some interaction length, we are in the previously discussed scenario (c.f. Fig. 3.1a). Ideally, a  $2 \times 2$  coupler produces two combined outputs with a  $\pi$  phase shift due to the conservation of energy. Clearly, the design is more difficult than the Y-Junction as the design parameters

(separation, interaction length) have to be carefully chosen in order to determine the desired fraction of power flow. Additionally, as shown before, the evanescent  $2 \times 2$  coupler is an inherently chromatic device. This can in theory be compensated by writing intentionally asymmetric waveguides (Hewlett et al. 1996), so that the power transfer is damped with  $F = 0.5$  (see end of Sec. 3.1 and Fig. 3.1b) and the coupler shows a wavelength-flattened response at the 50/50 splitting. However, this is far from straight forward to implement by ULI means as it requires extreme control of the writing process. Also, asymmetric couplers may introduce differential dispersion, c.f. Sec. 3.4, and therefore may decrease the instrumental contrast. The advantages are that, compared to the Y-Junction, there is no inherent 50% loss and that the  $2 \times 2$  coupler is the building block of the ABCD combiner described next. The coupler presented in Tepper et al. (2017a) is such a  $2 \times 2$  coupler. The coupler presented in Tepper et al. (2017b) follows a slightly different principle. It is called zero-gap directional coupler (Goel & Chang 1987), meaning that the cores of the waveguides overlap in the interaction area, see Fig. 1(b) in Tepper et al. (2017b). Such a coupler is not based on evanescent coupling anymore but in principle still produces two  $\pi$  phase shifted outputs and is chromatic. Therefore, in its functionality, it resembles the evanescent  $2 \times 2$  coupler.

- 2T ABCD (Fig. 3.4 top right): The so-called ABCD combiner for two telescopes consists of reverse Y-Junctions and  $2 \times 2$  couplers (Benisty et al. 2009). An additionally inscribed  $\pi/2$  phase shift creates (together with the natural  $\pi$  phase shifts of the  $2 \times 2$  couplers) four outputs that are  $\pi/4$  phase shifted with respect to each other. Therefore, with a single frame near zero OPD, the contrast and phase can be estimated without scanning the OPD as the interferometric signal is sampled at four points (hence the name ABCD) and can be fully reconstructed. The artificial  $\pi/2$  phase shift can be created by the alteration of the propagation constants by changing the writing speed or by creating a small detour (note that such phase shifts are not in general achromatic). The couplers in Diener et al. (2017) are based on the ABCD method and were using a monochromatic source at  $3.39 \mu\text{m}$ .
- 4T all-in-one (Fig. 3.4 bottom left): The most simple architecture for a four-telescope on-chip combiner. As for the Y-Junction, such a device would radiate out at least twice 50% of the light, i.e. a maximum transmission of 25%. Whereas the inscription is comparably easy, the visibility estimation becomes more difficult as the interferograms from all baseline pairs are superimposed. In order to disentangle, the respective fringe patterns from the telescope pairs must be scanned at distinct speeds. Then, the visibility can be estimated in the Fourier space, as the fringe peaks correspond to different frequencies.
- 4T ABCD (Fig. 3.4 bottom center): The four-telescope ABCD coupler is basically the extension of the two-telescope ABCD. Such a coupler has been successfully implemented in the PIONIER (Benisty et al. 2009; Le Bouquin et al. 2011) and GRAVITY (Gravity Collaboration et al. 2017) instruments at the VLTI using lithographic techniques for the H&K band and K band, respectively. While this approach has proven very successful, it is not yet clear whether this is the optimal solution for ULI inscribed waveguides as it requires extremely high repeatability for such a fine-tuned and complex chip architecture.
- 4T zig-zag array (Fig. 3.4 bottom right): The zig-zag array belongs to the class of discrete beam combiners (DBC). DBCs are periodic arrays of evanescently coupled waveguides (Diener et al. 2016). Thanks to discrete diffraction, the injected light fields spread out as

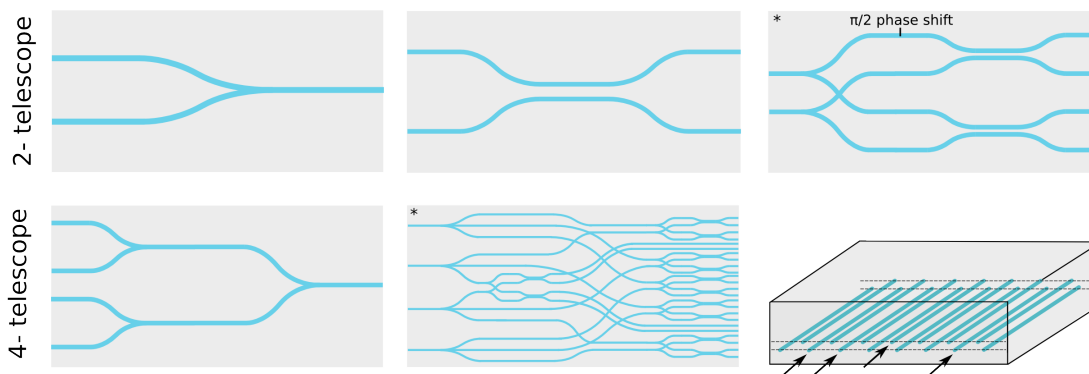


Figure 3.4: An overview of different beam combination architectures for two- and four-telescope couplers. Light injection is from left to right. From top left to bottom right: Y-Junction, 2x2 coupler, ABCD coupler, all-in one coupler, 4T ABCD coupler, zig-zag coupler. The zig-zag coupler is just a schematic illustration. The actual number of waveguides and input configuration may be different, see [Diener et al. \(2017\)](#) for details. (\* adapted from [Benisty et al. \(2009\)](#))

they travel through the sample and are superimposed in the output channels. The relation between the input and output fields must be experimentally calibrated by the so-called P2VM (pixel-to-visibility matrix). Then, from the measured output patterns one can extract the input fields from which their respective complex visibilities can be derived. A DBC does not need to take the form of a zig-zag array. Another proposed layout for a DBC would be a square array of waveguides such as the 4×4 array in [Saviauk et al. \(2013\)](#). In [Diener et al. \(2017\)](#), the calibration of the V2PM and the visibility retrieval is explained in detail and a four-telescope zig-zag array is tested for beam combination.

Certainly, a major question for the future of this project is which architecture is the optimal one for a four-telescope beam combiner. This is discussed in the view of the results of the papers in Chap. 7.

### 3.4 Requirements of integrated optics chips in astronomy

Integrated optics chips have to meet a number of stringent requirements for the application in astronomical instruments. Independently of the IO chip design, such combiners should exhibit high throughput and provide a stable interferometric output with high interferometric contrast<sup>3</sup>. This, in turn, depends crucially on parameters discussed in this section. Bulk optics beam combiners are the conventional alternative to IO. Therefore, I will also comment on the bulk optics cases in the subsections.

#### Transparency

The first question is the desired transparency range and, thereby, the choice of substrate material. One of the most common materials for IO has been silica. In this thesis, however,

<sup>3</sup>A lowered (but stable) instrumental contrast can be calibrated out but lowers the SNR due to the decreased interferometric signal.

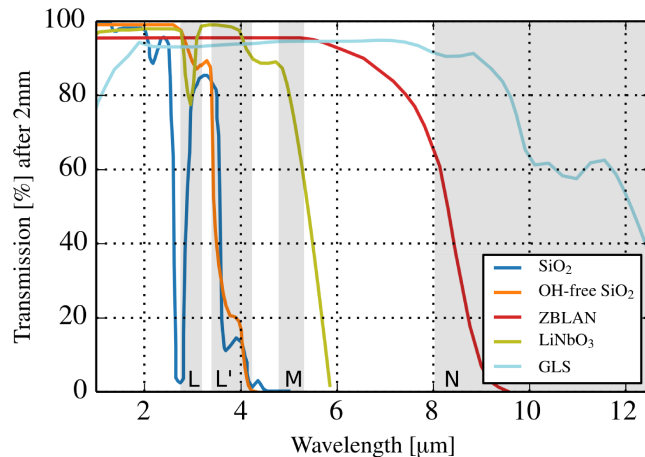
Figure 3.5: Transmission for  $\text{SiO}_2^a$ , OH-free  $\text{SiO}_2^a$ , ZBLAN<sup>b</sup>,  $\text{LiNbO}_3^c$  and GLS<sup>d</sup>. Fresnel losses are computationally removed. The gray shaded areas depict the astronomical bands L, L', M and N.

<sup>a</sup><http://www.almazoptics.com>

<sup>b</sup>Parker (1989)

<sup>c</sup><http://www.impex-hightech.de>

<sup>d</sup><https://chalcogenide.net>



I want to extend the operation of IO to longer wavelengths beyond  $3 \mu\text{m}$ , where silica is no longer transparent. Although OH-free silica is transmissive up to  $3.3 \mu\text{m}$ , writing waveguides in this substrate has evidenced strong differential dispersion<sup>4</sup>. Also, the important L' and M band atmospheric windows are still not accessible by OH-free silica, see Fig. 3.5. Therefore, other kinds of materials need to be considered.

A number of glasses and few crystals have been tested for laser inscription that are transparent beyond  $3 \mu\text{m}$ , which can be grouped into fluoride<sup>5</sup> and chalcogenide glasses<sup>6</sup> with the exception of germanate and the crystal lithium niobate ( $\text{LiNbO}_3$ ). A more detailed overview of substrate materials which are suitable for ULI in the mid-IR can be found in Arriola et al. (2017). Figure 3.5 shows the transparency range of some mid-IR materials including the ones used in this thesis (GLS and ZBLAN). Notably, GLS is the only material which is still transmissive around  $10 \mu\text{m}$  and would therefore allow observations in the N band.

In comparison, for bulk optics, there are plenty of wide-band mid-IR optics such as mirrors and beam splitters readily available at relatively low cost.

## Losses

The overall losses are undoubtedly a detrimental property for a typically photon-poor application as astronomy. The losses in an IO chip can be subdivided in coupling losses, Fresnel losses and propagation losses as well as bending losses. Coupling losses are due to the mode mismatch between the Airy disc<sup>7</sup> arising from the telescope aperture and the waveguide mode. The maximum coupling for a Gaussian-like waveguide mode is about 80% (Toyoshima 2006). This loss is practically impossible to circumvent. Fresnel losses are caused by the mismatch of the refractive index of air and the substrate material. Those losses are typically lower for fluorides than for chalcogenides due to their lower refractive index, although this effect can be minimized by the application of antireflection (AR) coatings.

<sup>4</sup>Laurent Jocou, Institut de Planétologie et d'Astrophysique de Grenoble (IPAG), Université Grenoble Alpes, personal communication

<sup>5</sup>Fluorides are materials whose basic constituent is fluorine.

<sup>6</sup>Chalcogenides are materials that contain at least one of the following: sulfur, selenium or tellurium.

<sup>7</sup>The Airy disc is the point spread function of a circular aperture, i.e. the best attainable image of a point source.

The dominant propagation losses in straight waveguides are due to scattering. Scattering may occur inside the volume of the core or at the core-cladding surface. Volume scattering is caused by imperfections and the loss per unit length is proportional to the number of imperfections per unit length. Surface scattering is caused by surface roughness of the core-cladding interface. Absorption losses are comparably negligible in glasses (Hunsberger 1982).

In bent waveguides, radiation out of the waveguide occurs due to the distortion of the optical field as the waveguide bends. An expression for the attenuation of the power  $P(z)$  in the waveguide as a function of the distance traveled  $z$  in a bend with radius  $R$  is given by

$$\alpha := \frac{1}{P(z)} \frac{dP(z)}{dz} = C_1 \exp(-C_2 R) \quad (3.4)$$

in which  $C_1$  and  $C_2$  are constants that depend on the dimensions of the waveguide and the mode, which are specified in Hunsberger (1982). Importantly,  $C_2$  is proportional to  $\Delta n$ , meaning that bend losses are decreased for higher  $\Delta n$  and stronger mode confinement. Also, the attenuation is larger for smaller bend radii  $R$ . The level of bending losses are highly important as they decide over the level of complexity that can be implemented into the chip needed for architectures such as the previously discussed ABCD scheme. Radiation out of the guiding core does not only decrease the throughput but also adds a potentially partially coherent background to the output signal which is difficult to correct for.

For bulk optics, only Fresnel losses apply but can be kept to a minimum using AR coatings.

## Modal behavior

At a given wavelength, the number of supported modes depends basically on the size of the waveguide cross-section and the refractive index difference  $\Delta n$ . One of the main features of IO is their function as spatial filters if they are single-mode, i.e. support only one mode for each polarization. This means that any phase distortion of the incoming wavefront, due to atmospheric turbulence for instance, is translated into the (Gaussian-like) mode that is supported by the single-mode waveguide. This greatly improves the stability and the instrumental contrast and eliminates waveguide dispersion<sup>8</sup>. However, this puts limitations on the maximum size and refractive index change of the waveguide as they become multimode with increasing size and refractive index. The  $V$  parameter of a waveguide is defined as

$$V = 2\pi \frac{a}{\lambda} \cdot \text{NA} \quad (3.5)$$

in which  $a$  is the core radius and NA is the numerical aperture given by  $\text{NA} = \sqrt{n_1^2 - n_2^2}$ . The number of modes increases with  $V$  and, therefore, increases with the change in refractive index,  $\Delta n$ , and the size of the waveguide. For  $V < 2.405$ , the waveguide operates in single-mode. However, since a larger refractive index change leads to a stronger mode confinement and reduces bend and propagation losses as discussed above, a trade-off has to be made so that waveguides are typically best to operate close to the multimode regime at the desired wavelength.

---

<sup>8</sup>Waveguide dispersion occurs in multimode waveguides as different modes have different propagation constants.

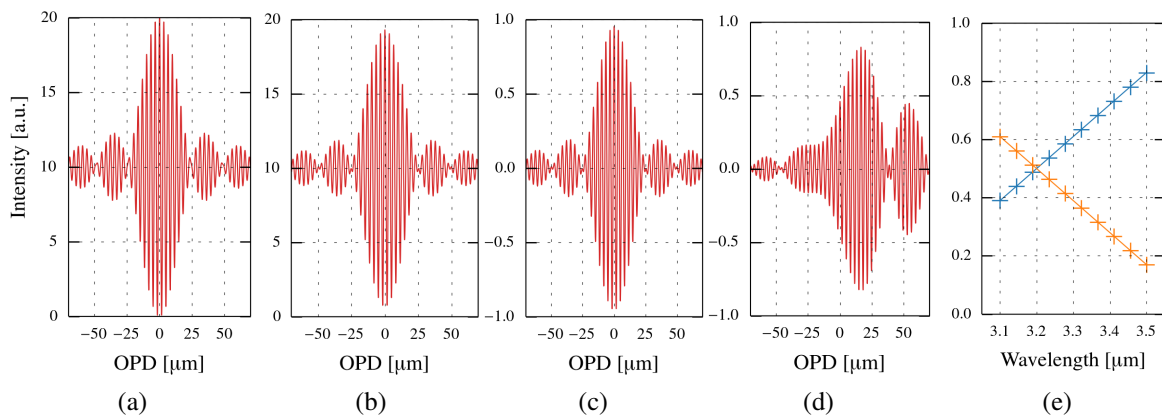


Figure 3.6: This figure shows a wide-band interferogram for a point source, i.e. visibility of one, synthesized out of 10 wavelengths from 3.1 to 3.6  $\mu\text{m}$ . In the first plot (a), the power of the two interferometric arms is balanced for all wavelengths,  $I_1 = I_2 = 5$  (in arbitrary units). The raw contrast of this interferogram is one. In plot (b), the two arms are not balanced with 61% in one and 39% power in the other arm. Additionally, this ratio depends on the wavelength, see plot (e). As a consequence, the raw contrast drops to 93% (c.f. Eq. 2.4). In plot (c), the photometric correction is applied (Eq. 2.5). This raises the contrast back to 95%. It does not reach back to 100% as it cannot account for the fact that the power ratio is wavelength dependent but only that the *integrated* power over the band is unbalanced. Finally, in plot (d), the effect of strong dispersion is qualitatively demonstrated. Here, also the shape of the interferogram is affected and the contrast drops to 83%.

The absence of modal filtering is the biggest disadvantage of bulk optics solutions compared to IO. Therefore, the achieved instrumental contrast and the accuracy on the measured contrast is lower.

## Splitting Ratio

The ideal IO beam combiner splits and combines the input beams achromatically. The effect of an unbalanced and chromatic splitting ratio on the measured contrast is shown in Fig. 3.6. A chromatic splitting ratio, i.e. different across the spectrum, cannot be corrected for by naive photometric correction (c.f. Eq. 2.5) and reduces the interferometric contrast depending on the steepness of the splitting ratio as a function of wavelength. If the IO output is dispersed before imaged onto the camera (as usual for most instruments), the photometric correction can be applied to each spectral channel to reconstruct the visibility. Additionally, the splitting ratio can be a function of the polarization; an effect which has been overlooked in most publications as well as in [Tepper et al. \(2017a,b\)](#). As a matter of fact, measurements performed after the publication of the papers on a  $2 \times 2$  coupler have shown that the splitting ratio can change by 15% when going from TE to TM polarization.

The bulk optics equivalent is the beam splitter which can be used to split and recombine beams. Beam splitters are available for a wide-transparency range in the mid-IR off-the-shelf.

## Birefringence and cross-talk

In optical waveguides, birefringence means that the refractive index, and therefore propagation constant, is different for different polarizations. This can be due to the non-circular geometry of the waveguide cross-section (c.f. 3.2b) or due to impurities and defects in the substrate material that may produce additional birefringence. As an example for a two-telescope combiner, if birefringence is present but identical for both waveguides, the zero OPD for TE and TM polarized light is identical and the interferometric contrast is unaffected. On the other hand, if the differential birefringence is nonzero, the respective interferograms for TE and TE modes would be shifted and as a result decreases the contrast.

In an ideal waveguide, the TE and TM modes are orthogonal and no cross-talk between the two modes occurs. However, due to imperfections in the waveguides, power may be transferred between the TE and the TM modes. In the most extreme case for instance, light is launched into the waveguide in TE mode and leaves as TM mode. Now, if the other waveguide is fully polarization-maintaining, the interferometric signal is composed of one TE mode channel and TM mode channel. As a result, the electrical fields cannot add up or cancel each other out anymore and the contrast is reduced to zero. Similar to birefringence, cross-talk is not crucial as long as this behavior is identical in both waveguides. In addition, the amount of cross-talk may depend on the wavelength (Penninckx & Beck 2005). As opposed to IO, fibers may exhibit a time-dependent cross-talk as they are more sensitive to external variables such as stress, bendings and temperature.

In bulk optics setups, the individual beams are reflected and transmitted by several optical components which can alter the state of polarization and degrade the contrast (Buscher et al. 2009). In the case of the MATISSE instrument, this results in a contrast loss of 3%<sup>9</sup>. A common solution to regain high contrast, at the cost of a lower signal-to-noise ratio, is to split the polarizations into TE and TM modes and treat them individually.

## Dispersion

Dispersion means that the refractive index and, therefore, the propagation constant depends on the wavelength. If the dispersion in both interferometric arms is nonzero but equal, then the optical path difference (OPD) remains unaffected for all wavelengths. Consequently, the interferometric contrast is not decreased. Yet, if the dispersion in the two arms is different, i.e. differential dispersion is nonzero and the zero OPD is chromatic, the broadband contrast is decreased and the shape of the interferogram is affected, qualitatively shown in Fig. 3.6d. The degradation in contrast can be related to the phase curvature<sup>10</sup>, that is the second derivative of the phase  $\Phi$  with respect to the wavenumber  $\sigma$

$$\frac{d^2\Phi}{d\sigma^2} = -2\pi c\lambda^2 \cdot (L\Delta D + D\Delta L) \quad (3.6)$$

in which  $L$  is the length of interferometric channel,  $\Delta L$  the difference in lengths,  $D := \frac{d\tau_G}{d\lambda}$  the dispersions parameter, i.e. the derivative of the group delay with respect to wavelength, and  $\Delta D$  the difference in dispersion parameter between the two interferometric channels (Coudé

<sup>9</sup>Alexis Matter, Université Côte d'Azur, personal communication

<sup>10</sup>A linear dependency of the phase in wavenumber is not relevant as it corresponds to a global shift of the interferogram and does not alter the contrast or shape.

du Foresto et al. 1995). One can see that dispersion arises from either a difference in length or difference in dispersion parameter in the two arms.

Controlling dispersion is one of the most critical aspects in IO as it requires a highly repeatable writing process. So far many groups could achieve high monochromatic contrasts in IO (Martin et al. 2014; Ródenas et al. 2012; Labadie et al. 2011) but failed to produce high-contrast wide-band mid-IR interferograms. In bulk optics setups, similarly as for the birefringence, the individual beams can accumulate differential dispersion with respect to each other due to the finite thicknesses of the optical components such as the beam splitters. A common solution to this problem is to disperse the light and process the interferograms separately in each wavelength channel.

Bulk optics are convenient as they are readily available off-the-shelf for almost any wavelength range and show reasonably flat achromatic responses. However, IO provide a more stable instrumental transfer function. Once installed, IO need no further alignment, which proves to be a great advantage in practice. Also, any effects of differential dispersion or birefringence, if present, can be calibrated out. Bulk optics, on the other hand, are sensitive to thermal and mechanical disturbances, which leads to larger error bars on the measured visibilities. As an example, whereas error bars on the measured visibilities using the IO based instrument PIONIER are on the order of 2-3% (Kluska et al. 2016), the error bars of an observation using the bulk optics based AMBER instrument can be on the order of 10% or more (Renard, S. et al. 2010).

### 3.5 Previous and related works

The advantages of IO for long-baseline interferometry were first discussed in Malbet et al. (1999). In the following years, the IO concept was further studied and led to the first on-sky observation five years later using IO (Lebouquin et al. 2004) and, finally, resulted in the four-telescope beam combiner in the VLTI instrument PIONIER (Le Bouquin et al. 2011). IO is now accepted as an established platform for beam combination by the interferometric community and has been implemented in the recently commissioned VLTI instrument GRAVITY (Gravity Collaboration et al. 2017). However, those previous efforts were designed for the H and K bands and could therefore adapt a mature technology that has been developed by the telecommunications industry for many years. For instance, the about-to-be commissioned VLTI instrument MATISSE, which operates in the L, M and N bands, is still based on bulk optics beam combination. The interest in IO for mid-IR astrophysics started to develop about ten years ago.

First mid-IR straight waveguides were produced by etching and tested at 10.6  $\mu\text{m}$  (Labadie et al. 2006; Vigreux-Bercovici et al. 2007). Labadie et al. (2011) created Y-Junctions for 10  $\mu\text{m}$  wavelengths by laser writing in chalcogenide  $\text{As}_2\text{Se}_3$ <sup>11</sup>. The ULI approach was then put forward by Ródenas et al. (2012) and Arriola et al. (2014) in which channel waveguides, 2x2 couplers and tricouplers were inscribed in chalcogenide glasses for 3.39  $\mu\text{m}$  and 10.6  $\mu\text{m}$ . Gross et al. (2015) used ULI to introduce a negative change in refractive index in ZBLAN glass and successfully inscribed 2x2 couplers with a depressed cladding.

<sup>11</sup>This laser writing work relied on the inscription into a thin  $\text{As}_2\text{Se}_3$  film using a continuous wave laser where the structural modification is due to photodarkening.

At the same time, etching and lithography could demonstrate the manufacturing of low-loss rib channel waveguides (Ma et al. 2013) and a multimode-interference coupler (MMI)<sup>12</sup> in chalcogenide glass (Goldsmith et al. 2017). Using titanium-diffusion, waveguides were realized in lithium niobate glass. In this material, the electro-optic effect was exploited so that by applying voltage to on-chip electrodes the OPD could be altered and the interferogram scanned on-chip. However, Martin et al. (2014) evidenced large propagation losses of 16 dB/cm as well as low broadband contrast which is impractical for astronomical interferometry .

A completely different approach to overcome the deficiency of suitable optics/photonics and detectors as well as the strong thermal background in the mid-IR regime is proposed in Szemendera et al. (2017). Using sum frequency generation process, monochromatic light at 3.39  $\mu\text{m}$  was successfully converted down to 810 nm and interferometrically combined. Monochromatic contrasts of about 95% were achieved down to the photon counting regime. At the moment the conversion efficiency of about  $1.5 \cdot 10^{-5}$  and the spectral acceptance of the non-linear crystal of 3 nm are relatively poor and limit astronomical applications. However, if the efficiency can be increased, this concept may reduce the need for mid-IR optics after all.

To my knowledge, so far no paper could report a high (>90%) interferometric contrast over a broad spectral range in the mid-IR. This, in part, constitutes the novelty of the papers Tepper et al. (2017a) and Tepper et al. (2017b) as a high broadband instrumental contrast is the key feature of any future IO based interferometric instrument.

## 3.6 Applications beyond astronomy

The applications of ULI in general and ULI in mid-IR materials go beyond astronomy. As an example, in medicine and biology, the mid-IR is a valuable spectral region as it encompasses the fundamental vibrational absorption signatures of molecular species (Seddon 2011). Every organic molecule displays unique spectral fingerprints in this region. Therefore, mid-IR spectroscopy allows the detection of disease markers, emerging pollutants or toxic chemicals without the need of prior labeling through fluorescence of the molecule (Adam et al. 2015). Mid-IR microsensors based on IO would be a cheap, compact and robust solution that could detect changes in intensity, wavelength, phase and polarization. Additionally, IO can also sense evanescent fields, i.e. probing the external medium surrounding the waveguide. As a concrete example, Baudet et al. (2017) manufactured chalcogenide based IO for the detection of pollutant molecules in water by evanescent field sensing. To my knowledge, such studies have so far been based on conventional planar fabrication techniques.

Another application of ULI is the manufacturing of so-called Lab-on-chips (LOCs) in which microfluidic channels transport mix, separate, make react and analyze small portions of the substances under investigation (Osellame et al. 2012). In this case, ULI is not exploited for the inscription of optical waveguides but the creation of hollow channels. This can be achieved as follows: The sample is irradiated with the femtosecond laser in the second birefringent regime (c.f. Sec. 3.2). Then, the laser-modified region is etched by a hydrofluoric acid solution in water. Since the laser irradiation leads to an increased etching rate by two orders of magnitude, microchannels can be tailored. ULI now offers the opportunity to combine the inscription of microfluidic channels and optical waveguides in the same so-called

---

<sup>12</sup>An MMI is a 2x2 coupler that does not rely on evanescent coupling but has a large common multimode interaction area in which the input fields are mixed.

optofluidic chip. [Osellame et al. \(2007\)](#) inscribed microchannels and optical waveguides using the same inscription setup into a single silica chip. Coupling light at 543 nm into the optical waveguide resulted in yellow fluorescence in the microfluidic channel. [Crespi et al. \(2012\)](#) developed an optofluidic chip exploiting the 3D writing capabilities of ULI to measure protein concentrations using pairs of entangled photons. This allows to minimize light exposure of the specimen as the precision of quantum metrology is not any longer bound by the shot noise as for a classical interferometer. In such devices, the use of IO is inevitable to achieve high and stable quantum (and classical) interference contrast. The capability of inscribing microchannels of ULI may be used for mid-IR materials as well. This would allow optofluidic chips to operate in the valuable mid-IR region up to 10  $\mu\text{m}$ . Moreover, ULI can be applied to many more fields, such as processing quantum information ([Meany et al. 2015](#)) or space-division multiplexing for enhanced bandwidths in optical communication networks ([van Uden et al. 2014](#)); however, a full review would go beyond the scope of this thesis.

## Paper 1 (Tepper 2017a): Integrated optics prototype beam combiner for long baseline interferometry in the L and M bands

The first paper is concerned with the characterization of evanescent  $2\times 2$  coupler as shown in Fig. 3.4 top center. I was provided by Romina Diener, University of Jena, with one chip containing 20 couplers inscribed with different parameters, i.e. interaction length, waveguide separation and bend radius. The goal of this parameter scan was to find the right parameters for a coupler that shows a balanced 50/50 splitting ratio over the L band. After I had identified the most suitable L band coupler, I performed further tests on this device in order to assess its relevant properties for astronomical interferometry. Interestingly, the coupler also showed an almost 50/50 splitting over the M band, so that I extended the characterization to this band.

I report on spectrally resolved throughput and splitting ratio, modal behavior and polarization properties of the beam combiner. Most importantly, however, I demonstrate for the first time that high interferometric contrast can be achieved over a wide mid-IR spectral range using integrated optics and experimentally trace the differential dispersion contribution of an integrated optics combiner by measuring the phase distortion over the spectrum.

The results were published in the peer-reviewed journal *Astronomy & Astrophysics*.

# Integrated optics prototype beam combiner for long baseline interferometry in the $L$ and $M$ bands

J. Tepper<sup>1</sup>, L. Labadie<sup>1</sup>, R. Diener<sup>2</sup>, S. Minardi<sup>2,3</sup>, J.-U. Pott<sup>4</sup>, R. Thomson<sup>5</sup>, and S. Nolte<sup>2</sup>

<sup>1</sup> 1. Physikalisches Institut, Universität zu Köln, Zùlpicher Strasse 77, 50937 Köln, Germany  
 e-mail: tepper@ph1.uni-koeln.de

<sup>2</sup> Institut für Angewandte Physik, Friedrich-Schiller-Universität Jena, Albert-Einstein-Strasse 15, 07745 Jena, Germany

<sup>3</sup> Leibniz-Institut für Astrophysik Potsdam, An der Sternwarte 16, 14482 Potsdam, Germany

<sup>4</sup> Max Planck Institut für Astronomie, Königstuhl 17, 69117 Heidelberg, Germany

<sup>5</sup> Scottish Universities Physics Alliance (SUPA), Institute of Photonics and Quantum Sciences (IPaQS), Heriot Watt University, Riccarton Campus, Edinburgh, EH14 4AS, UK

Received 25 November 2016 / Accepted 11 March 2017

## ABSTRACT

**Context.** Optical long baseline interferometry is a unique way to study astronomical objects at milli-arcsecond resolutions not attainable with current single-dish telescopes. Yet, the significance of its scientific return strongly depends on a dense coverage of the uv-plane and a highly stable transfer function of the interferometric instrument. In the last few years, integrated optics (IO) beam combiners have facilitated the emergence of 4-telescope interferometers such as PIONIER or GRAVITY, boosting the imaging capabilities of the VLTI. However, the spectral range beyond 2.2  $\mu\text{m}$  is not ideally covered by the conventional silica based IO. Here, we consider new laser-written IO prototypes made of gallium lanthanum sulfide (GLS) glass, a material that permits access to the mid-infrared spectral regime.

**Aims.** Our goal is to conduct a full characterization of our mid-IR IO two-telescope coupler in order to measure the performance levels directly relevant for long-baseline interferometry. We focus in particular on the exploitation of the  $L$  and  $M$  astronomical bands. **Methods.** We use a dedicated Michelson-interferometer setup to perform Fourier transform spectroscopy on the coupler and measure its broadband interferometric performance. We also analyze the polarization properties of the coupler, the differential dispersion and phase degradation, as well as the modal behavior and the total throughput.

**Results.** We measure broadband interferometric contrasts of 94.9% and 92.1% for unpolarized light in the  $L$  and  $M$  bands. Spectrally integrated splitting ratios are close to 50%, but show chromatic dependence over the considered bandwidths. Additionally, the phase variation due to the combiner is measured and does not exceed 0.04 rad and 0.07 rad across the  $L$  and  $M$  band, respectively. The total throughput of the coupler including Fresnel and injection losses from free-space is 25.4%. Furthermore, differential birefringence is low ( $<0.2$  rad), in line with the high contrasts reported for unpolarized light.

**Conclusions.** The laser-written IO GLS prototype combiners prove to be a reliable technological solution with promising performance for mid-infrared long-baseline interferometry. In the next steps, we will consider more advanced optical functions, as well as a fibered input, and we will revise the optical design parameters in order to further enhance the total throughput and achromatic behavior.

**Key words.** instrumentation: high angular resolution – instrumentation: interferometers – techniques: interferometric

## 1. Introduction

Aperture synthesis imaging is a major ambition of the optical/IR interferometry community for the next decades and it will remain the only route to reach a level of angular resolution equivalent to that of a diffraction-limited telescope of a few hundred meters aperture. In aperture synthesis imaging, the high fidelity of the reconstructed images needed to observe objects with complex morphologies critically depends on our ability to deliver observations with a dense uv coverage (Soulez et al. 2016). Over the last five to ten years, a major incentive has been given to improving this technique at the VLTI and at the CHARA Array. Recently, Kluska et al. (2016) has exploited the four-telescope imaging capabilities of the PIONIER instrument (Le Bouquin et al. 2011) in the  $H$  band to evidence a time-variable asymmetry in the close environment of MWC158 whose origin has not yet been determined. Using

the same instrument, Hillen et al. (2016) have obtained a direct view of the dust sublimation front in the circumbinary disk of the post-AGB system IRAS 08544-4431. Using the improved uv coverage of the six-telescope MIRC beam combiner operating in the  $H$  band, Roettenbacher et al. (2016) were able to map the surface of zeta Andromeda with a 0.5 mas resolution and investigated the surface distribution of starspots to reveal the absence of a solar dynamo mechanism. These recent results highlight the unprecedented potential of optical/infrared interferometric imaging, which has now gone through significant improvement. The core subsystem of an infrared imaging interferometer is the beam combiner, where the beams of the individual sub apertures coherently interfere. While various designs for beam combination have been explored since the early times of long-baseline interferometry, instrumental solutions based on integrated optics (IO) are now considered serious reliable alternatives to bulk optics designs. Their “on-chip”

compact design results in a simpler optical subsystem in comparison to instruments like AMBER (Petrov et al. 2007) or MATISSE (Lopez et al. 2014). Moreover, thanks to the single-mode properties of the component, the IO beam combiner delivers a much more stable instrumental transfer function, which is key to the measurement of high accuracy interferometric visibilities. After about 15 yr of R&D activities, such concepts have become well-established solutions in the near-IR and are currently implemented in the community instruments GRAVITY (Eisenhauer et al. 2011) and PIONIER (Benisty et al. 2009), in the  $K$  and  $H$  bands, respectively. The recognized importance of the mid-infrared spectral range for the study of exoplanetary systems and AGNs at high angular resolution motivates the extension towards longer wavelengths of integrated optics solutions. Due to the intrinsic absorption beyond  $3\ \mu\text{m}$  of silica, a specific technological platform for the mid-infrared is needed. The three main technological platforms that have been explored for mid-infrared IO technologies are based on ion exchange/diffusion, chemical etching/lithography, and ultrafast laser writing. Ion diffusion in lithium niobate glass has demonstrated the feasibility of active IO beam combiners in the  $3.2\text{--}3.8\ \mu\text{m}$  range (Hsiao et al. 2009; Heidmann et al. 2012). However, broadband operation by Martin et al. (2014) has evidenced large chromatic dispersion and low-confinement of the modes, which resulted in propagation losses as high as 16 dB/cm. Etching and lithography techniques have been tested with chalcogenide glass, which raised interest due to its potentially wide mid-infrared transparency from  $1\ \mu\text{m}$  to  $20\ \mu\text{m}$ . Using this platform, simple rib channel waveguides have been manufactured showing average propagation losses of  $0.5\text{--}1\ \text{dB/cm}$  in the  $3\text{--}6\ \mu\text{m}$  range (Ma et al. 2013) and  $6\ \text{dB/cm}$  in the  $2\text{--}20\ \mu\text{m}$  range (Vigreux et al. 2015). Recently, Kenchington Goldsmith et al. (2016) used this platform to manufacture a multimode interference coupler (MMI) in chalcogenide glass for nulling interferometry.

To date, the technique of direct laser writing has been a successful approach for the manufacture of two-telescope and three-telescope mid-infrared IO beam combiners. Using fluorozirconate ZBLAN glass transparent from  $0.2\ \mu\text{m}$  to  $5\ \mu\text{m}$ , single-mode channel waveguides with  $0.3\ \text{dB/cm}$  losses and evanescent couplers over the spectral range of  $3.75\text{--}4.2\ \mu\text{m}$  were laser-inscribed by Gross et al. (2015). The laser inscription technique has also been used to manufacture proof-of-concept IO combiners in chalcogenide glass, with reported losses on the order of  $1\ \text{dB/cm}$  (Labadie et al. 2011; Ródenas et al. 2012; Arriola et al. 2014). In all the cases mentioned above, neither high interferometric contrasts nor a detailed investigation of the differential birefringence and dispersion were reported. These are essential quantities used to assess the potential of IO devices for long-baseline interferometry. In this paper, we report for the first time to our knowledge a complete performance characterization in the  $L$  ( $3.1\text{--}3.6\ \mu\text{m}$ ) and  $M$  bands ( $4.5\text{--}4.9\ \mu\text{m}$ ) of new  $2 \times 2$  directional couplers manufactured by laser inscription in a gallium lanthanum sulfide (GLS) chalcogenide glass. This experimental work tests in detail the potential of new IO combiners in the immediate perspective of astronomical applications. The paper is structured as follows. Section 2 presents the design adopted for the integrated optics component and briefly describes the ULI fabrication process. Section 3 describes the laboratory setup and the measurement procedure. Our results are detailed in Sect. 4 and deal with the spectral splitting ratio and modal behavior, the throughput characteristics, the polarization properties of the coupler, and the monochromatic and broadband interferometric performance revealing the impact of the beam combiner on the phase curvature across the  $L$  and  $M$  bands.

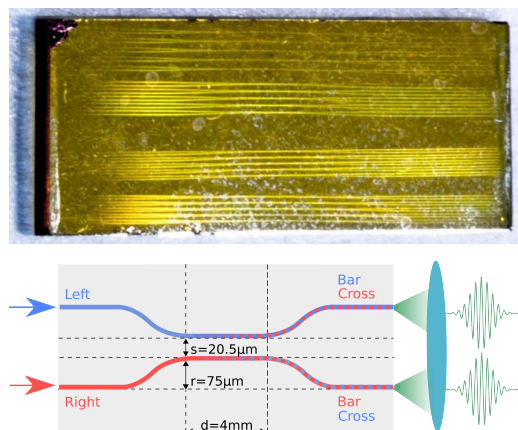


**Fig. 1.** *Top:* integrated optics chip including 20 two-beam combiners written with different parameters. *Bottom:* dimensions of the chosen two-beam combiner used in this paper and labeling of the waveguides. The terms bar and cross are used to distinguish the output of the initially excited waveguide from the evanescently coupled arm output.

## 2. Properties of the integrated optics combiner

### 2.1. Ultrafast laser writing for interferometry

The  $2 \times 2$  integrated optics couplers are manufactured using the technique of ultrafast laser inscription (ULI; Glezer et al. 1996; Davis et al. 1996; Nolte et al. 2003; Thomson et al. 2009) that exploits the large peak intensity (up to  $10^{12}\ \text{W/cm}^2$ ) of a focused femtosecond laser to induce a structural change in the glass sample. This can result in a localized refractive index modification confined in the region where the femtosecond laser is focused. Physically, intense light pulses can transfer a substantial fraction of their energy in transparent dielectric media by means of multiphoton ionization followed by avalanche ionization, which could trigger localized structural glass modifications from a chain of chemical and/or thermodynamic resettlements of the glass network. Depending on the chosen substrate material, either a local increase or decrease in the bulk refractive index can be observed. By translating the irradiated sample under the focused laser beam, it is possible to create a pattern of waveguides, with an index difference between the core and the cladding depending basically on the laser power and the duration of irradiation. Recently, this technique has attracted some attention in the field of astronomical instrumentation. Further detail on the technique is available from the review of Gross & Withford (2015).

### 2.2. Design and fabrication

The integrated optics chip presented in this paper (see Fig. 1 top) is composed of commercial gallium lanthanum sulfide (GLS), a chalcogenide glass with refractive index  $n = 2.3159 \pm 0.002$  at  $3.4\ \mu\text{m}$ <sup>1</sup> and high transparency from  $0.5$  to  $9\ \mu\text{m}$ , thus suitable for the astronomical  $L$  and  $M$  bands. In comparison to arsenic-based waveguides (Vigreux et al. 2007), GLS is a non-toxic material. The design of the device is a directional evanescent coupler (Fig. 1 bottom) as this represents a key building block for advanced functions such as ABCD phase and visibility estimators (Colavita 1999). In the interaction area where the channel waveguides have the smallest separation, a fraction of the light injected in one arm is transferred into the nearby arm

<sup>1</sup> Interpolated from refractive index measurements commissioned to VITRON GmbH, August 2016.

J. Tepper et al.: Integrated optics for  $L$  and  $M$  band interferometry

by evanescent coupling. A monochromatic splitting/coupling ratio of 50/50 can be obtained by optimizing the gap between the waveguides  $s$  and the interaction length  $d$  of the device.

The integrated optics chip was inscribed using the Jena laser writing facility composed of a femtosecond Yb:KGW laser at 1023 nm launching 400 fs pulses at 500 kHz repetition rate, comparable to parameters used in Arriola et al. (2014). The waveguides are written using the multipath technique where cores are built up by a collection of 21 tracks, each spaced laterally by 300 nm with respect to the previous one. Three design parameters were varied to estimate their effect on the performance of the device in the  $L$  band (cf. Fig. 1 bottom). Two values  $r$  for the S-bend amplitude, namely 50 and 75  $\mu\text{m}$ , were considered to investigate the impact on the bending losses. The tested coupling lengths were 0 mm and 4 mm. The separation  $s$  was varied between 20 and 22  $\mu\text{m}$  with 0.5  $\mu\text{m}$  steps as this parameter has a strong influence on the coupling as well. In total, twenty directional couplers were inscribed on the chip. The result is shown in Fig. 1 top where several of these couplers are visible on the chip with dimensions  $25 \times 10 \times 1$  (mm)<sup>3</sup>. Waveguides were written at a depth of 200  $\mu\text{m}$  from the top and bottom surface, respectively, and had measured cross sections of  $7 \times 25$  ( $\mu\text{m}$ )<sup>2</sup>. We note that the impact of this design on the  $M$ -band performance was not considered at first in the selection of the sample that was eventually characterized.

### 3. Laboratory setup

The characterization setup, similar to that used in Labadie et al. (2007), is based on a classical Michelson interferometer design (Fig. 2). Two sources of light enable both broadband and monochromatic measurements: a CoolRed blackbody source ( $T = 1500$  K) by Ocean Optics connected to a multimode infrared fiber from Thorlabs with 400  $\mu\text{m}$  core and a single-mode 5 mW HeNe laser at 3.39  $\mu\text{m}$ . The sources are spatially filtered by 20 and 25  $\mu\text{m}$  pinholes, respectively, before being collimated with an  $f = 50$  mm achromat and an  $f = 150$  mm plano-convex lens, respectively. A pellicle beamsplitter (BS2) is used instead of a conventional thick beamsplitter to avoid differential dispersion in the interferogram. A Thorlabs Z812B delay line is used to adjust remotely the optical path difference in one arm by translating one flat mirror M1. Both mirrors can be adjusted in tip-tilt, and two images of the source can be created to be coupled to each input of the device by an  $f = 50$  mm achromat. Using BS1, the laser beam can be independently aligned. The two interferometric outputs are re-imaged by an  $f = 50$  mm achromat and the 50 mm camera objective onto the focal plane of the 5360S Infratech Camera. The IO chip can be fine-positioned in all three directions thanks to a high-precision XYZ translation stage.

A Michelson interferometer can operate as a Fourier transform spectrometer, and we use this mode to measure the spectra of our device. A typical obstacle, however, is recording the true OPD as errors caused by the inaccurate and non-repeatable translation of the delay line directly translate into spectral errors in the Fourier space. We fix this problem by simultaneously recording the interferogram of the 3.39  $\mu\text{m}$  laser, see Fig. 3. The known fringe spacing is used to yield the true OPD and functions as a metrology channel (Tepper et al. 2016).

### 4. Results

We present here the characterization of the properties of the directional coupler which are relevant for applications in stellar

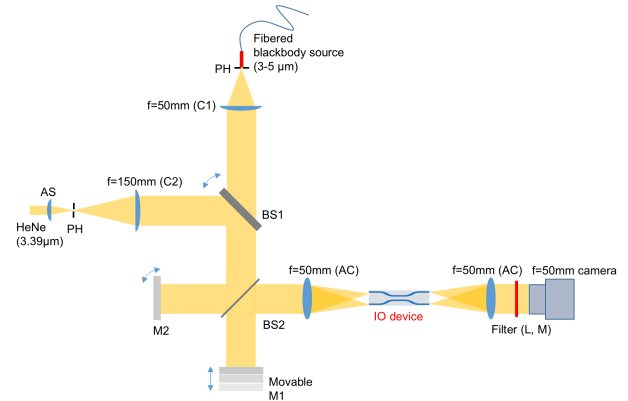


Fig. 2. Layout of the experimental setup. AS: aspheric lens; PH: pinhole; C1, C2: collimator 1 & 2; BS1: thick beamsplitter; BS2: pellicle beamsplitter; M1, M2: flat mirrors; AC:  $f = 50$  mm achromat; F:  $L$  or  $M$  broadband filter.

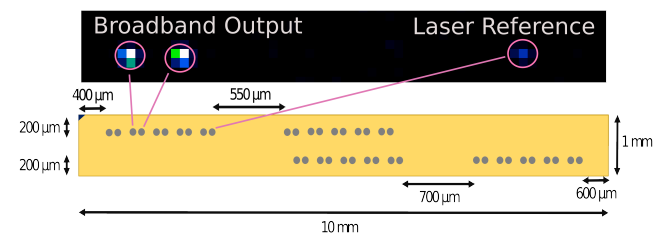
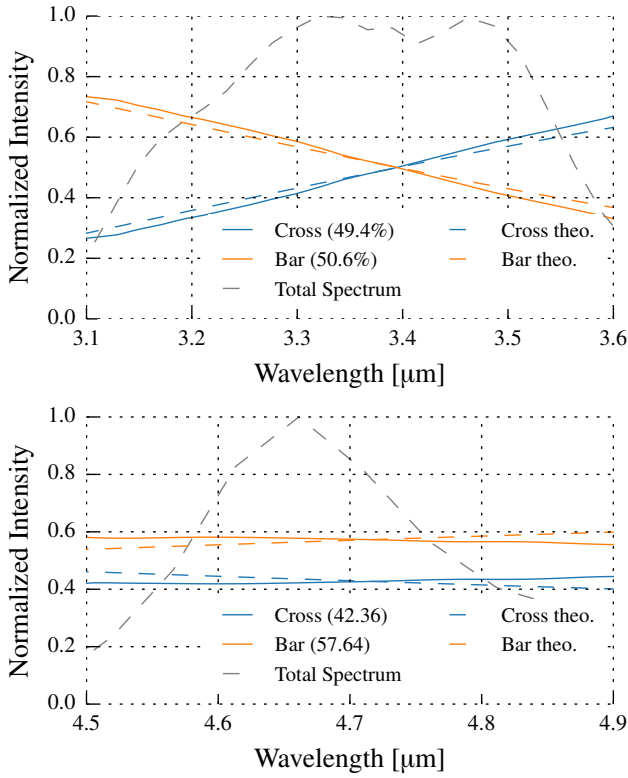


Fig. 3. Outputs of the chip imaged with a magnification of 1 and focused on mainly one pixel. Next to the broadband output, the laser interferogram is recorded in a neighboring coupler. Below, the corresponding couplers from the chip (face-on view) are specified, in total 20 couplers.

interferometry. We report on the spectral splitting ratio, modal behavior, throughput, polarization properties, broadband interferometric contrast and chromatic dispersion. The impact of a cryogenic temperature cooling cycle on the performance of the component is presented as well.

#### 4.1. Splitting ratio over $L$ and $M$ band

We were provided with 20 couplers written with different parameters in one single chip as seen in Fig. 1 top and 3. In order to find the most suitable coupler for  $L$ -band interferometry, we first investigated the broadband splitting ratio defined as  $P_{\text{cross}}/(P_{\text{cross}} + P_{\text{bar}})$ , where  $P$  is the power in the respective channel (Fig. 1 bottom). The splitting ratios, which depend on the interaction length and the separation of the waveguides in the interaction area, are found to range from 10 to 85% for the different couplers of the chip. The best coupler, i.e., closest to 50/50, shows a splitting ratio of 49.4%. The design properties of this particular coupler are  $d = 4$  mm and  $s = 20.5$   $\mu\text{m}$  (see Fig. 1 bottom). Using Fourier transform spectroscopy, we measured the chromaticity of the splitting ratio. By injecting the two input beams in the same input and varying the OPD, we yield one interferogram for each output from which the respective spectrum is derived (see Fig. 4 top). We find a linear trend of the splitting ratio ranging from about 30% at 3.1  $\mu\text{m}$  to 70% at 3.6  $\mu\text{m}$ . Also shown as a dashed line is the normalized spectrum of the totally transmitted flux (i.e. the sum of the two output fluxes), which is the product of the transmission curves of the respective broadband filter, of the optical bench and of the waveguide. The chromatic splitting ratio for the right input was also measured and



**Fig. 4.** Spectrally resolved coupling ratios for the left input over the  $L$  (top) and  $M$  (bottom) bands measured for the two outputs bar and cross. The numbers in the brackets refer to the spectrally integrated coupling. The dashed line shows the measured bandwidth of the experiment.

shows the same behavior. Using the same coupler in the astronomical  $M$  band, we found an imbalance in the broadband splitting ratio of 42.36%. The spectral dependence, however, is found to be flatter (see Fig. 4 bottom). This coupler is used for all further measurements, except for the spectral transmission (Fig. 6, channel waveguide instead) and the temperature test in Sect. 4.6. Theoretically, the splitting ratio for the directional coupler can be derived as described in Snyder & Love (1983). As the calculation is sensitive to the cross section of the waveguide, which is not known precisely, we used a simplified, weakly wavelength-dependent approach for the coupled power,  $\sin^2(K \cdot d/\lambda)$ ,  $K$  being a real scalar constant and  $d$  the interaction length. Only a discrete set of  $K$  values correspond to a 50/50 splitting at a given wavelength, which is here taken at  $3.4 \mu\text{m}$  and  $4.7 \mu\text{m}$ , respectively, for the  $L$  and  $M$  band. From these values, the correct  $K$  can be univocally determined by comparing the slope to the experimental data (Fig. 4). The  $K$  values ( $K_L = 2.0 \times 10^{-3}$  and  $K_M = 0.84 \times 10^{-3}$ ) indicate that we operate close to 0.75 and 0.25 beat length, respectively, at the above-mentioned reference wavelengths for the  $L$  and  $M$  band.

#### 4.2. Modal behavior

For the purpose of wavefront filtering (Ruilier & Cassaing 2001), it is essential that the waveguides exhibit single-mode behavior over the considered bandwidths. Figure 5 shows an image of one of the two outputs and the respective mode profile. We use an optical system with a working f-number of  $f/36$  to magnify and image the MFD onto our sensor with a pixel

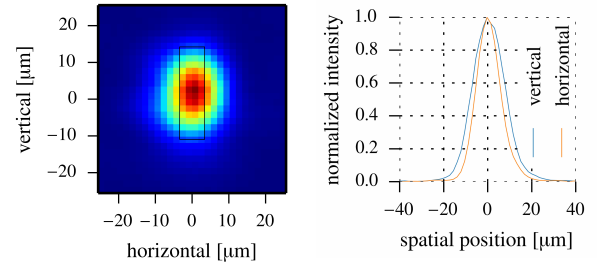


**Fig. 5.** Left: left output of the two-telescope combiner with a magnification of 17 at  $3.39 \mu\text{m}$ . The black rectangle illustrates the size of the waveguide cross section. Right: respective vertical and horizontal Gaussian-like mode profiles before deconvolution.

size of  $30 \mu\text{m}$ . We find a Gaussian-like shape as expected for single-mode waveguides, with  $1/e^2$  measured mode field diameters (MFD) of  $28.2 \pm 0.3 \mu\text{m}$  (vertically) and  $(22.6 \pm 0.2) \mu\text{m}$  (horizontally) at  $3.39 \mu\text{m}$ . The measured FWHM point spread function (PSF) of the optical system is  $8.4 \mu\text{m}$  ( $8.5 \mu\text{m}$  theoretically). We derive the true MFD as the diameter of the Gaussian waveguide mode, whose convolution (i.e., the convolution of the Gaussian mode) with the PSF results in the measured MFD. We obtain  $16.3 \mu\text{m}$  and  $24.8 \mu\text{m}$  for the horizontal and vertical direction, respectively. This can be related to the waveguide cross section to obtain the refractive index contrast. As an approximation, we used a rectangular waveguide model with a step-index<sup>2</sup>. Indeed, the cross section is only known with an accuracy of  $\pm 2 \mu\text{m}$ , and the true index profile is unknown. Therefore, we can only give a range for the refractive index contrast from  $3 \times 10^{-3}$  to  $4 \times 10^{-3}$ . Single-mode behavior is classically tested against the presence of a second higher order mode by changing the input coupling conditions, such as inserting a small lateral displacement of the injection spot (Hô et al. 2006). We applied such a displacement in the vertical and horizontal direction and we did not find any deviation from the near-Gaussian shape.

#### 4.3. Throughput

In this section, we present the total and spectrally resolved relative throughputs of the coupler.

The total throughput in the  $L$  band is estimated by injecting into one of the two inputs, and measuring the sum of the flux from the two outputs. Dividing this number by the input beam flux (measured by removing the sample in front of the imaging system), we obtain the throughput of the component.

For the throughput experiment we used input beam diameters of 8, 11, 14, and 16 mm in order to find the optimal input coupling efficiency. Table 1 shows the throughputs for the different injection beam diameters. We find the optimal throughput of 25.4% at 11 mm. This corresponds to a numerical aperture of 0.11 and a  $\Delta n = (3.1 \pm 0.1) \times 10^{-3}$ , which is in line with the change in refractive index derived in the previous section.

The total throughput can be written as  $T = (1 - R_F)^2 \cdot C \cdot PL \cdot B^2$ , where  $C$  is the input coupling efficiency and  $R_F$  the Fresnel reflections at the input and output facets. The values of  $P$  and  $B$  account for the reduced transmission due to propagation losses per cm and bending losses per bend, respectively. The quantity  $L = 2.5 \text{ cm}$  is the length of the component. For the coupling efficiency we assume the optimal coupling between a Gaussian and an Airy pattern given by  $C = 81\%$  (Toyoshima 2006). Due to the

<sup>2</sup> Calculated using the online tool

<http://www.computational-photonics.eu/eims.html>

J. Tepper et al.: Integrated optics for  $L$  and  $M$  band interferometry

**Table 1.** Throughput of the 25 mm two-telescope combiner in  $L$  band for different input beam diameters.

Beam diameter	8 mm	11 mm	14 mm	16 mm
Left input	20.4%	22.5%	16.6%	13.8%
Right input	24.5%	28.4%	24.1%	21.9%
Average	22.4%	25.4%	20.4%	17.8%

**Notes.** Absolute accuracy on the order of 2% due to error propagation of imperfect adjusting of the iris.

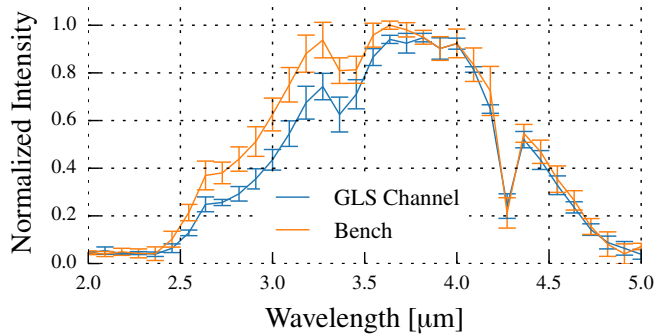


**Fig. 6.** Normalized transmission of the optical bench and transmission of the optical bench including a GLS channel waveguide. The GLS data is upscaled without exceeding the bench data. For each case, three datasets were taken and the error bars show the standard deviation.

high refractive index  $n = 2.316$ , a Fresnel reflection coefficient of  $R_F = 15.7\%$  per facet is found. This can be mitigated by an AR coating, which would raise the throughput to 36%. Bending losses were separately measured to  $(0.6 \pm 0.2)$  dB/bend. Using these numbers and taking the averaged throughput for the 11 mm beam diameter, we estimate  $P$  to be  $0.94$  dB/cm  $\pm$   $0.29$  dB/cm. We stress that this number is a rough approximation, due to the large error bar on the bending losses, and is also very sensitive to the input coupling efficiency. For instance, for a coupling efficiency of 70%, the value  $P = 0.69$  dB/cm would be derived from our measurements.

The transmission spectrum of the component was measured by Fourier transform spectroscopy. The two beams are injected into the same channel waveguide and by scanning the OPD, an interferogram is recorded from which the relative spectrum is derived. This is directly compared to the normalized transmission of the bench (see Fig. 6 for details). We find a very good match between the two spectra, which indicates a flat spectral response of the waveguide. The location of the CO<sub>2</sub> dip at  $\approx 4.26$   $\mu$ m is measured at the expected position in both transmission spectra and confirms the validity of the OPD correction method.

#### 4.4. Polarization properties

Instrumental contrasts measured with a long-baseline interferometer are highly sensitive to polarization mismatches resulting from differential stress and birefringence between the two arms (Berger et al. 1999). When operating with unpolarized stellar light, it is important that the differential birefringence is minimized so that the polarization alteration that may arise from the IO component is similar in each arm, hence reducing the visibility loss effects. We investigate the polarization properties of the coupler at 3.39  $\mu$ m. We look at one output and test the difference in polarization for the two arms by exciting the left and the right input one at a time. By placing a half-wave plate before the

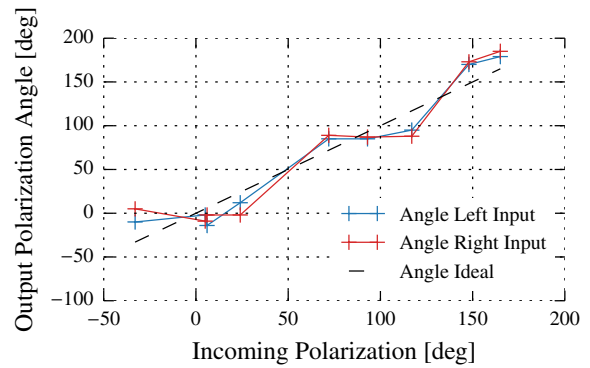


**Fig. 7.** Polarization angle of the output ellipse (cf. Fig. 8) for the left output when injecting into the left and right input, respectively. For the input, we used the linearly polarized HeNe laser at 3.39  $\mu$ m at different polarization angles (depicted on the x-axis). The dashed line depicts an unaltered polarization angle. Qualitatively, there is very little or no difference between the two output polarization angles.

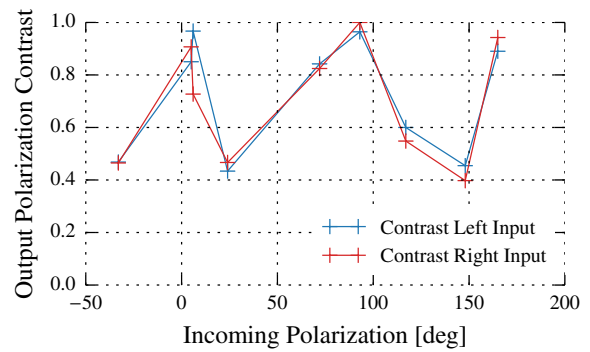


**Fig. 8.** Change in polarization contrast (“ellipticity”) for the left output when injecting into the left and right input, respectively, for incoming linear polarization of different angles. As for the angle of the ellipse (cf. Fig. 7), there is very little or no difference in the ellipticity between the two outputs.

component and an analyzer behind the output collimation lens, we analyze the change in polarization state for different incoming polarization angles. Two different quantities are measured: the change in polarization angle and to what extent linear polarization is transformed into elliptical polarization. The latter is quantified as the polarization contrast  $P_c = \frac{I_{\max} - I_{\min}}{I_{\max} + I_{\min}}$ , where  $I_{\max}$  and  $I_{\min}$  are the maximum and minimum intensities, respectively, found by turning the polarizer. Consequently,  $P_c = 1$  for a linear polarization and  $P_c = 0$  for a circular polarization.

From Fig. 7, we find that the polarization angle is similarly well maintained for both inputs to within  $20^\circ$ . Furthermore, for input angles close to 0, 90, and  $180^\circ$ , the polarization state is almost unchanged and remains linear, as seen in Fig. 8. For other angles, the linear polarization is transformed into an elliptical polarization with the contrast dropping down to 0.4. The same result is found by measuring the right output. The important result from Figs. 7 and 8 is that, for a given output, the change in polarization is almost identical for both arms, making differential polarization effects small. The polarization properties of the coupler can be explained by the rectangular waveguide cross section, which induces shape birefringence (Marcuse 1974).

#### 4.5. Interferometric contrast and differential dispersion

In the following sections interferograms over different bandwidths using the evanescent  $2 \times 2$  coupler are presented. The

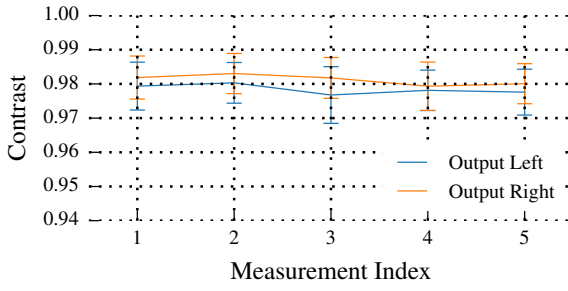


**Fig. 9.** Monochromatic interferometric contrast of the two outputs at  $3.39 \mu\text{m}$  for a series of measurements. The error bars show the standard deviation in contrast for the respective measurement.

interferograms are recorded for linearly polarized laser light and unpolarized broadband light. The recording and post-processing is as follows. First, the photometric channels are recorded. Then, the interferogram is recorded. The laser signal is recorded simultaneously to yield the true OPD as described in Sect.

#### 4.5.1. Monochromatic interferogram at $3.39 \mu\text{m}$

First, using the vertically linearly polarized HeNe laser at  $3.39 \mu\text{m}$ , a monochromatic interferogram is recorded. Each interferogram is scanned over approximately 125 fringes. From the pairs of local maximums and minimums, 125 contrast values can be calculated. The average contrast and its standard deviation are shown in Fig. 9. This measurement was repeated five times and averaged contrasts of  $97.8 \pm 0.6\%$  and  $98.1 \pm 0.6\%$  for the two outputs are found (sampling effects are negligible). Repeated testing showed that the measured contrast does not change for an incoming polarization angle of  $45^\circ$ . This is in line with Figs. 7 and 8, which show that differential birefringence between the two arms is small for any incoming angle. In comparison, for an interferogram recorded through a single-channel waveguide, where no differential birefringence is present, we find  $99.4\%$  with a standard deviation of  $0.2\%$ . This loss in contrast of  $\sim 1.4\%$  would correspond to a mismatch in polarization angle of  $0.2 \text{ rad}$ .

#### 4.5.2. L band interferogram

The L band filter, covering the range from  $3.1$  to  $3.6 \mu\text{m}$ , as seen in Fig. 4 top, is inserted into the collimated beam. Figure 10 shows the two recorded interferometric outputs. We find a high contrast of  $94.9\%$ . In addition to the high broadband contrasts, the  $\pi$ -phase shift between the two outputs resulting from energy conservation is observed with excellent repeatability over the coherence length.

In order to estimate the level of differential dispersion, we calculated the phase of the interferogram through the real and imaginary part of its Fourier transform. After removing the linear part in wavenumber  $2\pi x_0 \sigma = 2\pi x_0 / \lambda$ , which relates to the zero-OPD position  $x_0$  (Coudé du Foresto et al. 1995), the non-linear term remains, which accounts for the overall differential dispersion. In order to disentangle any dispersion that may arise from the experimental setup, we also measured the phase for an interferogram without the IO chip. The results are shown in Fig. 11. We find that the phase variation across the band is mainly determined by the phase from the testbench itself and that the combiner is close to dispersion free with a standard deviation of

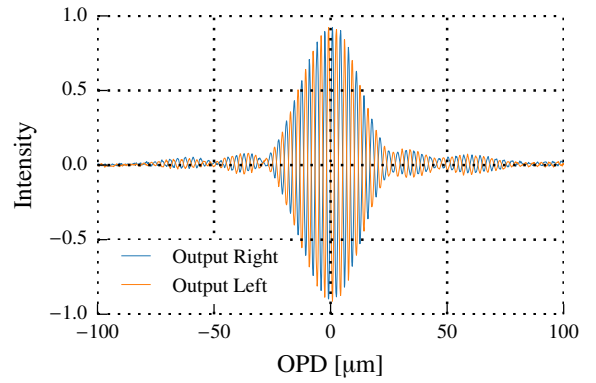


**Fig. 10.** Experimental L-band interferogram of the two interferometric outputs of the coupler after photometric correction. A broadband contrast of  $94.9\%$  is measured. The spectral shape of the bandwidth is shown in Fig. 11. The respective interferograms of the two outputs are shifted by half a wavelength, i.e.,  $\pi$ -phase shifted.

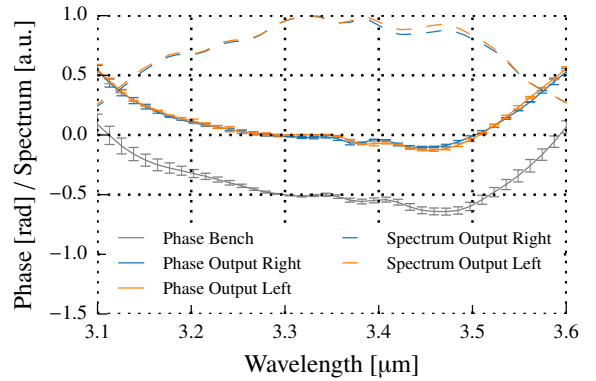


**Fig. 11.** Phases for the two chip outputs as well as the phase of experimental setup without chip (lowered by  $0.5 \text{ rad}$  for visualization) over the L band. The value  $\pi$  was subtracted from one of the chip outputs to demonstrate the phase shift. The respective spectra are shown as dashed lines.

$0.04 \text{ rad}$  across the band. For visualization purposes  $\pi$  was subtracted from one of the two chip outputs. The excellent overlap of the two phase curves reflects the clean  $\pi$ -phase shift visible in the interferogram. The present dispersion can be further quantified through the dispersion parameter defined as  $D := \frac{d(\tau_g)}{d\lambda}$ , i.e., the derivative of the group delay with respect to wavelength. From Coudé du Foresto et al. (1995), the (differential) dispersion parameter can be related to the phase curvature, i.e., the second derivative of the phase with respect to the wavenumber, through

$$\frac{d^2\Phi}{d\sigma^2} = -2\pi c \lambda^2 \cdot (L\Delta D + D\Delta L). \quad (1)$$

Assuming that the two channels have identical lengths  $\Delta L = 0$ , the quantity of interest is the difference in dispersion parameters of the two channels multiplied by the length of the component  $L \cdot \Delta D = L \cdot (D_2 - D_1)$ . Before calculating the dispersion parameter, we subtracted the phase of the bench from the phase of the beam combiner interferogram. Then, calculating the second derivative of the phase averaged over the bandwidth, we find  $L\Delta D = 3.6 \times 10^{-5} \text{ ps/nm}$ . In comparison,

J. Tepper et al.: Integrated optics for  $L$  and  $M$  band interferometry

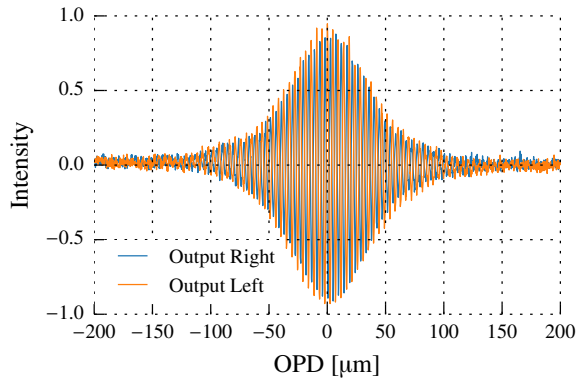


**Fig. 12.** Experimental  $M$ -band interferogram of the two interferometric outputs of the coupler after photometric correction. A broadband contrast of 92.1% is measured. The spectral shape of the bandwidth is shown in Fig. 13. The respective interferograms are not perfectly  $\pi$ -phase shifted, as can be seen from Fig. 13.

Coudé du Foresto et al. (1995) finds  $1.8 \times 10^{-4}$  ps/nm for a moderately dispersed interferogram. For our case, we then find a differential dispersion parameter of  $\Delta D = 1.4$  ps/(km nm) with a standard deviation of 15.7 ps/(km nm) across the band. Both values must be read as an upper limit as the phase variation due to the combiner is within the error bars (see Fig. 11).

#### 4.5.3. $M$ band interferogram

We measure the  $M$ -band interferogram through the same component and find a contrast of 92.1% (see Fig. 12). By applying the same procedures as for the  $L$ -band interferogram, we obtain the phase and the differential dispersion parameter. Here we find a relatively flat phase both for the bench and for the bench including the combiner (see Fig. 13). After subtracting the bench phase, we are left with a standard deviation of 0.07 rad across the band. The differential dispersion parameter of the combiner  $\Delta D = 2.8$  ps/(km nm) is about twice as large as for the  $L$  band with a standard deviation of 17.9 ps/(km nm) across the band. This may be due to the larger deviations towards the edge of the spectrum which result from the lower flux in the  $M$  band, as can be seen from the increasing error bars. After removal of  $\pi$  between the two outputs of the chip, we still find an offset of about 0.4 rad between the two phases. This shows that the phase shift slightly deviates from  $\pi$ , although this cannot be easily seen in Fig. 12.

#### 4.6. Temperature test

Another similar spare coupler was cooled down to 120 K in a cryostat over an approximately ten hours. After bringing the sample back to room temperature, no physical changes, e.g. cracks in the glass, were observed. The coupler was interferometrically characterized in the  $L$  band before and after the cooling down. In this one-time test, no major difference in throughput or interferometric properties was found. Thermal shocks, however, caused by dropping the sample directly into liquid nitrogen at 77 K, lead to cracks in one of two instances. As cryogenic conditions are typically used for mid-IR instruments, further testing is required to understand the optimal cooling rate  $\Delta T/\Delta t$  for our component.

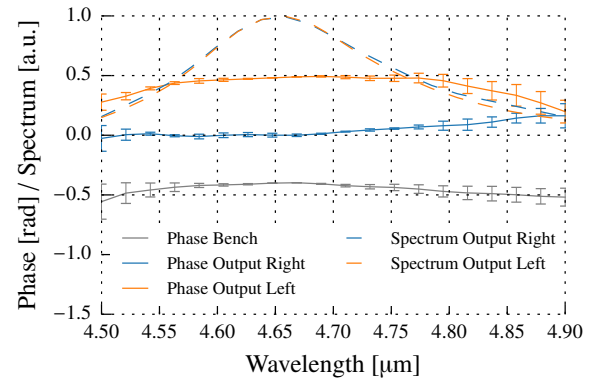


**Fig. 13.** Phases for the two chip outputs and the phase of experimental setup without chip (lowered by 0.5 rad for visualization). After subtraction of  $\pi$  a residual phase difference of 0.4 rad between the two outputs remains. The respective spectra are shown as dashed lines.

**Table 2.** Overview of the coupler properties.

	3.39 $\mu\text{m}$	$L$ band	$M$ band
integrated splitting	–	49.4%	42.3%
spectral splitting variation	–	35.5%	5.1%
throughput	–	25.4%	–
diff. polarization	0.2 rad		
	& see Sect. 4.4		
phase variation	–	0.04 rad	0.07 rad
contrast	98.0%	94.9%	92.1%

**Notes.** Numbers are averaged over the two inputs for the splitting and averaged over the two outputs for the phase and contrast.

## 5. Discussion and conclusion

We have presented a full characterization of a laser-written  $2 \times 2$  integrated-optics beam combiner in the 3–5  $\mu\text{m}$  mid-infrared range. The measured properties are summarized in Table 2. From twenty different test couplers, we chose to characterize the component with a spectrally integrated splitting ratio close to 50/50 over the  $L$  band. The measured splitting ratio shows a maximum imbalance of 30/70 across a relatively large bandwidth of  $\Delta\lambda = 0.5 \mu\text{m}$  with the balanced splitting being at 3.4  $\mu\text{m}$ . The chromatic dependence is larger than has been measured for the GRAVITY beam combiner (Benisty et al. 2009). However, the latter was measured over a narrower bandwidth  $\Delta\lambda/\lambda = 0.12 \mu\text{m}/1.6 \mu\text{m} = 0.08$ , whereas our result covers a broader bandwidth with  $\Delta\lambda/\lambda = 0.5 \mu\text{m}/3.4 \mu\text{m} = 0.15$ . Also, GRAVITY used  $2 \times 2$  asymmetric tapered couplers which allowed for an achromatic design. As we operate at a beat length of 0.75 in the  $L$  band, one immediate step towards a more achromatic design will be to test shorter interaction lengths to come closer to an achromatic coupler. In the  $M$  band, the maximum imbalance is found to be 40/60 over a bandwidth of  $\Delta\lambda = 0.4 \mu\text{m}$ . These are encouraging results given that a directional coupler is by definition a chromatic device. Further flatness of the spectral splitting ratio can be obtained with asymmetric coupler design (Takagi et al. 1992) or other broadband design, as in Hsiao et al. (2010). We find that the coupler exhibits some birefringence which supports non-degenerate quasi-TM and quasi-TE polarization modes. However, because of the

small differential polarization effect, the measured interferometric contrast in broadband unpolarized light remains high. Contrasts were measured of 98% at  $3.39\ \mu\text{m}$  as well as 94.9% over the  $L$  band and 92.1% over the  $M$  band.

Finally, we quantitatively assessed the dispersion parameter. Considering the length of the component, the estimated dispersion parameters  $D$  of 1.4 and 2.8 ps/(km nm), respectively, have little impact on the broadband interferograms. The deviation from 100% in contrast in  $L$  band can be roughly attributed to several effects: about 2% due to the chromatic splitting, about 1.4% due to differential birefringence and the rest possibly due to the dispersion of the experimental setup. In the  $M$  band this assignment is more difficult as the signal-to-noise ratio is much lower in that case. Our single-mode coupler shows a total throughput of 25.4%, including Fresnel, coupling, bend and propagation losses. Since a meaningful requirement for astronomical applications is the total throughput (after mitigation of the Fresnel losses), a potential objective is to revise the design of the device for a better trade-off between the propagation losses (higher for a longer component) and the bending losses (higher for a shorter component). Given that propagation losses can be as low as 0.3 dB/cm in similarly laser-written channel waveguides (Thomson 2016, priv. comm.), we are optimistic that by further optimization of the writing parameters, the total throughput can be significantly increased. We found a refractive index modification of about  $\Delta n = 3 \times 10^{-3}$ , which is about five times greater than the negative laser writing in ZBLAN reported in Gross et al. (2015). A large  $\Delta n$  is crucial in reducing bending losses and essential in order to implement more complex optical designs without greatly increasing the overall losses. In the view of a multi-aperture (4+) beam combiner, more advanced optical functions are targeted in the next phases of our technology roadmap. Also, the development of a fiber-fed system and the interface between the infrared fibers and the chip will be addressed.

*Acknowledgements.* L.L., R.D., S.M., J.-U.P., R.T., and J.T. acknowledge the financial support from the German Ministry of Education and Research (BMBF). Special thanks go to Michael Wiest who helped carrying out the cryogenic measurements. The authors thank the anonymous referee for the constructive remarks which helped to improve the quality of the paper.

## References

- Arriola, A., Mukherjee, S., Choudhury, D., Labadie, L., & Thomson, R. R. 2014, *Opt. Lett.*, **39**, 4820
- Benisty, M., Berger, J.-P., Jocoü, L., et al. 2009, *A&A*, **498**, 601
- Berger, J.-P., Rousselet-Perraut, K., Kern, P., et al. 1999, *A&A*, **139**, 173
- Colavita, M. M. 1999, *PASP*, **111**, 111
- Coué du Foresto, V., Perrin, G., & Boccas, M. 1995, *A&A*, **293**, 278
- Davis, K. M., Miura, K., Sugimoto, N., & Hirao, K. 1996, *Opt. Lett.*, **21**, 1729
- Eisenhauer, F., Perrin, G., Brandner, W., et al. 2011, *The Messenger*, **143**, 16
- Glezer, E. N., Milosavljevic, M., Huang, L., et al. 1996, *Opt. Lett.*, **21**, 2023
- Gross, S., & Withford, M. J. 2015, *Nanophotonics*, **4**, 20
- Gross, S., Jovanovic, N., Sharp, A., et al. 2015, *Opt. Express*, **23**, 7946
- Heidmann, S., Courjal, N., & Martin, G. 2012, *Opt. Lett.*, **37**, 3318
- Hillen, M., Kluska, J., Le Bouquin, J.-B., et al. 2016, *A&A*, **588**, L1
- Hô, N., Phillips, M. C., Qiao, H., et al. 2006, *Opt. Lett.*, **31**, 1860
- Hsiao, H.-K., Winick, K. A., Monnier, J. D., & Berger, J.-P. 2009, *Opt. Express*, **17**, 18489
- Hsiao, H.-K., Winick, K. A., & Monnier, J. D. 2010, *Appl. Opt.*, **49**, 6675
- Kenchington Goldsmith, H.-D., Cvetojevic, N., Ireland, M., et al. 2016, in *SPIE Conf. Ser.*, **9907**, 990730
- Kluska, J., Benisty, M., Soulez, F., et al. 2016, *A&A*, **591**, A82
- Labadie, L., Le Coarer, E., Maurand, R., et al. 2007, *A&A*, **471**, 355
- Labadie, L., Martin, G., Anheier, N. C., et al. 2011, *A&A*, **531**, A48
- Le Bouquin, J.-B., Berger, J.-P., Lazareff, B., et al. 2011, *A&A*, **535**, A67
- Lopez, B., Lagarde, S., Jaffe, W., et al. 2014, *The Messenger*, **157**, 5
- Ma, P., Choi, D.-Y., Yu, Y., et al. 2013, *Opt. Express*, **21**, 29927
- Marcuse, D. 1974, *Theory of dielectric optical waveguides* (New York: Academic Press)
- Martin, G., Heidmann, S., Rauch, J.-Y., Jocoü, L., & Courjal, N. 2014, *Opt. Eng.*, **53**, 034101
- Nolte, S., Will, M., Burghoff, J., & Tuennermann, A. 2003, *Appl. Phys. A: Mat. Sci. Proc.*, **77**, 109
- Petrov, R. G., Malbet, F., Weigelt, G., et al. 2007, *A&A*, **464**, 1
- Ródenas, A., Martin, G., Arezki, B., et al. 2012, *Opt. Lett.*, **37**, 392
- Roettenbacher, R. M., Monnier, J. D., Korhonen, H., et al. 2016, *Nature*, **533**, 217
- Ruilier, C., & Cassaing, F. 2001, *J. Opt. Soc. Am. A*, **18**, 143
- Snyder, A., & Love, J. 1983, *Optical Waveguide Theory*, Science paperbacks (Springer US), 391
- Soulez, F., Thiebaut, E., Kluska, J., et al. 2016, in *SPIE Conf. Ser.*, **9907**, 99070Z
- Takagi, A., Jinguji, K., & Kawachi, M. 1992, *J. Lightwave Technol.*, **10**, 735
- Tepper, J., Diener, R., Labadie, L., et al. 2016, *Proc. SPIE*, **9907**, 990719
- Thomson, R. R., Kar, A. K., & Allington-Smith, J. 2009, *Opt. Express*, **17**, 1963
- Toyoshima, M. 2006, *J. Opt. Soc. Am. A*, **23**, 2246
- Vigreux, C., Bonhomme, E., Pradel, A., et al. 2007, *Appl. Phys. Lett.*, **90**, 011110
- Vigreux, C., Escalier, R., Pradel, A., et al. 2015, *Opt. Mater.*, **49**, 218



## Paper 2 (Tepper 2017b): Ultrafast laser inscription in ZBLAN integrated optics chips for mid-IR beam combination in astronomical interferometry

In the second paper, I had the chance to collaborate with colleagues from Macquarie University, Sydney. [Gross et al. \(2015\)](#) had reported on the manufacturing of 2×2 couplers in ZBLAN by means of negative laser writing, i.e. writing the cladding into the ZBLAN substrate. Since there was no interferometric characterization performed, we decided to have the sample shipped to Cologne to use our interferometric testbench for further characterization.

After having tested the relevant properties of the sample (transmission, splitting ratio, interferometric contrast), I put the focus on the comparison between the ZBLAN and the GLS platform in this paper. This is a critical assessment as the most suitable platform for mid-IR ULI needs to be eventually identified in order to proceed to a science-qualified instrument.

The results were published in the peer-review journal *Optics Express*.



## Ultrafast laser inscription in ZBLAN integrated optics chips for mid-IR beam combination in astronomical interferometry

JAN TEPPER,<sup>1,\*</sup> LUCAS LABADIE,<sup>1</sup> SIMON GROSS,<sup>2</sup> ALEXANDER ARRIOLA,<sup>2</sup> STEFANO MINARDI,<sup>3,4</sup> ROMINA DIENER,<sup>2</sup> AND MICHAEL J. WITFORD<sup>2</sup>

<sup>1</sup>Universität zu Köln, Zùlpicher Straße 77, 50937 Köln, Germany

<sup>2</sup>Centre for Ultrahigh Bandwidth Devices for Optical Systems (CUDOS), MQ Photonics Research Centre, Department of Physics & Astronomy, Macquarie University, New South Wales 2109, Australia

<sup>3</sup>Leibniz-Institut für Astrophysik Potsdam, An der Sternwarte 16, 14482 Potsdam, Germany

<sup>4</sup>Institut für Angewandte Physik, Friedrich-Schiller-Universität Jena, Albert-Einstein-Strasse 15, 07745 Jena, Germany

\*tepper@ph1.uni-koeln.de

**Abstract:** Astronomical interferometry is a unique technique that allows observation with angular resolutions on the milliarcsec scale by combining the light of several apertures hundreds of meters apart. The PIONIER and GRAVITY instruments at the Very Large Telescope Interferometer have demonstrated that silica-based integrated optics (IO) provide a small-scale and highly stable solution for the interferometric beam combination process. Yet, important science cases such as exoplanet hunting or the spectroscopic characterization of exoplanetary atmospheres are favorable for observation in the mid-IR, namely the atmospheric windows L and L' band (3-4  $\mu\text{m}$ ), a wavelength range that is not covered by conventional silica-based IO. Here, we propose laser-inscribed IO  $2 \times 2$  couplers in ZBLAN and experimentally assess the critical properties of the component for broadband mid-IR interferometry. We measure the splitting ratio over the 2.5 to 5.0  $\mu\text{m}$  range and find excellent broadband contrast over the L (3.1-3.6  $\mu\text{m}$ ) and L' (3.6 - 4.0  $\mu\text{m}$ ) bands. Furthermore, we quantify the dispersion properties of the coupler and find a phase variation as low as 0.02 rad across the L and L' band, respectively. By optimizing the NA of our injection beam, we measured a very high total throughput of 58% over the L band including Fresnel reflection and coupling losses. We also compare our findings to recent advances in mid-IR IO in GLS and discuss its advantages and disadvantages for the implementation in future mid-IR interferometers.

© 2017 Optical Society of America

**OCIS codes:** (130.3120) Integrated optics devices; (160.3130) Integrated optics materials; (160.2750) Glass and other amorphous materials; (220.4000) Microstructure fabrication; (230.7370) Waveguides; (120.2650) Fringe analysis; (120.3180) Interferometry; (120.5050) Phase measurement.

### References and links

1. S. Wolf, F. Malbet, R. Alexander, J.-P. Berger, M. Creech-Eakman, G. Duchêne, A. Dutrey, C. Mordasini, E. Pantin, F. Pont, J.-U. Pott, E. Tatulli, and L. Testi, "Circumstellar disks and planets. Science cases for next-generation optical/infrared long-baseline interferometers," *A&A Rev.* **20**, 52 (2012).
2. A. Matter, L. Labadie, J. C. Augereau, J. Kluska, A. Crida, A. Carmona, J. F. Gonzalez, W. F. Thi, J.-B. Le Bouquin, J. Olofsson, and B. Lopez, "Inner disk clearing around the Herbig Ae star HD 139614: Evidence for a planet-induced gap?" *A&A* **586**, A11 (2016).
3. R. J. De Rosa, J. Rameau, J. Patience, J. R. Graham, R. Doyon, D. Lafrenière, B. Macintosh, L. Pueyo, A. Rajan, J. J. Wang, K. Ward-Duong, L.-W. Hung, J. Maire, E. L. Nielsen, S. M. Ammons, J. Bulger, A. Cardwell, J. K. Chilcote, R. L. Galvez, B. L. Gerard, S. Goodsell, M. Hartung, P. Hibon, P. Ingraham, M. Johnson-Groh, P. Kalas, Q. M. Konopacky, F. Marchis, C. Marois, S. Metchev, K. M. Morzinski, R. Oppenheimer, M. D. Perrin, F. T. Rantakyö, D. Savransky, and S. Thomas, "Spectroscopic Characterization of HD 95086 b with the Gemini Planet Imager," *Astrophys. J.* **824**, 121 (2016).
4. M. Bonnefoy, A. Zurlo, J. L. Baudino, P. Lucas, D. Mesa, A.-L. Maire, A. Vigan, R. Galicher, D. Homeier, F. Marocco, R. Gratton, G. Chauvin, F. Allard, S. Desidera, M. Kasper, C. Moutou, A.-M. Lagrange, J. Antichi, A. Baruffolo, J. Baudrand, J.-L. Beuzit, A. Boccaletti, F. Cantalloube, M. Carillet, J. Charton, R. U. Claudi, A. Costille, K. Dohlen,

- C. Dominik, D. Fantinel, P. Feautrier, M. Feldt, T. Fusco, P. Gigan, J. H. Girard, L. Gluck, C. Gry, T. Henning, M. Janson, M. Langlois, F. Madec, Y. Magnard, D. Maurel, D. Mawet, M. R. Meyer, J. Milli, O. Moeller-Nilsson, D. Mouillet, A. Pavlov, D. Perret, P. Pujet, S. P. Quanz, S. Rochat, G. Rousset, A. Roux, B. Salasnich, G. Salter, J.-F. Sauvage, H. M. Schmid, A. Sevin, C. Soenke, E. Stadler, M. Turatto, S. Udry, F. Vakili, Z. Wahhaj, and F. Wildi, "First light of the VLT planet finder SPHERE. IV. Physical and chemical properties of the planets around HR8799," *A&A* **587**, A58 (2016).
5. A. Chiavassa, R. Norris, M. Montargès, R. Ligi, L. Fossati, L. Bigot, F. Baron, P. Kervella, J. D. Monnier, D. Mourard, N. Nardetto, G. Perrin, G. H. Schaefer, T. A. ten Brummelaar, Z. Magic, R. Collet, and M. Asplund, "Asymmetries on red giant branch surfaces from CHARA/MIRC optical interferometry," *A&A* **600**, L2 (2017).
  6. R. M. Roettenbacher, J. D. Monnier, H. Korhonen, A. N. Aarnio, F. Baron, X. Che, R. O. Harmon, Z. Kóvári, S. Kraus, G. H. Schaefer, G. Torres, M. Zhao, T. A. Ten Brummelaar, J. Sturmann, and L. Sturmann, "No Sun-like dynamo on the active star  $\zeta$  Andromedae from starspot asymmetry," *Nature* **533**, 217–220 (2016).
  7. K. R. W. Tristram, D. Raban, K. Meisenheimer, W. Jaffe, H. Röttgering, L. Burtscher, W. D. Cotton, U. Graser, T. Henning, C. Leinert, B. Lopez, S. Morel, G. Perrin, and M. Wittkowski, "Parsec-scale dust distributions in Seyfert galaxies. Results of the MIDI AGN snapshot survey," *A&A* **502**, 67–84 (2009).
  8. L. Burtscher, S. Hönig, W. Jaffe, M. Kishimoto, N. Lopez-Gonzaga, K. Meisenheimer, and K. R. W. Tristram, "Infrared interferometry and AGNs: Parsec-scale disks and dusty outflows," *Proc. SPIE* **9907**, 99070R (2016).
  9. A. Léger, D. Defrère, F. Malbet, L. Labadie, and O. Absil, "Impact of  $\eta$ Earth on the Capabilities of Affordable Space Missions to Detect Biosignatures on Extrasolar Planets", *Astrophys. Rev.* **808**, 194 (2015).
  10. É. Thiébaud, "Principles of Image Reconstruction in Interferometry," *EAS Publications Series* **59**, 157–187 (2013).
  11. J. D. Monnier, S. Kraus, D. Buscher, J.-P. Berger, C. Haniff, M. Ireland, L. Labadie, S. Lacour, H. Le Coroller, R. G. Petrov, J.-U. Pott, S. Ridgway, J. Surdej, T. ten Brummelaar, P. Tuthill, and G. van Belle, "Planet formation imager (PFI): introduction and technical considerations," *Proc. SPIE* **9146**, 914610 (2014).
  12. L. Labadie, J.-P. Berger, N. Cvetojevic, R. Haynes, R. Harris, N. Jovanovic, S. Lacour, G. Martin, S. Minardi, G. Perrin, M. Roth, and R. R. Thomson, "Astronomical photonics in the context of infrared interferometry and high-resolution spectroscopy," *Proc SPIE* **9907**, 990718 (2016).
  13. S. Minardi, S. Lacour, J.-P. Berger, L. Labadie, R. R. Thomson, C. Haniff, and M. Ireland, "Beam combination schemes and technologies for the planet formation imager," *Proc SPIE* **9907**, 99071N (2016).
  14. R. W. Waynant, I. K. Ilev, and I. Gannot, "Mid-infrared laser applications in medicine and biology," *Phil. Trans. R. Soc. Lond.* **359**, 635–644 (2001).
  15. R. Muda, E. Lewis, S. O'Keefe, G. Dooly, and J. Clifford, "A compact optical fibre based mid-infrared sensor system for detection of high level carbon dioxide emissions in exhaust automotive applications," *Procedia Chem* **1**(1), 593–596 (2009).
  16. G. Z. Mashanovich, M. M. Milošević, M. Nedeljkovic, N. Owens, B. Xiong, E. J. Teo, and Y. Hu, "Low loss silicon waveguides for the mid-infrared," *Opt. Express* **19**, 7112–7119 (2011).
  17. F. Li, S. D. Jackson, C. Grillet, E. Magi, D. Hudson, S. J. Madden, Y. Moghe, C. O'Brien, A. Read, S. G. Duvall, P. Atanackovic, B. J. Eggleton, and D. J. Moss, "Low propagation loss silicon-on-sapphire waveguides for the mid-infrared," *Opt. Express* **19**, 15212–15220 (2011).
  18. L. Labadie, G. Martín, N. C. Anheier, B. Arezki, H. A. Qiao, B. Bernacki, and P. Kern, "First fringes with an integrated-optics beam combiner at 10  $\mu\text{m}$ . A new step towards instrument miniaturization for mid-infrared interferometry," *A&A* **531**, A48 (2011).
  19. A. Ródenas, G. Martín, B. Arezki, N. Psaila, G. Jose, A. Jha, L. Labadie, P. Kern, A. Kar, and R. Thomson, "Three-dimensional mid-infrared photonic circuits in chalcogenide glass," *Opt. Lett.* **37**, 392–394 (2012).
  20. G. Martin, S. Heidmann, J.-Y. Rauch, L. Jocou, and N. Courjal, "Electro-optic fringe locking and photometric tuning using a two-stage Mach-Zehnder lithium niobate waveguide for high-contrast mid-infrared interferometry," *Opt. Eng* **53**(3), 034101 (2014).
  21. R. Diener, S. Minardi, J. Tepper, S. Nolte, and L. Labadie, "All-in-one 4-telescope beam combination with a zig-zag array of waveguides," *Proc. SPIE* **9907**, 990731-990731-7 (2016).
  22. T. Baehr-Jones, A. Spott, R. Ilic, A. Spott, B. Penkov, W. Asher, and M. Hochberg, "Silicon-on-sapphire integrated waveguides for the mid-infrared," *Opt. Express* **18**(12), 12127–12135 (2010).
  23. S. Khan, J. Chiles, J. Ma, and S. Fathpour, "Silicon-on-nitride waveguides for mid- and near-infrared integrated photonics," *Appl. Phys. Lett.* **102**(12), 121104 (2013).
  24. A. Arriola, S. Mukherjee, D. Choudhury, L. Labadie, and R. R. Thomson, "Ultrafast laser inscription of mid-IR directional couplers for stellar interferometry," *Opt. Lett.* **39**, 4820–4822 (2014).
  25. S. Gross, N. Jovanovic, A. Sharp, M. Ireland, J. Lawrence, and M. J. Withford, "Low loss mid-infrared ZBLAN waveguides for future astronomical applications," *Opt. Express* **23**, 7946–7956 (2015).
  26. C. Vigreux, R. Escalier, A. Pradel, L. Bastard, J.-E. Broquin, X. Zhang, T. Billeton, G. Parent, M. Barillot, and V. Kirschner, "Telluride buried channel waveguides operating from 6 to 20  $\mu\text{m}$  for photonic applications," *Opt. Mater.* **49**, 218–223 (2015).
  27. P. Ma, D.-Y. Choi, Y. Yu, Z. Yang, S. Debbarma, S. Madden, and B. Luther-Davies, "Low-loss chalcogenide waveguides for chemical sensing in the mid-infrared," *Opt. Express* **21**, 29927–29937 (2013).
  28. H.-D. Kenchington Goldsmith, N. Cvetojevic, M. Ireland, and S. Madden, "Fabrication tolerant chalcogenide mid-infrared multimode interference coupler design with applications for bracewell nulling interferometry," *Opt.*

- Express **25**(4), 3038–3051 (2017).
29. A. Arriola, S. Gross, M. Ams, T. Gretzinger, D. Le Coq, R. P. Wang, H. Ebendorff-Heidepriem, J. Sanghera, S. Bayya, L. B. Shaw, M. Ireland, P. Tuthill, and M. J. Withford, “Mid-infrared astrophotonics: study of ultrafast laser induced index change in compatible materials,” *Opt. Mater. Express* **7**(3), 698–711 (2017).
  30. S. Gross and M. J. Withford, “Ultrafast-laser-inscribed 3D integrated photonics: challenges and emerging applications,” *Nanophotonics* **4**, 332–352 (2015).
  31. S. Minardi and T. Pertsch, “Interferometric beam combination with discrete optics,” *Opt. Lett.* **35**, 3009–3011 (2010).
  32. A. Saviuk, S. Minardi, F. Dreisow, S. Nolte, and T. Pertsch, “3d-integrated optics component for astronomical spectro-interferometry,” *Appl. Opt.* **52**(19), 4556–4565 (2013).
  33. H.-D. Nguyen, A. Ródenas, J. R. Vázquez de Aldana, J. Martínez, F. Chen, M. Aguiló, M. C. Pujol, and F. Díaz, “Heuristic modelling of laser written mid-infrared LiNbO<sub>3</sub> stressed-cladding waveguides,” *Opt. Express* **24**, 7777–7791 (2016).
  34. J. Tepper, L. Labadie, R. Diener, S. Minardi, J.-U. Pott, R. R. Thomson, and S. Nolte, “Integrated optics prototype beam combiner for long baseline interferometry in the L and M bands,” *A&A* **53**, 353–362 (2017).
  35. E. N. Glezer, M. Milosavljevic, L. Huang, R. J. Finlay, T.-H. Her, J. P. Callan, and E. Mazur, “Three-dimensional optical storage inside transparent materials,” *Opt. Lett.* **21**, 2023–2025 (1996).
  36. K. M. Davis, K. Miura, N. Sugimoto, and K. Hirao, “Writing waveguides in glass with a femtosecond laser,” *Opt. Lett.* **21**, 1729–1731 (1996).
  37. K. Goel and W. Chang, “Extinction ratio degradation due to asymmetry in zero-gap directional coupling and crossing channel switches,” *IEEE J. Quantum. Electron.* **23**(12), 2216–2223 (1987).
  38. M. M. Colavita, “Fringe Visibility Estimators for the Palomar Testbed Interferometer,” *PASP* **111**, 111–117 (1999).
  39. J. Tepper, R. Diener, L. Labadie, S. Minardi, B. Muthusubramanian, J.-U. Pott, S. Nolte, A. Arriola, G. Madden, D. Choudhury, W. N. MacPherson, and R. R. Thomson, “Increasing the spectral coverage of interferometric integrated optics: K/l and n-laser-written beam combiners,” *Proc. SPIE* **9907**, 990719 (2016).
  40. J.-P. Berger, K. Rousselet-Perraut, P. Kern, F. Malbet, I. Schanen-Dupont, F. Reaynaud, P. Haguenaud, and P. Benech, “Integrated optics for astronomical interferometry,” *A&A* **139**, 173–177 (1999).
  41. V. Coudé du Foresto, G. Perrin, and M. Boccas, “Minimization of fiber dispersion effects in double Fourier stellar interferometers,” *A&A* **293**, 278–286 (1995).
  42. M. Benisty, J.-P. Berger, L. Jocou, P. Labeye, F. Malbet, K. Perraut, and P. Kern, “An integrated optics beam combiner for the second generation VLTI instruments,” *A&A* **498**, 601–613 (2009).
  43. R. Diener, J. Tepper, L. Labadie, T. Pertsch, S. Nolte, and S. Minardi, “Towards 3D-photonics, multi-telescope beam combiners for mid-infrared astrointerferometry,” *Opt. Express* (to be published).
  44. S. Gross, M. Ams, G. Palmer, C. T. Miese, R. J. Williams, G. D. Marshall, A. Fuerbach, D. G. Lancaster, H. Ebendorff-Heidepriem, and M. J. Withford, “Ultrafast laser inscription in soft glasses: A comparative study of athermal and thermal processing regimes for guided wave optics,” *Int. J. Appl. Glass Sci.* **3**(4), 332–348 (2012).
  45. B. McMillen, B. Zhang, K. P. Chen, A. Benayas, and D. Jaque, “Ultrafast laser fabrication of low-loss waveguides in chalcogenide glass with 0.65 dB/cm loss,” *Opt. Lett.* **37**, 1418–1420 (2012).

## 1. Introduction

Achieving high angular resolution observations in astronomy is key to a large number of science cases encompassing, for instance, the investigation of planet formation in circumstellar disks [1, 2], the spectroscopic characterization of exoplanetary atmospheres [3, 4], stellar physics [5, 6], or the study of the innermost regions in active galactic nuclei [7, 8]. Ground-based seeing-limited observations typically reach about an angular resolution of 1". Significantly finer resolution can be obtained with adaptive optics or with interferometric techniques as implemented at the VLTI, CHARA, NPOI observatories, or from space [9]. An astronomical interferometer consists of several apertures tens to hundreds meters apart, whose light is simultaneously coherently combined to create an interferogram from which the spatial structure of the observed object can be constrained/imaged with milliarcsecond resolution. The heart of an infrared interferometer is the beam combiner, whose role is to coherently combine the beams from the individual telescopes. Recent progress in optical instrumentation and photonics has permitted to develop innovative solutions such as multi-beam single-mode integrated optics combiners to replace classical bulk optics designs in long-baseline interferometry. This offers unique improvement in terms of stability of the instrumental transfer function, which is a prerequisite to measuring calibrated interferometric visibilities with the highest accuracy and hence accessing a high dynamic range for image reconstruction [10]. Such a technology could play a great role in future multi-aperture interferometric instruments such as the planet formation imager (PFI) [11].

Fiber-fed single-mode interferometric integrated optics (IO) beam combiners are now scientifically operational on instruments like PIONIER and GRAVITY at the VLTI (cf. [12] for a review). Unfortunately, a limitation of current IO beam combiners with respect to bulk optics solutions resides in their insufficient wavelength coverage beyond  $\sim 2\ \mu\text{m}$ , i.e. the transparency cut-off wavelength of silica. Using OH-free silica, the transparency range can be greatly increased up to  $3.5\ \mu\text{m}$ , which would potentially allow to apply well-established lithographic methods. This was tested for the GRAVITY beam combiner but resulted in strong dispersion, hampering high interferometric contrasts (Laurent Jocou, personal communication). Also, the important astronomical L' band cannot be accessed and out-of-plane waveguides cannot be easily achieved by this technique.

Considering the richness of the mid-infrared range for high-angular resolution astrophysics and the instrumental benefit of the integrated solution in interferometry, this has motivated further developments of multi-telescope IO beam combiners using alternative dielectric substrates transparent in the  $2\text{-}12\ \mu\text{m}$  range [13]. Such mid-IR IO would hold application potential not only in astronomy but also in other areas such as medicine [14] or environmental monitoring [15]. The basic need is to benefit from a stable technological platform capable of producing high-throughput single-mode waveguides in mid-infrared materials, in a comparable manner to what the telecom-driven photo-lithographic platform has provided for forty years for silica-based integrated optics and fibers. At longer wavelengths beyond  $2\ \mu\text{m}$ , several technologies tested over the last decade succeeded in manufacturing proof-of-concept mid-infrared waveguides and combining functions: the used platforms included chemical etching/lithography, laser-inscription in glass substrates, ion-exchange and diffusion in glasses [16–29].

In this paper, we concentrate on using Ultrafast laser inscription (ULI) [30] to inscribe and characterize interferometric couplers in fluoride glasses. A great advantage of laser inscription is that waveguides can be inscribed in all three dimensions, which then allows to experiment with novel beam combination schemes such as all-in-one discrete beam combiners [31, 32]. Two- and three-port couplers for the mid-IR range were successfully laser-inscribed in GLS (Gallium Lanthanum Sulfide) and GCIS glasses [19]. Propagation losses on the order of  $0.8\ \text{dB/cm}$  and balanced monochromatic splitting ratios were reported [24]. ULI has also been used to inscribe depressed cladding waveguides in crystals. Nguyen et al 2016 [33] has presented a heuristic theoretical analysis of laser writing in Lithium Niobate along with experimental results at  $3.68\ \mu\text{m}$ . Yet, the reported measured propagation losses of  $2.9\ \text{dB/cm}$  for TE and no guidance for TM modes, are still impractical for astronomical applications. Recently, a comprehensive interferometric study on laser-inscribed couplers in GLS glass evidenced low dispersion properties and low differential birefringence and showed for the first time high broadband instrumental contrast well above 90% over the L and M band [34]. The ULI technique has also been applied to ZBLAN, a fluorozirconate glass, showing propagation losses as low as  $0.3\ \text{dB/cm}$  and a functioning evanescent coupler over the  $3.75\text{-}4.2\ \mu\text{m}$  range [25]. Although this work has evidenced the great potential of the ZBLAN platform, no further interferometric characterization has been reported yet.

This paper experimentally measures the critical properties of the laser-inscribed ZBLAN couplers for interferometry applications over the L and L' bands ( $3\text{ to }4\ \mu\text{m}$ ). It includes the total throughput, spectral splitting ratio, dispersion properties and most importantly the instrumental interferometric contrast. In order to move forward to a science qualified mid-IR IO interferometric instrument, it is essential to obtain a detailed picture on the experimental performance achievable with promising mid-IR IO technologies. With this work, we contribute to this objective and, in particular, provide a comparative study to the ULI-GLS platform.

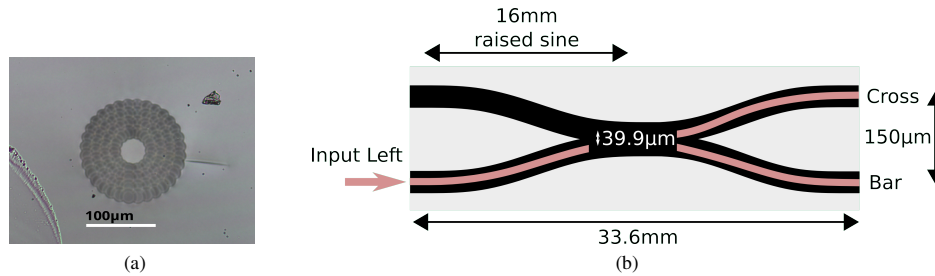


Fig. 1. Figure 1(a) shows the cross-section of a laser-inscribed channel waveguide written with similar parameters as used for the coupler. In Fig. 1(b), the design parameters of the coupler studied in this paper are depicted. The terms Cross and Bar are used to distinguish the originally excited and the coupled waveguide. Left and right orientation is used as seen from the camera.

## 2. Design and fabrication of the sample

The waveguides were inscribed into a ZBLAN substrate using ULI, a technique pioneered 20 years ago by Glezer et al 1996 [35] and Davis et al 1996 [36]. An intense femtosecond laser is tightly focused inside the substrate and causes a local and permanent change in refractive index. By translating the substrate waveguides can be inscribed into the sample. An extensive review of the ULI technique is found in Gross & Withford (2015) [30].

In the case of ZBLAN, the laser-induced change in refractive index is negative, i.e. the cladding of the waveguides is inscribed. The writing laser is a Ti:sapphire oscillator with a 5.1 MHz repetition rate and  $<50$  fs pulses at 800 nm. The laser is focused  $300\ \mu\text{m}$  below the polished surface of the substrate using a 1.25 NA objective. The substrate is then translated with a speed of 1000 mm/min and the energy per pulse is 65 nJ. The achieved contrast in refractive index is about  $-(6 \pm 1) \cdot 10^{-4}$ . The  $60\ \mu\text{m}$  wide cladding of each waveguide consists of 108 laser modifications around a  $50\ \mu\text{m}$  diameter circular core. Figure 1(a) shows the waveguide cross section of a channel waveguide inscribed with similar parameters. The sample at hand contains 12 straight waveguides and six couplers and measures a total length of 33.6 mm. The properties of the coupler used in this paper are depicted in Fig. 1(b). The coupler has an interaction length of 0 mm, i.e. the two waveguides converge and directly depart, and a raised sine length of 16 mm. The separation between the two waveguides in the interaction area is  $39.9\ \mu\text{m}$  (measured as the distance between the centers of the two cores), i.e. the waveguides overlap. More information on the fabrication of the sample can be found in Gross et al 2015 [25].

The principal design of the component is the one of a 2x2 directional coupler which has two inputs and two outputs. In the interaction area the two channels are brought in proximity or to overlap where the two fields mix [37]. Ideally, the two outputs contain each a mixed field with a  $\pi$  phase shift with respect to each other due to the conservation of energy. The advantage of this design is that the losses are only determined by the propagation and bending losses, whereas the Y-Junction inherently reflects 50% of the light. Also, such a design is the building block of an ABCD combiner [38]. Yet, the directional coupler naturally exhibits a chromatic splitting ratio, which will be discussed in this paper.

## 3. Experimental setup

We use a two-arm interferometric setup for the characterization of the sample as depicted in Fig. 2. For the broadband measurements, we use a fibre-coupled blackbody source that is spatially filtered by a  $20\ \mu\text{m}$  pinhole and collimated by an  $f=50\text{mm}$  achromat. In addition, a spatially

filtered HeNe Laser at  $3.39\ \mu\text{m}$  is inserted into the setup which can be positioned with respect to the broadband source by a beamsplitter. The beam is split into two beams using a thin pellicle beamsplitter (Thorlabs, BP145B4) in order to avoid differential dispersion in the beamsplitter. The two beams are then reflected by two mirrors: one mirror is mounted on a delay line (Thorlabs, Z812B) in order to control the optical path difference (OPD), the other mirror can be tilted in order to fine-position the beam with respect to the other. The two beams are then injected by an  $f=50\text{mm}$  achromat into the IO chip. The chip is mounted on a translational stage which can be fine-positioned in three dimensions. The outputs of the chip are collimated by another  $f=50\text{mm}$  achromat and re-imaged by the infrared camera (Infratech 5360S) with an  $f=50\text{mm}$  lens. A bandpass filter can be inserted in order to test the performance over the L and L' band. Our camera adds an intrinsic noise at about  $25\ \text{kHz}$  (corresponding to  $0.5\ \mu\text{m}$ ), which we filtered out, as this can lead to falsely measuring too high interferometric contrasts [39].

We also use this setup to perform Fourier transform spectroscopy. Therefore, it is critical to precisely record the OPD of the interferometric measurements. The delay line, however, does not provide a highly accurate or repeatable translation. Therefore, we record the interferometric signal of the HeNe laser at  $3.39\ \mu\text{m}$  simultaneously to the broadband measurement. As the fringe spacing of the laser is known, we use it to calibrate the OPD. The advantage of the Fourier Transform approach, as opposed to a fiber-coupled spectrometer, lies in the possibility to measure the two chip outputs separately as they are imaged onto the detector of the camera.

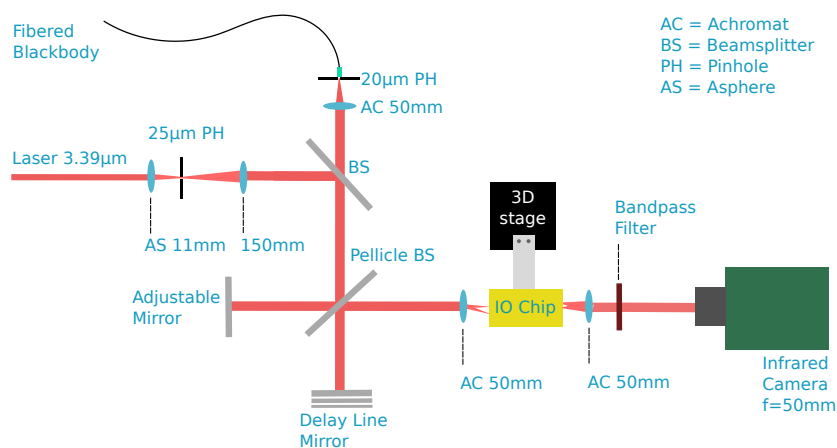


Fig. 2. Design of the experimental setup for interferometric characterization of the ZBLAN integrated optics chip. Bandpass filters L and L' can be inserted.

## 4. Results

### 4.1. Splitting ratio

The spectral shape of the splitting ratio of the directional coupler is crucial to its interferometric performance in broadband operation. When the coupler operates with monochromatic light, an unbalanced splitting (i.e. not 50/50) can be easily calibrated by photometric correction. On the contrary, when operating with polychromatic stellar light within a bandpass filter, the chromatic unbalance of the splitting ratio across the band will result into a degradation of the instrumental contrast, which cannot be compensated photometrically. The degradation effect of the chromaticity of the splitting ratio will occur even if the coupler exhibits a balanced (50/50) splitting ratio integrated over the filter bandwidth.

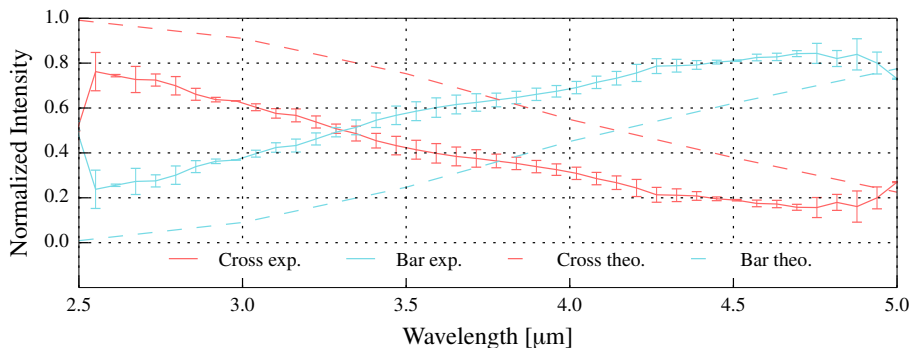


Fig. 3. The splitting ratio of the coupler as a function of wavelength. Bar and Cross denote the originally injected and the coupled waveguide, respectively, (cf. Fig. 1(b)). The solid lines depict the measured values and the dashed lines depict the RSoft simulation.

The sample contains six couplers, each inscribed with varying the parameters. The coupler which showed the most balanced integrated splitting ratio across the L band was chosen to be eventually characterized. After testing the available couplers for photometric unbalance, the selected sample exhibits an integrated splitting ratio of 45% and 34% over the L and L' band, respectively. The design parameters of this coupler are depicted in Fig. 1(b).

In order to measure the splitting ratio as a function of wavelength, we inject the two arms of the interferometric setup into the same input. Scanning the OPD, each output yields one interferogram, from which the respective spectrum can be derived through Fourier transform spectroscopy. We performed this measurement for the left and right input, from which we yield an average splitting ratio. For this measurement, we initially do not insert any bandpass filter, so that the bandwidth covers the whole accessible spectral range (2.5 - 5  $\mu\text{m}$ ) offered by the infrared fiber, the optical setup and the ZBLAN component. Figure 3 shows the mean spectral splitting ratio along with the standard deviation as error bars. We find a quasi linear dependency ranging from about 25% to 80% from 2.5 to 5.0  $\mu\text{m}$  with a slope of about  $0.3\mu\text{m}^{-1}$ . Over the L (3.1-3.5  $\mu\text{m}$ ) and L' (3.6-4.0  $\mu\text{m}$ ) band the splitting ratio varies, from edge to edge of the respective band, from 40% to 57% and from 57% to 70%. The 50/50 crossing point is at 3.3  $\mu\text{m}$ .

We modeled the splitting ratio by an RSoft simulation with a depressed cladding index of  $\Delta n = -7 \cdot 10^{-4}$  and using the geometry of the coupler depicted in Fig. 1(b). The model reproduces the slope across the bandwidth but shows an offset of about 30%, see Fig. 3. The simulation can be matched with the measured splitting ratio by tuning the separation of the waveguides in the coupling region to 36  $\mu\text{m}$ .

#### 4.2. Transmission

In this section, we present both the average total throughput in the L band and the transmission spectrum from 2.5 to 5.0  $\mu\text{m}$ . Maintaining a high throughput in photon-starved applications like astronomy is clearly important if one considers, for instance, that the VLTI transmission from the primary mirror down to the interferometric combination laboratory is only  $\sim 20\%$  at 2  $\mu\text{m}$  before entering any instrument.

In order to estimate the total throughput, it is essential that the numerical aperture (NA) of the injection beam matches the NA of the waveguide. Therefore, we placed an iris in the collimated beam before the injection lens to modify the injection spot size – and the coupling efficiency

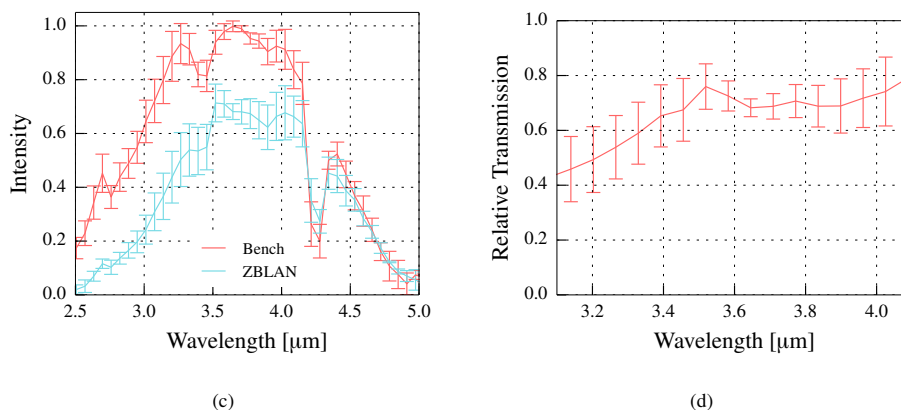


Fig. 4. Figure 4(a) shows the normalized transmission of the experimental setup compared to the transmission of the ZBLAN sample. The ZBLAN curve was scaled with respect to the bench matching the measured total throughput of 58% over the L band. For each case, three measurements were taken from which the average and the standard deviation is calculated. The dip at 4.2  $\mu\text{m}$  is due to  $\text{CO}_2$  absorption. Figure 4(b) shows the relative transmission of the ZBLAN sample calculated from the ratio of the curves from Fig. 4(a) over the relevant the L and L' band up to the  $\text{CO}_2$  absorption.

accordingly – and measured the throughput for different iris diameters  $D$ . The results are shown in table 1. We find the highest throughput of 58% for an iris size of 6 mm which corresponds to an  $\text{NA} \sim D/2f$  of  $0.06 \pm 0.01$  (error due to sampling of the beam diameter). If we take into account the attenuation due to Fresnel reflections (4% at the input and output facet for  $n_{\text{ZBLAN}} \sim 1.50$ ) and the maximum coupling efficiency (82%) between the Airy pattern and the Gaussian-like waveguide mode, we are left with an excellent transmission of 76% of the sample including bending and propagation losses, which translates into 1.19dB (0.33 dB/cm). The measured NA is in line with what was measured by [25] for another coupler (but with the same refractive index contrast) in this sample. Table 1 also shows that the transmission for the left and right input are very similar.

Table 1. Throughput of the 33.6 mm long  $2 \times 2$  combiner in L band (FWHM: 3.1-3.6  $\mu\text{m}$ ) for different input beam diameters.

Beam diameter	4 mm	6 mm	8 mm	11 mm
Left Input	56%	58%	39%	23%
Right Input	55%	58%	39%	22%

In order to measure the spectral transmission of the sample, we use the data from the interferometric measurements from section 4.1 and performed Fourier transform spectroscopy. The sum of the two output spectra is the totally transmitted spectrum, which can be compared to the spectrum of the setup without component. We find a relatively flat spectral transmission along the measured bandwidth with a slightly lower transmission towards shorter wavelength, see Fig. 4(a). This may be explained by the fact that the coupling cannot be equally optimized for all wavelengths across the spectrum. Figure 4(b) allows to assume that the total throughput will not be significantly less in the L' than has been measured for the L band.

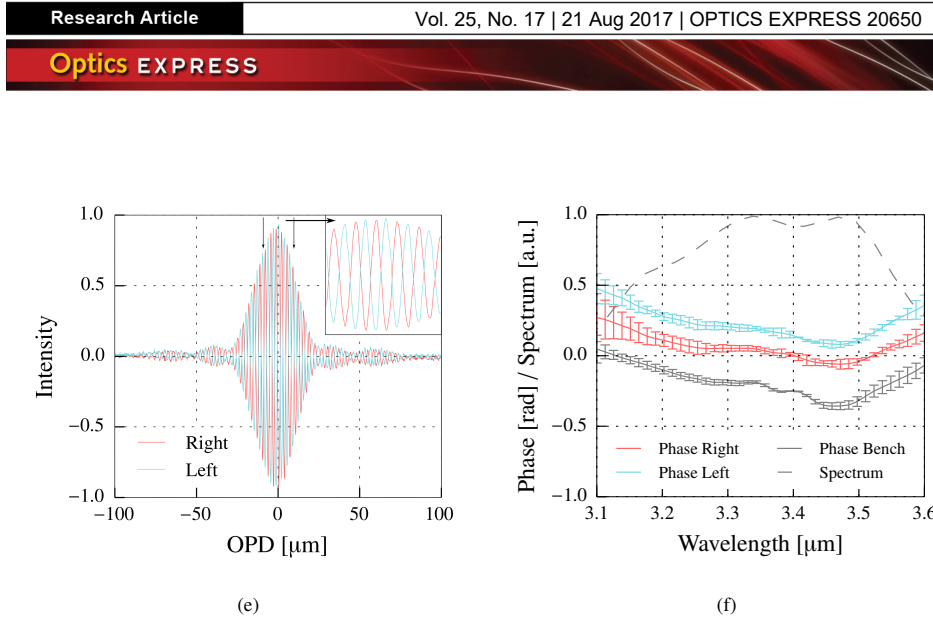


Fig. 5. Figure 5(a) shows the experimental L band interferogram after photometric correction of the two chip outputs with a contrast of 93.0%. The inset magnifies the central region and demonstrates the near- $\pi$  phase shift. Figure 5(b) shows the corresponding bandwidth of the interferogram across the band. The right phase is set to zero at 3.4  $\mu\text{m}$  and the left phase is lowered by  $\pi$  to visualize the near- $\pi$  phase shift between the two outputs. The phase of the bench is lowered by 0.25 for better visualization.

#### 4.3. Interferometric characterization

In this section we test the coupler for interferometric beam combination as it is eventually intended to operate in an interferometric instrument. The interferograms presented are photometrically corrected and recorded for unpolarized light. Each interferogram is recorded three times from which a mean and standard deviation are computed.

Using the L band filter with 0.4  $\mu\text{m}$  FWHM, we test the interferometric performance over the 3.1 to 3.5  $\mu\text{m}$  range (see Fig. 5(b) for the spectrum of the measurement). Figure 5(a) shows the two interferometric outputs of the chip with a high broadband contrast of  $C_L = 93.0 \pm 1.3\%$  in unpolarized light. The near- $\pi$  phase shift between the two coupler's outputs is qualitatively visible in the inset. The high contrast evidences the small level of differential birefringence between the two coupler's two channels, an effect visible in other studies. A low differential birefringence allows to operate the component in unpolarized light without having to split the two orthogonal polarizations [40].

A typical limitation of IO combiners for broadband interferometry is differential dispersion which stems from different propagation constants and/or different lengths between the two waveguides that form the coupler. This results in different OPDs for different wavelengths and a smeared out interferogram with an attenuated contrast. This is detrimental to astronomical interferometry where the instrumental visibility should be as close as possible to one. In Fig. 5(a), we can clearly identify the first and second lobe of the interferogram, which is an excellent indicator for a low differential dispersion. Yet, the effect of the differential dispersion can be further investigated qualitatively by analyzing the phase curvature of the interferogram [41]. A flat phase – i.e. with a zero first derivative against wavelength – corresponds to a perfectly dispersion-free interferogram. The phase is estimated through the real and imaginary part of the Fourier transform of the interferogram. Figure 5(b) depicts the variation of the phase of the left and right output across the spectrum, quantifying the dispersion present in the interferogram. The phases of the right and left outputs exhibit almost the same curvature across the band, pointing at

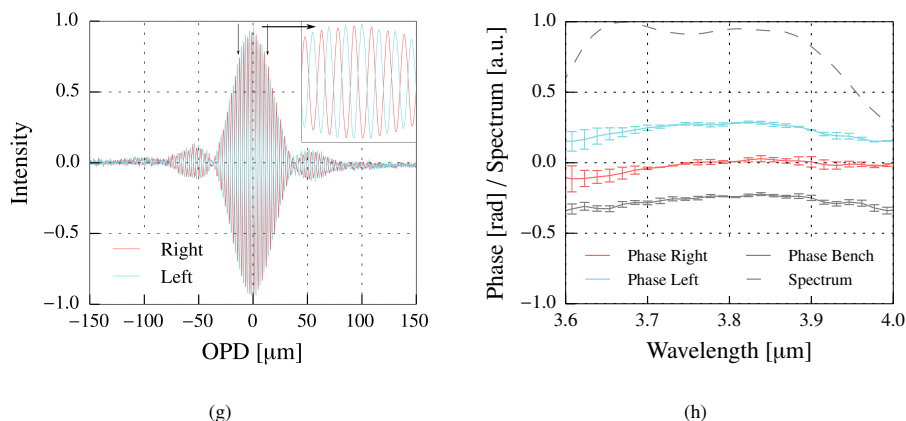


Fig. 6. Figure 6(a) shows the experimental L' band interferogram after photometric correction of the two chip outputs with a contrast of 93.5% along with an inset of the central region. Figure 6(b) shows the corresponding bandwidth of the measurement and the phase variation of the interferogram. The right phase is set to zero at 3.8 μm and the left phase is lowered by  $\pi$  to visualize the near- $\pi$  phase shift between the two outputs. The phase of the bench is lowered by 0.25 for better visualization.

identical behaviours in terms of dispersion. We also measured the phase without component – i.e. of the experimental setup – for which we would expect a flat phase. We find that its phase curvature is very similar to the component's one, which indicates that the experimental phase curvature is dominated by our setup, possibly because of the pellicle beamsplitter which has a very small but non-zero thickness. After subtracting the dispersion due to our bench, we find a residual phase variation of  $\sigma_L = 0.02$  rad (measured as the standard deviation across the band) intrinsic to the component. This variation is within the error bars of the measurement. Note that the absolute offset of the bench's phase is not relevant here, only its curvature is. In Fig. 5(b) the left output phase was artificially lowered by an offset of  $\pi$  for visualization purposes. The left and right phases should then have overlapped with each other, which is not the case here with a residual offset of about 0.2 rad. The two interferograms not being in perfect phase opposition points to additional losses.

We conducted the same test by inserting the L' band filter ( $\lambda_c=3.8$  μm, FWHM=0.4 μm) into the setup (see Fig. 6(b) for the measured bandwidth). The same coupler that was used for the L band shows interferometric outputs with a high broadband contrast of  $C_{L'} = 93.5\% \pm 0.2\%$  over the L' band as seen in Fig. 6(a). As for the L band, we find that the phase curvature mainly results from the experimental setup (see Fig. 6(b)). The residual phase variation after removing the bench is again on the order of  $\sigma_{L'} = 0.02$  rad. Similarly, we find that the phase shift between the two outputs is not exactly  $\pi$  but about 0.3 rad off.

## 5. Discussion and conclusion

We have demonstrated that ULI in ZBLAN is a suitable platform to manufacture good quality  $2 \times 2$  directional couplers as the basic brick for single-mode integrated optics mid-infrared beam combiners.

We measure high broadband interferometric contrasts of 93.0% and 93.5% in unpolarized light over the L and L' band, respectively, with spectral bandwidths of  $\sim 0.4$  μm. The origins of

fringe contrast loss are typically an unbalanced spectral splitting ratio, differential dispersion, differential birefringence, multimode behaviour, or improper photometric correction.

At first we assessed the splitting ratio of the coupler and found a variation of less than  $0.3/\mu\text{m}$ . These are promising results as the spectral splitting ratio is flatter than the recently reported directional evanescent coupler inscribed in GLS glass [34] for which a slope of  $0.8/\mu\text{m}$  was measured. For this ZBLAN coupler, the measured spectral unbalance of the splitting ratio would result in a contrast loss of about 1%. The crossing point lies at  $3.3\mu\text{m}$ . In order to obtain a high raw contrast (i.e. before photometric correction), it is important that the crossing point of the splitting ratio lies in the center of the bandwidth. The position of the crossing point can be fine-tuned by altering the separation of the waveguides in the interaction area.

The dispersion in the interferogram, measured as the phase variation across the band, is dominated by our experimental setup. The intrinsic differential dispersion of the component itself introduces a phase curvature of less than 0.02 rad over both L and L' band. These are similar results as for the GLS sample measured in Tepper et al 2017 [34]. Therefore, we can conclude that laser inscription is capable of repeatedly inscribing waveguides with precisely equalized lengths and propagation constants (cf. [41], Eq.15). Our simulations indicate that the phase curvature of the setup results into a contrast loss not larger than 0.8%.

The core size of  $50\mu\text{m}$  and the  $\Delta n$  of  $\sim 6 \times 10^{-4}$  point in the first order to a single-mode behavior at these mid-IR wavelengths with a normalized frequency  $V$  well below 2.405. This can be confirmed on a later stage through classical near-field imaging.

A detailed study of the differential birefringence is not reported in this paper. Although we do not expect high differential birefringence in light of the high broadband contrast, this is still an effect that, if not controlled, may introduce additional contrast loss of few percents. This will be assessed later by investigating the evolution of the monochromatic interferometric contrast at  $3.39\mu\text{m}$  for different angular directions of the input linear polarization by using a  $\lambda/2$  plate.

Finally, since the photometric channels are not recorded simultaneously to the interferometric signal, the photometric correction may add additional systematic biases given the randomness of the delay-line mirror tip-tilt when coupling in the component's channel. This may lead in some cases to an underestimated instrumental calibrated contrast. This will be assessed in the future through the acquisition of a large number of repeated contrast measurements.

Concerning the sample transmission, we measured a very high throughput of 58% over the L band including coupling losses and Fresnel reflections. We find that the spectral transmission is relatively flat over the 3 to  $4\mu\text{m}$  range of interest. Evanescent couplers in GLS have shown a lower total throughput of 25% [34], partly hampered by the higher Fresnel losses. The larger throughput could be a significant advantage, although the GLS platform provides a wider transparency range up to  $\sim 10\mu\text{m}$  compared to the cutoff of ZBLAN at about  $5\mu\text{m}$ . Gross et al 2015 [25] reported propagation losses of 0.29 dB/cm in ZBLAN channel waveguides. By comparing this value to the measured 0.33 dB/cm for the coupler, we can derive the important result that additional bendings do not introduce significant losses.

From the analysis of the phase we could determine that the phase shift between the two outputs is not exactly  $\pi$  but by about 0.2-0.3 rad off this value. As the  $\pi$  phase shift is a consequence of energy conservation in the coupler, this result points to additional, albeit small, flux losses in the cladding that are not seen in the GLS couplers. This could result from small bending or scattering losses in the interaction area during the process of energy transfer from one waveguide to the other. More importantly, this possible deviation from the expected  $\pi$  phase shift needs to be understood and controlled if the ZBLAN platform would be used to manufacture ABCD integrated optics combiners [42] for which the phase opposition and quadratures have to be accurately guaranteed.

So far, laser inscription in ZBLAN has not capitalized on the 3D potential of ULI. While functioning 3D ABCD couplers have been inscribed into GLS [43], it is not yet clear whether the

negative writing in ZBLAN allows for more complex functions due to its smaller refractive index contrast and consequently limited mode confinement; a critical aspect that needs to be targeted in the next phase. Gross et al 2012 [44] has demonstrated the feasibility of higher refractive index contrast in ZBLAN (up to  $4 \cdot 10^{-3}$ ) at the expense of slower manufacturing.

It should be noted that the performance of both the ZBLAN and the GLS couplers critically depend on the chosen laser writing parameters as well as the design of the coupler (cf. McMillen et al 2012 [45]). In this work, as well as in Tepper et al 2017 [34], the best performing coupler was picked from a number of couplers (6 and 20, respectively) without a detailed previous parameter scan over all possible inscription configurations. Thus, there may still be room for potential improvement in the waveguide properties for both technological platforms.

With this work, we have presented a comprehensive quantitative comparison of the performances of two promising ULI platforms, namely ZBLAN and GLS glasses. We confirm the strong potential of the ZBLAN platform to produce the basic bricks for mid-IR integrated optics with this first interferometric characterization.

### Funding

Bundesministerium für Bildung und Forschung (BMBF) (05A14PK2, 05A14SJA); Australian Research Council Centre of Excellence for Ultrahigh bandwidth Devices for Optical Systems (CUDOS) (CE110001018).

### Acknowledgements

JT, LL, SM and RD acknowledge the financial support of the German Ministry of Research and Education (BMBF) through the ALSI project.

This research was supported by the Australian Research Council Centre of Excellence for Ultrahigh bandwidth Devices for Optical Systems (project number CE110001018) and an ARC Discovery Project, and was performed in part at the Optofab node of the Australian National Fabrication Facility using Commonwealth and NSW and SA State Government funding. S. Gross acknowledges funding by an Australian Research Council DECRA Fellowship.

The authors thank the anonymous referees for the constructive remarks.



## Paper 3 (Diener 2017): Towards 3D-photonic, multi-telescope beam combiners for mid-infrared astrometry

In the third paper, we go beyond the classical two-telescope  $2 \times 2$  couplers that were investigated in the previous publications and test advanced beam combining schemes. Our colleagues in Jena produced two-telescope ABCD couplers and a four-telescope zig-zag array (c.f. Fig. 3.4). In Cologne, I performed the measurements on the ABCD coupler.

In this publication, we first discuss the concept of the V2PM matrix and its calibration procedure. From the experimental characterization, we find that the advanced beam combiners can indeed retrieve the visibility and phase of the input light fields. Finally, the impact of the different beam combining concepts on the signal-to-noise ratio is discussed.

The results were published in the peer-review journal *Optics Express*.



## Towards 3D-photonic, multi-telescope beam combiners for mid-infrared astrometry

ROMINA DIENER,<sup>1</sup> JAN TEPPER,<sup>2</sup> LUCAS LABADIE,<sup>2</sup>  
THOMAS PERTSCH,<sup>1</sup> STEFAN NOLTE,<sup>1,3</sup> AND STEFANO MINARDI<sup>1,4,\*</sup>

<sup>1</sup>Institute of Applied Physics, Abbe Center of Photonics, Friedrich Schiller University Jena, Albert-Einstein Str. 15, 07745 Jena, Germany

<sup>2</sup>1st Institute of Physics, University of Cologne, Zulpicher Str. 77, Cologne, Germany

<sup>3</sup>Fraunhofer Institute for Applied Optics and Precision Engineering, Albert-Einstein-Strasse 7, 07745 Jena, Germany

<sup>4</sup>inoFSPEC, Leibniz Institute for Astrophysics Potsdam, An der Sternwarte 16, 14482 Potsdam, Germany  
\*stefano@stefanominardi.eu

**Abstract:** In the past two decades high precision optical astronomical interferometry has benefited from the use of photonic technologies. Today, near-infrared interferometric instruments deliver high-resolution, hyperspectral images of astronomical objects and combine up to 4 independent telescopes at a time thanks to integrated optics (IO). Following the success of IO interferometry, several initiatives aim at developing components which could combine simultaneously more telescopes and extend their operation beyond the near-infrared bands. Here we report on the development of multi-telescope IO beam combiners for mid-infrared interferometry exploiting the three-dimensional (3D) structuring capabilities of ultrafast laser inscription. We characterise the capability of a 2-telescope and a 4-telescope beam combiner to retrieve the visibility amplitude and phase of monochromatic light fields at a wavelength of 3.39  $\mu\text{m}$ . The combiner prototypes exploit different 3D architectures and are written with a femtosecond laser on substrates of gallium lanthanum sulfide. Supporting numerical simulations of the performance of the beam combiners show that there is still room for improvement and indicate a roadmap for the development of future prototypes.

© 2017 Optical Society of America

**OCIS codes:** (130.3120) Integrated optics devices; (120.3180) Interferometry; (350.1260) Astronomical optics.

### References and links

1. M. Born and E. Wolf, *Principles of Optics* (Cambridge, 1999), Chap. 10.
2. <http://www.evlbi.org>
3. <https://almascience.eso.org/about-alma/alma-basics>
4. <http://www.eso.org/sci/facilities/paranal/telescopes/vlti.html>
5. M. J. Ireland, A. Mérand, T. A. ten Brummelaar, P. G. Tuthill, G. H. Schaefer, N. H. Turner, J. Sturmann, L. Sturmann, and H. A. McAlister, "Sensitive visible interferometry with PAVO," *Proc. SPIE* **7013**, 701324 (2008).
6. G. Giovannini, W. D. Cotton, L. Ferretti, L. Lara, and T. Venturi, "VLBI observations of a complete sample of radio galaxies: 10 years later," *Astroph. J.* **552**, 508–526 (2001).
7. D. F. Buscher, J. E. Baldwin, P. J. Warner, and C. A. Haniff, "Detection of a bright feature on the surface of Betelgeuse," *Month. Not. R. Astron. Soc.* **245**, 7P–11P (1990).
8. J. D. Monnier, M. Zhao, E. Pedretti, N. Thureau, M. Ireland, P. Muirhead, J. P. Berger, R. Millan-Gabet, G. Van Belle, T. ten Brummelaar, H. McAlister, S. Ridgway, N. Turner, L. Sturmann, J. Sturmann, and D. Berger, "Imaging the Surface of Altair," *Science* **317**, 342–345 (2007).
9. X. Haubois, G. Perrin, S. Lacour, T. Verhoelst, S. Meimon, L. Mugnier, E. Thiébaud, J. P. Berger, S. T. Ridgway, J. D. Monnier, R. Millan-Gabet, and W. Traub, "Imaging the spotty surface of Betelgeuse in the H band," *Astron. Astroph.* **508**, 923–932 (2009).
10. R. van Boekel, M. Min, C. Leinert, L. B. F. M. Waters, A. Richichi, O. Chesneau, C. Dominik, W. Jaffe, A. Dutrey, U. Graser, T. Henning, J. de Jong, R. Köhler, A. de Koter, B. Lopez, F. Malbet, S. Morel, F. Paresce, G. Perrin, T. Preibisch, F. Przygodda, M. Schöller, and M. Wittkowski, "The building blocks of planets within the 'terrestrial' region of protoplanetary disks," *Nature* **432**, 479–482 (2004).
11. ALMA Partnership, C. L. Brogan, L. M. Pérez, R. T. Hunter, W. R. F. Dent, A. S. Hales, R. E. Hills, S. Corder, E. B. Fomalont, C. Vlahakis, Y. Asaki, D. Barkats, A. Hirota, J. A. Hodge, C. M. V. Impellizzeri, R. Kneissl, E. Liuzzo, R. Lucas, N. Marcelino, S. Matsushita, K. Nakanishi, N. Phillips, A. M. S. Richards, I. Toledo, R. Aladro, D. Brogiere, J. R. Cortes, P. C. Cortes, D. Espada, F. Galarza, D. Garcia-Appadoo, L. Guzman-Ramirez, E. M.

- Humphreys, T. Jung, S. Kamenon, R. A. Laing, S. Leon, G. Marconi, A. Mignano, B. Nikolic, L.-A. Nyman, M. Radiszcz, A. Remijan, J. A. Rodón, T. Sawada, S. Takahashi, R. P. J. Tilanus, B. Vila Vilaro, L. C. Watson, T. Wiklind, E. Akiyama, E. Chapillon, I. de Gregorio-Monsalvo, J. Di Francesco, F. Gueth, A. Kawamura, C.-F. Lee, Q. Nguyen Luong, J. Mangum, V. Pietu, P. Sanhueza, K. Saigo, S. Takakuwa, C. Ubach, T. van Kempen, A. Wootten, A. Castro-Carrizo, H. Francke, J. Gallardo, J. Garcia, S. Gonzalez, T. Hill, T. Kaminski, Y. Kuroono, H.-Y. Liu, C. Lopez, F. Morales, K. Plarre, G. Schieven, L. Testi, L. Videla, E. Villard, P. Andreani, J. E. Hibbard, and K. Tatematsu, "The 2014 ALMA Long Baseline Campaign: First Results from High Angular Resolution Observations toward the HL Tau Region," *Astrophys. J.* **808**, L3 (2015).
12. J. Bland-Hawthorn, and P. Kern, "Astrophotonics: a new era for astronomical instrumentation," *Opt. Express* **17**, 1880–1884 (2009).
  13. V. Coudé du Foresto, S. Ridgway, and J.-M. Mariotti, "Deriving object visibilities from interferograms obtained with a fiber stellar interferometer," *Astron. Astrophys. Suppl. Ser.* **121**, 379–392 (1997).
  14. F. Malbet, P. Kern, I. Schanen-Duport, J.-P. Berger, K. Rousselet-Perraut, P. Benech, "Integrated optics for astronomical interferometry," *Astron. Astrophys. Suppl. Ser.* **138**, 135–145 (1999).
  15. J.-P. Berger, P. Hagenauer, P. Kern, K. Perraut, F. Malbet, I. Schanen, M. Severi, R. Millan-Gabet, and W. Traub, "Integrated optics for astronomical interferometry - IV. First measurements on stars," *Astron. Astrophys.* **376**, L31–L34 (2001).
  16. L. Jocou, K. Perraut, T. Moulin, Y. Magnard, P. Labeye, V. Lapras, A. Nolot, G. Perrin, F. Eisenhauer, C. Holmes, A. Amorim, W. Brandner, and C. Straubmeier, "The beam combiners of Gravity VLTI instrument: concept, development and performance in laboratory," *Proc. SPIE* **9146**, 91461J (2014).
  17. M. Benisty, J.-P. Berger, L. Jocou, P. Labeye, F. Malbet, K. Perraut, and P. Kern, "An integrated optics beam combiner for the second generation VLTI instruments," *Astron. Astrophys.* **498**, 601–613 (2009).
  18. L. Labadie, G. Martín, N. C. Anheier, B. Arezki, H. A. Qiao, B. Bernacki, and P. Kern, "First fringes with an integrated-optics beam combiner at 10  $\mu\text{m}$  A new step towards instrument miniaturization for mid-infrared interferometry," *Astron. Astrophys.* **531**, A48 (2011).
  19. A. Rodenas, G. Martin, B. Arzeki, N. D. Psaila, G. Jose, A. Jha, L. Labadie, P. Kern, A. K. Kar, and R. R. Thomson, "Three-dimensional mid-infrared photonic circuits in chalcogenide glass," *Opt. Lett.* **37**, 392–394 (2012).
  20. S. Gross, N. Jovanovic, A. Sharp, M. Ireland, J. Lawrence, and M. J. Withford, "Low loss mid-infrared ZBLAN waveguides for future astronomical applications," *Opt. Express* **23**, 7946–7956 (2015).
  21. N. Jovanovic, P. G. Tuthill, B. Norris, S. Gross, P. Stewart, N. Charles, S. Lacour, M. Ams, J. S. Lawrence, A. Lehmann, C. Niel, J. G. Robertson, G. D. Marshall, M. Ireland, A. Fuerbach, and M. J. Withford, "Starlight demonstration of the Dragonfly instrument: an integrated photonic pupil-remapping interferometer for high-contrast imaging," *Mon. Not. R. Astron. Soc.* **427**, 806–815 (2012).
  22. G. Martín, T. Pognat, F. Gardillou, C. Cassagnettes, D. Barbier, C. Guyot, J. Hauden, E. Huby, and S. Lacour, "Novel multi-telescopes beam combiners for next generation instruments (FIRST/SUBARU)," *Proc. SPIE* **9907**, 990738 (2016).
  23. R. Errmann, S. Minardi, L. Labadie, B. Muthusubramanian, F. Dreisow, S. Nolte, and T. Pertsch, "Interferometric nulling of four channels with integrated optics," *Appl. Opt.* **54**, 7449–7454 (2015).
  24. H.-D. Kenchington Goldsmith, N. Cvetojevic, M. Ireland, P. Ma, P. Tuthill, B. Eggleton, J. S. Lawrence, S. Debbarma, B. Luther-Davies, and S. J. Madden, "Chalcogenide glass planar MIR couplers for future chip based Bracewell interferometers," *Proc. SPIE* **9907**, 990730 (2016).
  25. A. Arriola, B. Norris, N. Cvetojevic, S. Gross, J. Lawrence, M. Withford, and P. Tuthill, "First on-sky demonstration of a compact fully-integrated Photonic Waveguide Nulling Interferometer," in *Conference on Lasers and Electro-Optics, OSA Technical Digest*, paper JF2N.4.
  26. K. Itoh, W. Watanabe, S. Nolte, and C. Schaffer, "Ultrafast processes for bulk modification of transparent materials," *MRS Bulletin* **31**, 620–625 (2006).
  27. R. Gattass and E. Mazur, "Femtosecond laser micromachining in transparent materials," *Nat. Phot.* **2**, 219–225 (2008).
  28. S. Minardi, F. Dreisow, M. Gräfe, S. Nolte, and T. Pertsch, "Three-dimensional photonic component for multichannel coherence measurements," *Opt. Lett.* **37**, 3030–3032 (2012).
  29. A. Saviuk, S. Minardi, F. Dreisow, S. Nolte, and T. Pertsch, "3D-integrated optics component for astronomical spectro-interferometry," *Appl. Opt.* **52**, 4556–4565 (2013).
  30. A. Arriola, S. Mukherjee, D. Choudhury, L. Labadie, and R. R. Thomson, "Ultrafast laser inscription of mid-IR directional couplers for stellar interferometry," *Opt. Lett.* **39**, 4820–4822 (2014).
  31. J. Tepper, L. Labadie, R. Diener, S. Minardi, J.-U. Pott, R. R. Thomson, and S. Nolte, "Integrated optics prototype beam combiner for long baseline interferometry in the L and M bands," *Astron. Astrophys.* **602**, A66 (2017).
  32. A. Ymeti, J.S. Kanger, J. Greve, P.V. Lambeck, R. Wijn, and R.G. Heideman, "Realization of a multichannel integrated Young interferometer chemical sensor," *Appl. Opt.* **42**, 5649–5660 (2003).
  33. J. G. Titchener, A. S. Solntsev, and A. A. Sukhorukov, "Two-photon tomography using on-chip quantum walks," *Opt. Lett.* **41**, 4079–4082 (2016).
  34. R. J. Chapman, M. Santandrea, Z. Huang, G. Corrielli, A. Crespi, M.-H. Yung, R. Osellame, and A. Peruzzo, "Experimental perfect state transfer of an entangled photonic qubit," *Nat. Comm.* **7**, 11339 (2016).
  35. S. Minardi, and T. Pertsch, "Interferometric beam combination with discrete optics," *Opt. Lett.* **35**, 3009–3011

- (2010).
36. E. Tatulli, and J.-B. LeBouquin, "Comparison of Fourier and model-based estimators in single- mode multi-axial interferometry," *Month. Not. R. Astron. Soc.* **368**, 1159–1168 (2006).
  37. E. Tatulli, F. Millour, A. Chelli, G. Duvert, B. Acke, O. Hernandez Utrera, K.-H. Hofmann, S. Kraus, F. Malbet, P. Mége, R.G. Petrov, M. Vannier, G. Zins, P. Antonelli, U. Beckmann, Y. Bresson, M. Dugué, S. Gennari, L. Glück, P. Kern, S. Lagarde, E. Le Coarer, F. Lisi, K. Perraut, P. Puget, F. Rantakyö, S. Robbe-Dubois, A. Roussel, G. Weigelt, M. Accardo, K. Agabi, E. Altariba, B. Arezki, E. Aristidi, C. Baffa, J. Behrend, T. Blöcker, S. Bonhomme, S. Busoni, F. Cassaing, J.-M. Clausse, J. Colin, C. Connot, A. Delboulbé, A. Domiciano de Souza, T. Driebe, P. Feautrier, D. Ferruzzi, T. Forveille, E. Fossat, R. Foy, D. Fraix-Burnet, A. Gallardo, E. Giani, C. Gil, A. Glentzlin, M. Heiden, M. Heininger, D. Kamm, M. Kiekebusch, D. Le Contel, J.-M. Le Contel, T. Lesourd, B. Lopez, M. Lopez, Y. Magnard, A. Marconi, G. Mars, G. Martinot-Lagarde, P. Mathias, J.-L. Monin, D. Mouillet, D. Mourard, E. Nussbaum, K. Ohnaka, J. Pacheco, C. Perrier, Y. Rabbia, S. Rebattu, F. Reynaud, A. Richichi, A. Robini, M. Sacchetti, D. Schertl, M. Schöller, W. Solscheid, A. Spang, P. Stee, P. Stefanini, M. Tallon, I. Tallon-Bosc, D. Tasso, L. Testi, F. Vakili, O. von der Lühe, J.-C. Valtier, and N. Ventura, "Interferometric data reduction with AMBER/VLTI. Principle, estimators and illustration," *Astron. Astroph.* **464**, 29–42 (2007).
  38. W. H. Press, S. A. Teukolsky, W. T. Vetterling, B. P. Flannery, *Numerical Recipes in C++: the Art of Scientific Computing* (Cambridge, 2003).
  39. H. Yayama, S. Fujino, K. Morinaga, H. Takebe, D. W. Hewak, and D. N. Payne, "Refractive index dispersion of gallium lanthanum sulfide and oxysulfide glasses," *J. Non-Cryst. Sol.* **239**, 187–191 (1998).
  40. S. Minardi, "Nonlocality of coupling and the retrieval of field correlations with arrays of waveguides," *Phys. Rev. A* **92**, 013804 (2015).
  41. Y. Shimotsuma, P.G. Kazansky, J. Qiu, and K. Hirao, "Self-Organized Nanogratings in Glass Irradiated by Ultrashort Light Pulses," *Phys. Rev. Lett.* **91**, 247405 (2003).
  42. Y. Nasu, M. Kohtoku, and Y. Hibino, "Low-loss waveguides written with a femtosecond laser for flexible interconnection in a planar light-wave circuit," *Opt. Lett.* **30**, 723–725 (2005).
  43. M. M. Colavita, "Fringe Visibility Estimators for the Palomar Testbed Interferometer," *Publ. Astron. Soc. Pac.* **91**, 111–117 (1999).
  44. R. Diener, S. Minardi, J. Tepper, S. Nolte, and L. Labadie, "All-in-one 4-telescope beam combination with a zig-zag array of waveguides," *Proc. SPIE* **9907**, 990731 (2016).
  45. A. Glindemann *Principles of Stellar Interferometry* (Springer, 2011).

## 1. Introduction

Astronomical interferometry is a technique allowing the synthesis of extremely large, diffraction-limited virtual telescopes through the coherent combination of electromagnetic radiation collected by several separate, relatively small-size telescopes. The foundations of this technique lie in the Van Cittert-Zernike theorem, which states that the spatial coherence function of light is the Fourier transform of the angular brightness distribution of the light source [1]. Today, astronomical interferometers operating at radio [2], sub-millimeter [3], infrared [4] or visible [5] wavelengths can deliver images of astronomical objects with angular resolutions at the milliarcsecond level (1 milliarcsecond = 5 nrad). These resolution levels allow several unique science cases, such as the observation of relativistic jets ejected by accreting supermassive black holes in active galaxies [6], the observation of spots and temperature gradients on nearby giant stars [7–9] or the understanding of the inner structure of proto-planetary disks surrounding young stars [10, 11]. In the last two decades, near-infrared (1.5–2.5  $\mu\text{m}$ ) interferometry has strongly benefitted from the application of advanced photonic technologies to astronomical instrumentation (astrophotonics [12]). Since the first demonstration that high precision light coherence measurements can be achieved by combining telescopes in single mode, optical fibre couplers [13], interferometric instruments moved swiftly from optical fibre to integrated optics (IO) technology [14, 15]. Beside precision, IO technology can deliver additional calibration stability and miniaturisation of multi-telescope beam combination units. The current state-of-the-art in near-infrared interferometric astrophotonic instrumentation is represented by the GRAVITY instrument [16], which features an IO chip combining simultaneously up to 4 telescopes [17]. The success of the integrated optics approach to interferometry has motivated a few groups around the world to study the extension of integrated optics combiners to spectral bands beyond near-infrared [18–20], to implement IO reformatters for sparse aperture interferometry [21], to increase the number of combined

telescopes [22], or to include nulling capabilities in the devices [23–25]. In this context, the three-dimensional (3D) structuring capability of ultrafast laser inscription [26, 27] both enables the development of new beam combination geometries as well as components designed for optical bands ranging from visible to mid-infrared [19, 20, 28–31]. Interestingly, the progress in IO multi-channel interferometric beam combiners can also find valuable applications beyond astronomy, in particular in the field of miniaturised sensors for biophotonic [32] and quantum optics [33, 34].

Here we report the progress towards the development of multi-telescope 3D-IO beam combiners optimised for the mid-infrared band centred at a wavelength of  $3.4\mu\text{m}$  (known in astronomy as L-band). We present an experimental test of first prototypes allowing the combination of 2- and 4-telescopes based on two different architectures, namely the ABCD pairwise combiner [17] and the discrete beam combiner (DBC [35]). The experiments proved the capability of both our calibrated prototypes to retrieve precisely the amplitude of the visibility with signal to noise ratios exceeding 10 with several 100 counts per input channel and exposure. Phase could also be retrieved to a level sufficient to resolve the nonlinearity of our delay line. In the absence of an absolute photometric calibration of our cameras, we relied on numerical Monte-Carlo simulations to estimate the numerical stability of the fringe visibility retrieval algorithms for different levels of photon fluxes using the experimental and the ideal transfer matrix of the combiner. As result we could quantify the existing performance gap between the manufactured components and their ideal counterparts.

## 2. Mathematical description of interferometric beam combiners

Astronomical interferometric imaging requires a dense spatial sampling of the first order correlation function of electromagnetic fields, which is accomplished by combining pairs of (often movable) telescopes separated by a baseline. While the amplitude and phase of radio waves can be measured directly at the telescope and correlated at a later time, at optical frequencies only the measurement of the power of an interference modulation can be used to derive the field correlation functions. Because the fidelity of the reconstructed image increases with the number of sampled baselines, instruments allowing the simultaneous combination of more than two telescopes can reduce the acquisition time of the coherence function and provide snapshot images of the astronomical object. In general, simultaneous measurements of the coherence of all possible combinations of  $N$  optical fields  $\vec{E}_i = \hat{e}_i E_i$  can be accomplished by measuring the irradiance of their linear superposition:

$$P = \left\langle \left| \sum_{i=1}^N \vec{E}_i \right|^2 \right\rangle = \sum_{i=1}^N \langle |E_i|^2 \rangle + \sum_{i \neq j}^N C_{i,j} \langle E_i E_j^* \rangle = \sum_{i=1}^N \Gamma_{i,i} + 2 \sum_{i=1}^{N-1} \sum_{j=i}^N C_{i,j} \Re \Gamma_{i,j} \quad (1)$$

where  $C_{i,j} = \hat{e}_i \cdot \hat{e}_j$  takes into account the polarisation mismatch of the interfering fields (instrumental visibility) and  $\Gamma_{i,j} = \Gamma_{j,i}^* \equiv \langle E_i E_j^* \rangle$  are the mutual coherence functions (complex visibilities) [1]. In a beam combiner, the individual mutual coherence terms are in general retrieved by modulating in space or time the relative phase between the interfering fields. Irrespective of the combination technique, a multiple-field interferometric beam combiner can be described by a complex transfer matrix  $\{U\}$  relating the  $N$  input fields to  $M$  output fields. The power measured at the  $n^{\text{th}}$  output port of the device can be thus be written as:

$$\begin{aligned} P_n &= \sum_{i=1}^N \langle |U_{n,i} E_i|^2 \rangle + 2 \sum_{i=1}^{N-1} \sum_{j=i}^N C_{i,j} \Re \langle U_{n,i} E_i U_{n,j}^* E_j^* \rangle \\ &= \sum_{i=1}^N |U_{n,i}|^2 \Gamma_{i,i} + 2 \sum_{i=1}^{N-1} \sum_{j=i}^N C_{i,j} \left[ \Re(U_{n,i} U_{n,j}^*) \cdot \Re \Gamma_{i,j} - \Im(U_{n,i} U_{n,j}^*) \cdot \Im \Gamma_{i,j} \right], \quad n = 1, \dots, M \end{aligned} \quad (2)$$



We notice that the power at the outputs is a linear combination of the self-coherence functions  $\Gamma_{i,i}$  (*i.e.* the power at the input ports) and the quadratures of the mutual coherence functions (real and imaginary parts of  $\Gamma_{i,j}$ ). By arranging the coherence functions on a vector of length  $N^2$ ,

$$\vec{J} = (\Gamma_{1,1}, \dots, \Gamma_{N,N}, \Re\Gamma_{1,2}, \dots, \Re\Gamma_{N-1,N}, \Im\Gamma_{1,2}, \dots, \Im\Gamma_{N-1,N})^T, \quad (3)$$

we can write Eq. (2) as:

$$\vec{P} = \text{V2PM} \cdot \vec{J}, \quad (4)$$

where  $\vec{P} = \{P_n\}$  is the vector with the power measurements at the output ports of the combiner, and V2PM is a  $M \times N^2$  real-valued matrix known in astrointerferometry as Visibility to Pixel Matrix [36]. The V2PM is often employed to extract complex visibilities from measurements with multi-telescope interferometric instruments [37]. From Eq. (2), it is straightforward to derive that the elements of the V2PM are related to the transfer matrix of the beam combiner by [35]:

$$\begin{aligned} \text{V2PM}_{n,i} &= i_{n,i} = |U_{n,i}|^2 \quad i = 1 \dots N \\ \text{V2PM}_{n,p(i,j)} &= c_{n,p(i,j)} = 2C_{i,j} \Re(U_{n,i} U_{n,j}^*) \quad i < j \quad j = 2 \dots N \\ \text{V2PM}_{n,q(i,j)} &= s_{n,q(i,j)} = -2C_{i,j} \Im(U_{n,i} U_{n,j}^*) \quad i < j \quad j = 2 \dots N \end{aligned} \quad (5)$$

where the indices  $p(i, j)$  and  $q(i, j)$  are defined as follows:

$$p(i, j) = i + (j - 1) \cdot (j - 2)/2 + N \quad (6)$$

$$q(i, j) = i + (j - 1) \cdot (j - 2)/2 + N \cdot (N + 1)/2 \quad (7)$$

Given the  $\vec{P}$  it is possible to find a vector  $\vec{J}$  which minimise the residual  $r = |\text{V2PM} \cdot \vec{J} - \vec{P}|$ . In practice it is necessary to compute the Moore-Penrose pseudo-inverse [38] of the V2PM (also known as Pixel to Visibility Matrix or P2VM [36, 37]) and apply it to the known term  $\vec{P}$ . Notice that a meaningful solution  $\vec{J}$  exists whenever  $M \geq N^2$  (overdetermined linear system of equations). The singular value decomposition [38] of the V2PM can give a first estimate of the precision of the coherence retrieval procedure. The decomposition allows to calculate the condition number (CN) of the V2PM (defined as the ratio of the largest to the smallest singular value) which roughly gauges the noise amplification factor in the retrieval of the coherences from photometric measurements. The smaller the condition number, the more precise are the estimates of the mutual coherence functions. The V2PM elements can be used to estimate the instrumental visibility  $C_{i,j}$ . From the definition of the matrix elements (Eq. 5) it is possible to show [37] that:

$$C_{i,j}^2 = \frac{\sum_{n=1}^M (c_{n,p(i,j)}^2 + s_{n,q(i,j)}^2)}{\sum_{n=1}^M 4 \cdot (i_{n,i} i_{n,j})}. \quad (8)$$

Regarding notations, in the following we will comply to the usual astronomical custom of expressing the retrieved mutual coherence functions in terms of their normalised amplitude  $V_{i,j}$  (the Michelson fringe visibility):

$$V_{i,j} = \sqrt{\frac{(\Re\Gamma_{i,j})^2 + (\Im\Gamma_{i,j})^2}{\Gamma_{i,i}\Gamma_{j,j}}}, \quad i \neq j \quad (9)$$

and its phase  $\phi_{i,j}$ :

$$\phi_{i,j} = \tan^{-1} \frac{\Im\Gamma_{i,j}}{\Re\Gamma_{i,j}}. \quad (10)$$

### 3. Fabrication of samples

We fabricated all devices by means of ultrafast laser inscription (ULI) in Gallium Lanthanum Sulfide (GLS) glass substrates [39], a glass featuring a wide transparency window ranging from the visible to the mid-infrared (cut-off wavelength 9–10  $\mu\text{m}$ ). ULI uses tightly focused, high intensity femtosecond laser beams to induce permanent, local structural modifications in dielectric media (see [26,27] for reviews). Depending on the material and laser parameters, the laser-induced modifications can enhance [19] or depress [20] the refractive index of the irradiated dielectric medium allowing the structuring of photonic devices (such as waveguides, and couplers) in three dimensions (3D). From the viewpoint of our application, the 3D capabilities are essential to avoid losses and cross-talk from waveguide crossover in pairwise ABCD combiners or to enable the beam combination capability in arrays of coupled waveguides ([40], see also below).

The ULI setup is based on an amplified Yb:KGW laser (PHAROS, Light Conversion) emitting 200 fs pulses at a wavelength of 1026 nm with a settable repetition rates up to 1 MHz. The setup includes a rotatable  $\lambda/2$ -plate and a linear polariser for precise tuning the laser power. The formation of nano-gratings [41] is avoided by converting the beam polarisation to circular with a  $\lambda/4$ -plate just before being focused in the substrate with a NA = 0.35 microscope objective. The substrate is placed on a movable 3-axis nano-positioning stage. We wrote the components using laser parameters and translation speed which could induce positive variation of the refractive index of GLS, so that laser irradiation affected the core of the waveguides only. Writing parameters were optimised in order to obtain single mode waveguides featuring nearly circular propagating modes at a wavelength of 3.4  $\mu\text{m}$  (18.6  $\mu\text{m} \times 21.7 \mu\text{m}$  mode field diameter) with a propagation loss of  $0.9 \pm 0.3$  dB/cm (measured directly with cut back method). The waveguides exhibit a rectangular cross section (9.4  $\mu\text{m} \times 24.8 \mu\text{m}$ ) and were manufactured by multipass writing [42] with 21 lines separated by 300 nm and the following laser settings: pulse length 500 fs, repetition rate 500 kHz, laser power 40 mW and speed 1 mm/s.

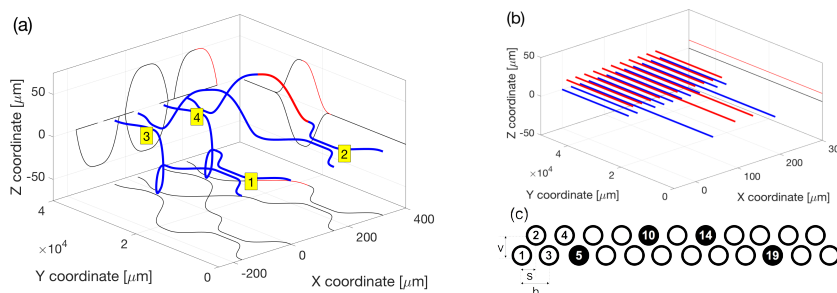


Fig. 1. Scheme of the 3D beam combiners tested in the experiments. (a) 2-telescope ABCD combiner with cross-over avoidance by 3D displacement of the waveguide path. Red path: region of the taper for insertion of a  $\pi/2$  phase delay. Numbers on yellow background indicate the 4 couplers of the ABCD combiner. (b) 4-telescope discrete beam combiner featuring 23 straight coupled waveguides arranged in a zig-zag lattice geometry. The two interlaced layers are highlighted by the blue (lower array) and the red colors (upper array). (c) Transverse view of the zig-zag array indicating the numbering convention, the geometric parameters, and the input waveguides (in black).

#### 3.1. 2-telescope ABCD combiner

In asterointerferometry the term ‘ABCD beam combination’ stands for a 4-levels phase shifting interferometry method to determine unambiguously the phase of an interference pattern [43]. In

practice, the spatial or temporal fringe is sampled at 4 equidistant phases separated by  $\pi/2$ . An implementation with integrated optics of the ABCD combination scheme is at the basis of the GRAVITY beam combiner [16] and consist on a 2-level construction of waveguide splitters and combiners [17]. At the first level, each of the two input waveguides are split in two. At the second level, pairs of waveguides (each originating from a different input waveguide) are combined in 2x2 directional couplers providing pairs of outputs which sample the fringe in phase opposition. To achieve the ABCD sampling, a section of waveguide with modified propagation constant is inserted in one of the waveguides feeding one of the output 2x2 couplers in order to introduce a  $\pi/2$  phase shift between the combined fields. The realisation of this component with planar IO technology necessarily requires a waveguide X-crossing, which contributes to the cross-talk between the  $M = 4$  output channels.

Our intention was to manufacture a component exploiting the capability of ULI to write waveguides in 3D and avoid the X-crossing. A sketch of the device is illustrated in Fig. 1(a). The design of the splitters at the first level (indicated by 1 and 2 in Fig. 1(a)) is based on the template of the 2x2 directional coupler we recently developed in GLS glass [31], which has an interaction length of 4 mm, a gap of  $20.5 \mu\text{m}$  and features  $75 \mu\text{m}$ -high raised-sine s-bend waveguides of 7 mm length for the input and output waveguides. For test convenience we retained the two inputs waveguide of each of the couplers at the first level. The outputs of the first level of couplers were bended in the x-dimension to address the inputs of couplers 3 and 4 at the second level (maximal elongation  $150 \mu\text{m}$ , total length 14 mm). The X-crossing of the waveguides was avoided by an additional  $50 \mu\text{m}$ -high double raised-sine s-bend in the z-dimension. To preserve the optical path difference at the input of the couplers at the second level both output waveguides of coupler 1 have a negative z-displacement, while the output waveguides of coupler 2 have a positive z-displacement. The  $\pi/2$  phase delay was introduced on one output waveguide of coupler 1 by a local increase of the writing speed (red segment in Fig. 1(a)). According to our measurements on single waveguides, an increase of the writing speed corresponds to a decrease of the propagation constant of the waveguide, so that a phase shift can be engineered between waveguides of equal geometrical path but different writing speeds. In our samples the writing speed was raised gradually from 1 mm/s to 1.4 mm/s over a 2.5-mm-long section, kept constant for another 1.2 mm and then decreased back to 1 mm/s within the final 2.5 mm. The gradual transition was necessary to avoid transition losses at the ends of the waveguide patch written at higher speed. While the design is not yet optimised, we mention that all s-bends had radii of curvature larger than 26 mm, in order to ensure losses below 1 dB per s-bend [31]. From independent measurements on straight and bended waveguides we estimated the losses of the manufactured ABCD combiner in about 6 dB (3.6 dB propagation losses and 2.4 dB from s-bends).

### 3.2. 4-telescope discrete beam combiner

Discrete beam combiners (DBC, [35]) are arrays of evanescently coupled waveguides (photonic lattices) designed to measure interferometric observables. A sufficient condition for the array to operate as an interferometric beam combiner is the presence of coupling between waveguides beyond the nearest neighbour [40]. This long-range coupling can be engineered by arranging the waveguides on a two-dimensional lattice. Three-telescope DBC featuring square lattice arrangements were manufactured and tested with monochromatic light [28] at visible wavelength. By a suitable dispersion of the output channels, the operation with polychromatic light was also proofed for applications in low-resolution spectro-interferometry [29]. We recently devised the zig-zag lattice geometry (Fig. 1(b) and (c)) as a way to satisfy at the same time the requirements of long-range coupling and the possible use of the device for high-resolution spectro-interferometry [44]. Two interlaced linear arrays featuring a total of  $M = 23$ , 25-mm-long straight waveguides are used for the purpose of beam combination. With reference to Fig.1(c), the horizontal core-

to-core separation of the waveguide is  $h = 21\ \mu\text{m}$ . The linear arrays are separated vertically by  $v = 10.8\ \mu\text{m}$  and shifted horizontally by  $s=h/2=10.5\ \mu\text{m}$ . Four 25-mm-long input waveguides were added to the waveguide array at the positions 5, 10, 14, 19 (black cores in Fig. 1(c)) to ensure the excitation of individual waveguides of the array. Because the ULI induces stress fields in the area surrounding each waveguide and leads to refractive index variations of at least  $2 \cdot 10^{-5}$  [44], we improved the uniformity of coupling across the array by increasing the inscription velocity linearly with the waveguide number at a rate of  $+0.075\ \text{mm/s}$  per waveguide. We found experimentally that this correction improves the symmetry of the discrete diffraction patterns excited by symmetrically positioned input waveguides and additionally reduces the polarisation dependence of the output field. A possible explanation of the effect of this writing protocol is that it compensates for the additional refractive index change due to the long range stress field induced by ULI.

The estimated losses of the DBC combiner are essentially propagation losses and amount to 4.5 dB.

#### 4. Calibration and monochromatic interferometric test of the beam combiners

The test of the components consisted in calibrating initially their monochromatic V2PM and then use the P2VM to retrieve interferometric observables (quadratures and phase of the normalised coherence functions) from video recordings of the light distribution at the output of the components excited by pairs of phase-modulated optical fields.

The calibration of the V2PM follows the method discussed in Ref. [29] and consists in recording the photometry of the output channels of the device for single beam and twin-beam excitation. As can be inferred from Eq. (5), the normalised photometry with single beam excitation of the inputs of the device consists in the first  $N$  columns of the V2PM. The determination of the remaining columns is accomplished by recording the time varying photometry of all possible  $N \cdot (N - 1)/2$  input field combinations, which are modulated in phase through a delay line traveling at constant speed. The phase modulation induces sinusoidal oscillations at the  $M$  outputs ( $M = 4$  for the 2-telescope ABCD,  $M = 23$  for the 4-telescope DBC) of the component whose normalised amplitude and phase are projected onto quadratures, corresponding to the following  $N \cdot (N - 1)$  columns of the V2PM. To improve the precision of the calibration, the raw photometric data were electronically filtered with a moving average to remove a high frequency electronic noise which artificially raises the visibility of the fringes [31].

The acquisition of the dataset with twin-beam input excitation is performed with a Michelson interferometer. A suitably collimated 3.39 nm He-Ne laser beam is split into two beams which are focused by a lens onto separate input waveguides of the components by slightly tilting one beam respect to the other. A computer-controlled, motorised delay line was used in one arm of the interferometer to introduce a controllable phase delay between the inputs. The minimal incremental delay of the stepping-motor is 100 nm (corresponding to a phase of 0.18 radians at  $\lambda = 3.39\ \mu\text{m}$ ) and a positioning accuracy of 0.5%. The samples were mounted on a multi-axis positioning stage and their outputs imaged with a suitable dioptric system onto an InSb mid-infrared camera (measured noise level  $\sim 7$  counts rms).

To test the numerical stability of the algorithm retrieving the interferometric quantities, we derived the P2VM from the experimentally determined V2PM and applied it to the calibration dataset. These measurements allowed us to estimate the standard deviation of the retrieved visibility and phase. From the average visibility  $\bar{V}$  and its standard deviation  $\sigma_V$  we estimated experimentally the signal to noise ratio of the visibility amplitude as  $\text{SNR} = \bar{V}/\sigma_V$ .

##### 4.1. Retrieval of visibility and phase with the 2-telescope ABCD combiner

An insight on the characteristics of the ABCD beam combiner is given by the plots in Figs. 2(a) and 2(b), which represent the calibrated and ideal V2PM respectively. For single beam

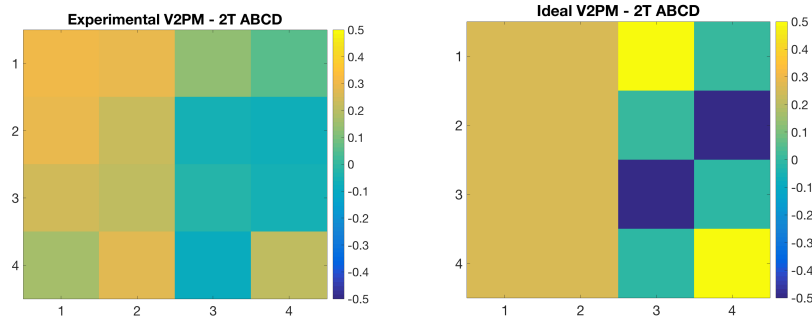


Fig. 2. False color representation of the experimental (a) and ideal (b) V2PM matrix of the 2-telescope ABCD beam combiner unit.

excitation the distribution of the light among the 4 outputs of the manufactured component is rather uniform, as indicated by the first two columns of the V2PM. The pattern of the last two columns of the experimental V2PM resembles the ideal. The amplitudes of the experimental pattern are smaller than the ideal due to a low instrumental visibility, which was measured to be  $C_{1,2} = 0.30$ . Such a low instrumental visibility is most probably originating from long range stress birefringence induced by ULI. From the last two columns of the experimental V2PM the phase delay induced by the phase-shifter of the ABCD combiner can be measured, as the matrix elements are proportional to the quadratures of the cross-products of the field transfer function of the combiner (see Eq.(5)). The measured phase shift is 2.2 rad, which is about 0.6 radian more than the optimal delay value.

Direct application of the calibrated P2VM on the dataset allows to retrieve a visibility  $V_{1,2} = 0.92 \pm 0.06$ , which is compatible with the expected visibility of our laser source ( $V_{1,2} = 1$ ). However, because the first two columns of the experimental V2PM have nearly equal elements, the condition number of the matrix is very high ( $\sim 65$ , the ideal V2PM is in fact singular for a 2T-ABCD combiner) and an improved retrieval of the visibility can be obtained by measuring independently the transmitted power of the individual beam and splitting the retrieval algorithm in two steps involving the use of two sub-matrices of the V2PM (see Ref. [37] for details). Figure 2 shows the results of the latter retrieval algorithm for the 2-telescope ABCD combination unit. The retrieved quadratures of the normalised visibility function (Fig. 3(a)) are distributed over a circle of average radius  $V_{1,2} = 0.96 \pm 0.034$  (visibility signal to noise ratio of 28). The linear phase ramp between the two input fields (Fig. 3(b)) is measured correctly with a standard deviation of the residuals of  $\sigma = 0.20$  rad, a value which can mostly be accounted for by the nonlinearity of the delay line (expected maximal deviation over the shown range  $< 0.4$  rad). The average transmitted power of the two input beams were measured in  $\sim 2500$  and  $\sim 1300$  counts per frame, respectively.

#### 4.2. Retrieval of visibility and phase with the 4-telescope DBC

We used the calibrated V2PM of the 4-telescope DBC (not shown) to estimate the instrumental visibility of for each baseline and found values ranging from 0.868 to 0.943 depending on the combined fields. These values are much higher than the values reported for the ABCD combiner possibly indicating a more balanced distribution of the stress birefringence in the DBC (see Table 1).

The relatively low condition number of the V2PM ( $\sim 14$ ) allowed us to retrieve the coherence functions applying directly the P2VM to a set of unfiltered photometric data for the pairwise

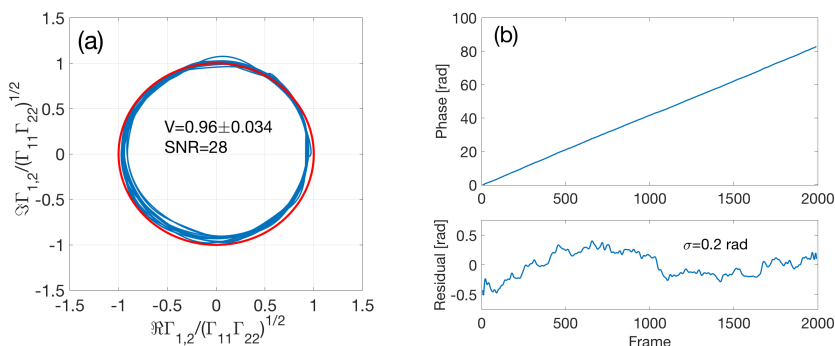


Fig. 3. Experimental estimate of the retrieval precision of interferometric quantities for a 2-telescope ABCD combination unit. (a) plot of the the retrieved normalised quadratures of the coherence function (blue) as compared to the expected values (red circle). (b, Top) Retrieved unwrapped phase difference between the input fields and their deviation from linearity (b, Bottom) as a function of time-consecutive frames.

Table 1. Instrumental visibilities for the baselines of the 4-telescope DBC as estimated from its calibrated V2PM.

$C_{1,2}$	$C_{1,3}$	$C_{1,4}$	$C_{2,3}$	$C_{2,4}$	$C_{3,4}$
0.868	0.878	0.899	0.943	0.875	0.875

excitation of the 4-telescope DBC. The quadratures of the normalised complex visibility and its phase are reported in Figs. 4 and 5. The experimental data are all scattered around circles of radius  $V_{i,j} = 0.96 - 1.04$  depending on the chosen pair of inputs with a standard deviation compatible with the hypothesis of unitary coherence of the input laser beams. The SNR of the visibility measurement varies from 12 to 25. The linear phase ramp is also retrieved correctly with a standard deviation from linearity ranging from  $\sigma = 0.13$  to  $\sigma = 0.17$  (corresponding to  $\lambda/48$  and  $\lambda/36$ , respectively), showing that the phase retrieval algorithm can reach a precision sufficient to measure the nonlinearities of the delay line (expected maximal deviation over the shown range  $< 0.2$ rad). The measured transmitted power for each input beam is about 1200 counts per frame.

## 5. Discussion of the results and outlook

The presented data show that the manufactured IO beam combiners can already be calibrated to retrieve precisely visibility and phase on pairs of monochromatic, mid-infrared excitation beams. However, because the absolute photon flux could not be calibrated in the experiments, we evaluated by means of a Monte Carlo simulation the relative performance of the calibrated combiners respect to the ideal V2PM of the ABCD and DBC architectures. The simulation tests the numerical stability of the retrieval algorithm by emulating the experimental determination of the signal-to-noise ratio of the amplitude of the fringe visibility for fully coherent input fields ( $V = 1$ ). We created a statistical ensemble of 10000 synthetic photometric measurements by application of the V2PM (experimental or ideal) to an input consisting of fields of constant amplitude (equal for all combined telescopes and corresponding to the the detected photon number per telescope and exposure) and random phase. A random number with variance equal to the number of measured photons was added to the synthetic photometric data to simulate the

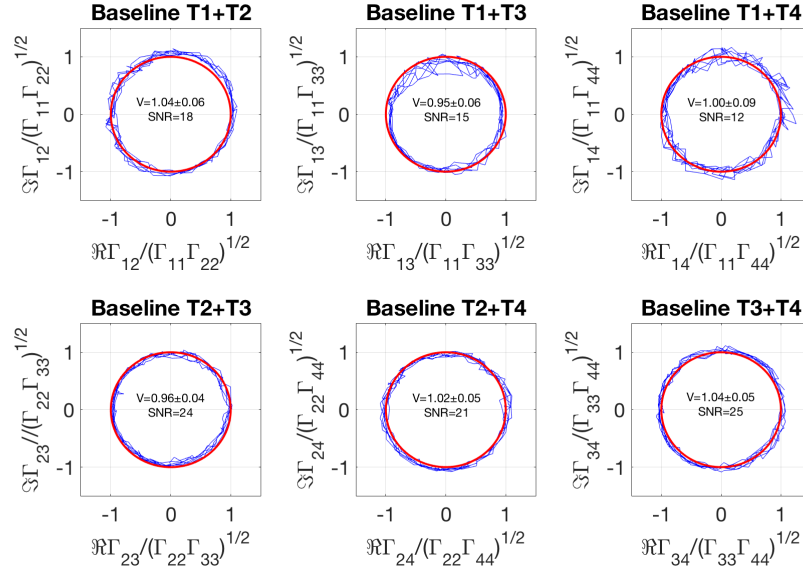


Fig. 4. Experimentally retrieved quadratures of the complex visibility function for the 4-telescope DBC for all possible combinations of the input beams. The individual input sites are indicated with T followed by a number. As in Fig. 3, the red circle indicated the expected distribution of the quadratures for fully coherent interfering fields.

photon shot noise in the photon-rich measurement regime. The visibility amplitude (Eq. 9) for each noise realisation was then calculated from the application of the P2VM to the synthetic photometric data and the SNR estimated from the average value and standard deviation of the ensemble.

Figure 6 illustrates the results of the simulations for the 2-telescope ABCD combiner (Fig. 6(a)) and the 4-telescope DBC (Fig. 6(b)). The blue lines represent the expected SNR for the ideal combiner, while the red lines represent the results obtained by using the experimentally measured V2PM. The multiple lines appearing in the DBC simulation correspond to different input combinations (baselines), which represents a peculiar feature of the DBC architecture. This feature can be exploited to equalise the SNR of the coherence measurements in arrays featuring telescopes of different diameter (such as the Very Large Telescope Interferometer) by connecting the larger telescopes to the baselines featuring lower SNR. The comparison between the red and blue lines show that the manufactured components are not yet optimal. The ideal combiners have a SNR higher by a factor 3.6 and 1.7 than the experimental 2-telescope ABCD combiner and the 4-telescope DBC, respectively. Because the SNR scales as the square root of the detected photon number, the amelioration of the matching (at constant throughput) between the ideal and real component by improved manufacturing process could deliver devices with a better sensitivity evaluated at the level of +2.8 and +1.1 astronomical magnitudes for the ABCD and the DBC, respectively. Since the calibration data had a large signal-to-noise ratio, our understanding is that the gap in sensitivity between the experimental and the ideal combiner mainly reside in the departure of the transfer function of the manufactured combiners respect to the ideal one.

Regarding the relative sensitivity of the chosen architectures, the fact that for fixed number of photons the ABCD combiners show higher SNR than DBC is mostly due to the fact that the

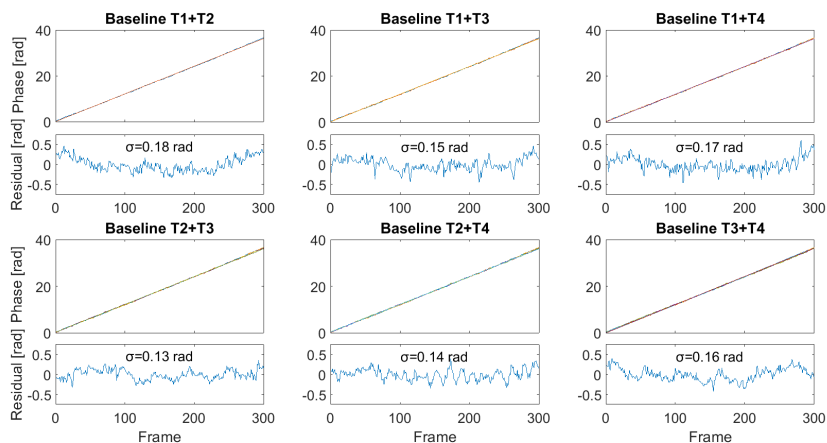


Fig. 5. Experimentally retrieved linear phase ramps for the 4-telescope DBC for all 6 possible combinations of the input fields (baselines). The residual of a linear fit are also plot as a function of time, here given in number of consecutive frames. The standard deviation of the phase residual are indicated for each baseline.

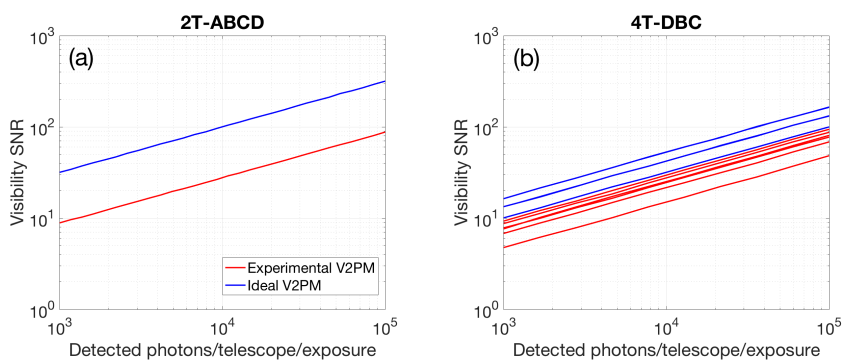


Fig. 6. Results of a Monte-Carlo simulation of the performance of the manufactured (red) and ideal (blue) beam combiners in the presence of photon shot noise (see details in the text). The signal-to-noise ratio of the retrieved visibility amplitude is plotted against the detected number of photons per input channel and exposure for the 2-telescope ABCD combiner (a) and the 4-telescope DBC (b). A feature of the DBC is that different baselines feature different sensitivities, as can be seen by the many lines of the same color in the plot.

number of combined fields is different. In fact, because multi-telescope beam combiners have to split the  $N$  input light fluxes on more output channels, the signal-to-noise ratio of the visibility scales as  $\propto \sqrt{I_0/N}$ ,  $I_0$  being the input detected flux per telescope [45]. Taking this scaling into account and assuming the same throughput for the two chips our conclusion is that both manufactured chips have comparable sensitivity (SNR $\sim$ 60 for  $10^5$  detected photons/telescope/exposure). However, in the current implementation, the ABCD combiner is penalised by the bend losses which reduce the throughput respect to the DBC combiner by an estimated 1.5 dB.

Because simulations indicate that there is room for improvement, we are currently working on the optimisation of the manufacturing process to obtain better components. In particular, we are



targeting the reduction of the bend losses and improvement of the instrumental visibility of the ABCD combiner which are required before starting the development of more complex combiners allowing the combination of 4 or more telescopes with ABCD architecture. The measurement of throughput and characterisation of the samples with polychromatic light with simultaneous multi-field excitation is also foreseen in the near future. These additional data will allow us to understand the advantages of one architecture respect to the other and establish (e.g.) the trade-off between combination efficiency and effective throughput of the components.

In conclusion, we believe that the presented results provide a significant step forward towards the extension to the mid-infrared bands of integrated optics multi-channel beam combiners for astronomical interferometry, besides representing a first attempt to compare the performance of real IO beam combiners manufactured with different architectures but utilising the same technology platform and substrate material.

### **Funding**

German Federal Ministry of Education and Research (BMBF) (05A14SJA, 03Z1H534).

### **Acknowledgments**

RD, JT, LL and SM acknowledge the support of the German Federal Ministry of Education and Research (BMBF) through the project ALSI (05A14SJA). TP and SN acknowledge the support of the BMBF through the project AstroOptics (03Z1H534).

## Conclusion & Perspective

In this thesis, I have experimentally demonstrated the capabilities of ULI integrated optics (IO) for interferometric beam combination in the mid-IR. In the following paragraph, I will only briefly summarize the key outcomes of this work as more detailed summaries of all individual results can be found in the respective publications. On the basis of these findings, I will discuss the way towards a four-telescope beam combiner and a science-qualified interferometric instrument and mention ongoing and future instrumental projects where this work can contribute to.

In [Tepper et al. \(2017a\)](#) and [Tepper et al. \(2017b\)](#), I tested two different IO platforms using different inscription techniques for two-telescope couplers, positive writing in GLS and depressed writing in ZBLAN, and assessed their critical properties for astronomical applications such as transmission, splitting ratio, modal behavior and polarization properties. It turned out that both platforms are suitable for on-chip beam combination. Most notably, both platforms are capable of producing high interferometric contrasts of over 93% over a broad spectral width with  $\Delta\lambda/\lambda > 0.1$ . This marks a critical leap forward as it demonstrated for the first time that IO in the mid-IR can in fact be used for broadband interferometric combination. However, the extension to the combination of four telescopes, which is the ultimate ambition, is not trivial and requires different types of beam combining designs. In [Diener et al. \(2017\)](#), a two-telescope ABCD combiner, which is the building block of the four-telescope ABCD, and a four-telescope zig zag array were tested using monochromatic light at  $3.39\ \mu\text{m}$ . It is demonstrated that after calibration of the IO chips, the interferometric contrasts between the input light fields could be retrieved from the output channels. Yet, due to the higher number of bendings in the chip, large losses inside the ABCD chip were evidenced which complicates the readout of the output channels and decreases the overall throughput and instrumental contrast to only 30%. While the zig-zag array demonstrated contrasts of 90%, further testing using broadband light is critical as chromatic behavior is expected due to the longer interaction lengths. The measured instrumental contrasts of all platforms tested in this thesis are summarized in Table 7.1.

Platform	3.39 $\mu\text{m}$	L band	L' band	M band
2T GLS 2 $\times$ 2	98.0%	94.9%	n.a.	92.1%
2T ZBLAN 2 $\times$ 2	n.a.	93.0%	93.5%	n.a.
2T GLS ABCD	30%	n.a.	n.a.	n.a.
4T GLS zig-zag	90%	n.a.	n.a.	n.a.

Table 7.1: Measured instrumental contrasts for different two- and four-telescope combiners and wavelength ranges.

In the following, I want to outline the future of this project, subdivided in the short, mid and long-term actions.

### Immediate future: Identifying the optimal 4T combiner

Thinking towards a future four-telescope beam combiner chip, two major questions arise in the view of the results obtained in this theses: which material is the most suitable, GLS or ZBLAN? And, which layout is the optimal one, i.e. shows a high transmission and high contrast, the all-in-one, ABCD or zig-zag scheme (see Fig. 3.4 bottom)? In the following, I will propose three potential routes.

- Although the ZBLAN chips have shown a much higher throughput of 58% (compared to 25% in GLS), no 3D architectures have been demonstrated yet. Therefore, at this stage, I believe that the ZBLAN depressed writing approach would be suitable for the all-in-one coupler which is the most simple, planar design. Also, in the ZBLAN chip in [Tepper et al. \(2017b\)](#), the two waveguides overlap and as such already resemble the all-in-one approach. Furthermore, in the negative writing approach only the region outside of the core is affected. Since the all-in-one approach does not rely on evanescent fields, the photons would mostly be confined to laser-affected regions. As the all-in-one approach resembles the tested two-telescope in [Tepper et al. \(2017b\)](#) in terms of waveguide bends, one can assume similar propagation and bending losses. If Fresnel losses are removed by a perfect AR coating, this translates into 63% for the two-telescope combiner. On the other hand, the four-telescope all-in-one design contains two Y Junctions which each inherently radiate out 50% of the flux. Taking into account the two Y-Junctions in the four-telescope combiner, each with a loss of 50%, the 63% is reduced to about 15%. In addition, the all-in-one architecture needs additional photometric channels to be inscribed in order to measure the visibility correctly<sup>1</sup>(c.f. Eq. 2.5). Depending on how much flux is used to obtain the photometries, the throughput will be further reduced towards 10%. On the positive side, this design consists of junctions whose splitting ratio is achromatic and is presumably insensitive to the polarization due to the symmetric nature of the junction. Therefore, a high interferometric contrast using a rather simple design can be achieved at the cost of an overall low throughput. Nevertheless, it may be fruitful to also test the negative writing for 3D architectures in the long run as negligible bending losses were evidenced in [Tepper et al. \(2017b\)](#) which may make it suitable for more complex designs. It should be kept in

<sup>1</sup>Note that, additional photometric channels are not needed for the four-telescope ABCD or zig-zag combiner as the photometries can be reconstructed from the interferometric outputs due to a redundant number of output channels.

mind though that ZBLAN does not transmit beyond 5-6  $\mu\text{m}$  and is therefore not suitable for the astronomical N band.

- The two-telescope ABCD chip in GLS demonstrated the proof-of-concept but showed strong leakage and little instrumental contrast. Extending to a four-telescope ABCD with an assumed total length of 10 cm, this would further increase losses and would not transmit more than 5% (taking into account the measured values of bending and propagation losses [Tepper et al. 2017a](#)) which is impractical to astronomical applications. Therefore, the necessary action to put forward is the decrease of the bending losses, presumably by increasing the field confinement through a larger  $\Delta n$ . According to Thomas Gretzinger<sup>2</sup>, who recently visited our lab, propagation losses as low as  $0.22 \pm 0.2$  dB/cm and relatively high refractive index changes of about  $10^{-2}$ , compared to  $3 \cdot 10^{-3}$  in [Tepper et al. \(2017a\)](#), can be achieved in GLS by choosing another set of inscription parameters. Therefore, we are currently having a 20 mm long two-telescope ABCD prototype combiner with presumably negligible bend losses designed and manufactured at Macquarie University. This would result in a transmission of 73% taking into account coupling losses and assuming a perfect AR coating. For a four-telescope beam combiner, the sample would increase in length. However, due to the low propagation losses, even a sample of 10 cm length would show a competitive throughput of 50%. First tests will be carried out by the end of 2017/beginning of 2018.
- The GLS zig-zag array is a promising route as it only consists of parallel waveguides which minimizes bend losses and leakage and could demonstrate instrumental contrasts of about 90% at 3.39  $\mu\text{m}$ . However, this device has only been tested with monochromatic light albeit the large interaction lengths between the waveguides suggests a strong chromatic behavior of the V2PM. Yet, by dispersing the signal after the output, the V2PM can be calibrated for each wavelength ([Saviuk et al. 2013](#)). For a stable retrieval of the visibilities in the case of zig-zag array, it is important that the numerical algorithm that relates the pixels to the visibility is stable, i.e. the condition number of the V2PM is low. While this can be tailored for a certain wavelength, it is not clear how much the condition number will vary in the spectral channels. As there are still many unknown about the broadband operation of the zig-zag array, I am planning to test the zig-zag array in Cologne using a recently acquired supercontinuum source which will provide enough flux to quantify the wavelength dependence of the coupling between the waveguides, i.e. the wavelength dependence of the V2PM.

To summarize, I value the following three routes towards a four-telescope combiner as the most promising: zig-zag array in GLS manufactured at the University of Jena (ongoing, broadband characterization missing), four-telescope ABCD in GLS manufactured at Macquarie University (initiated) and the all-in-one approach in ZBLAN presumably manufactured at Macquarie University as well (not yet initiated). The testing of a four-telescope beam combiner for the simultaneous injection of four beams also requires an update of the two-beam injection testbench. The proposed layout is shown in Fig. 7.1.

An issue that has not been addressed in the publications in this thesis is the repeatability. In all publications, a series of couplers were inscribed with different parameters from which the optimal one was identified. However, it is not said that such a coupler can be readily

---

<sup>2</sup>PhD student at Macquarie University

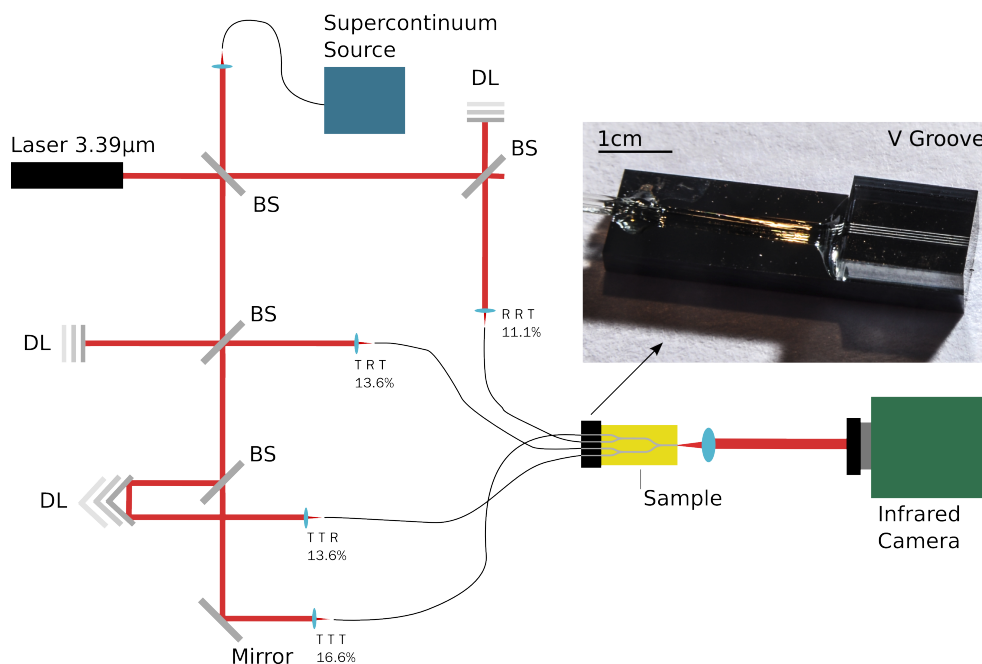


Figure 7.1: The planned final four-telescope optical testbench. Two sources of light are available, a HeNe laser at  $3.39\ \mu\text{m}$  and a supercontinuum source which ensures high-power flux from  $0.8$  to  $4\ \mu\text{m}$ . The beamsplitters are considered to be Pellicles, i.e. very thin splitters to avoid differential dispersion, with a 45/55 splitting ratio as they are available from Thorlabs. The respective optical paths differences can be scanned by individual delay lines. The individual beams are injected into single-mode fibers which are connected to the IO, here the all-in-one chip, by a V Groove. The inset shows a prototype V Groove manufactured by OZ Optics. The numbers at the fiber inputs denote the relative intensity of the broadband output due to reflection (R) and transmission (T) of the beamsplitter.

replicated by applying the same inscription parameters. In fact, repetitious inscription has shown that the splitting ratio varies by 5-10% despite the same chosen parameters. This may be due to uncontrolled fluctuations in the inscription laser power and/or different amounts of imperfections in the substrate<sup>3</sup>. The repeatability is of particular importance for the ABCD coupler as it contains many individual coupler which are ideally identical. A departure from the ideal design, can be calibrated in IO but results typically in a lower interferometric signal due to unbalanced photometries.

## Mid-term actions

In order to connect the final IO chip to the telescope beams, the instrument should provide a fixed fiber-fed interface, i.e. connecting the four input beams to the IO via mid-IR fibers. This is necessary as the waveguides into which the telescope beams will be injected can be as close as  $100\ \mu\text{m}$  to each other or even closer in the case of the zig-zag array. In order to ensure a stable injection without time-dependent cross-talk at the injection spot, fiber routing is required. Also, as the fiber inputs can be spatially arranged, a convenient coupling of the

<sup>3</sup>In fact, a higher number of defects may serve as seed electrons for avalanche photoionization and increase the level of structural modification.

telescope beams to the IO is ensured. Of course, what has been discussed in Sec. 3.4, i.e. differential dispersion and birefringence, also applies to the fibers. Therefore, the contrast can be degraded if the fibers are not equal in length, refractive index and/or show crosstalk between the polarizations. Additionally, the fiber-IO interface is not trivial as it requires micrometer precision alignment of the fiber cores with respect to the IO waveguides. While this is a standard procedure for telecom wavelength components, only a few, if any, companies can provide such services in the mid-IR. To this end, I am currently in contact with a French company specialized in the mid-IR, Le Verre Fluoré, which offers polarization maintaining fibers together with an arrayed connector that could be connected to the IO chip. While the propagation losses of fibers are negligible over distances less than one meter, the waveguide-fiber interface may reduce the overall transmission due to a mismatch of the waveguide and fiber mode. Typically, commercially available single-mode fibers have core sizes of about  $9\ \mu\text{m}$  which translates into a mode-field diameter (MFD) of  $15\ \mu\text{m}$ , which is smaller than the oval MFD of the waveguides measured in [Tepper et al. \(2017a\)](#) with  $16.3\ \mu\text{m}$  horizontally and  $24.8\ \mu\text{m}$  vertically. While this is not critical for a proof-of-concept test, the final instrument will need tapered waveguides or fibers to minimize the coupling losses. Also, a suitable optical glue at the interface will be needed in order to avoid an air gap and Fresnel losses between the fiber and waveguide. One prototype V Groove was assembled by the Canadian company OZ Optics, as shown in Fig. 7.1, but was not fully functional as one of the brittle channels broke.

So far, this work has relied on an iterative feedback between the external production of the samples in Jena or Sydney and the subsequent characterization in Cologne. However, proximity of the fabrication and testing facilities would accelerate the communication and learning process since production and characterization could be performed door-to-door. Therefore, the local implementation of a ULI facility is considered. Also, an in-house ULI setup would make us more independent of our collaborators and would strengthen the position of the institute in the astrophotonics community. In fact, such a facility may turn out to be crucial in the long term as our current collaborators cannot guarantee the steady production of ULI chips to our needs.

## Long-term future: Potential involvements in instrumental projects

Eventually, this work needs to be embedded in a larger project for the chips to be implemented at the telescope site in a science-qualified instrument. The IO combiners characterized in this thesis are, however, not directly developed for a certain telescope site or instrument.

Naturally, a four-telescope beam combiner would suit the capabilities of the four telescopes at the Very Large Telescope Interferometer (VLTI). In fact, the recently started Hi-5 project<sup>4</sup> aims at an IO based interferometric instrument for the VLTI working in the L, L' and M bands with the overall aim of high-resolution studies of planetary systems and active galactic nuclei. While Hi-5 is currently in a two-year conceptual study, it is clear that a four-telescope beam combiner will be one of its core parts that may be developed in Cologne.

The ambitious planet formation imager (PFI) project ([Monnier et al. 2016](#)) aims at about twenty individual apertures with baselines of up to 10 km. It is clear that such an undertaking requires progressive beam combination concepts to read out all pairwise interferometric

---

<sup>4</sup><http://www.biosignatures.ulg.ac.be/hi-5/index.html>

signals. Such a study was carried out in [Minardi et al. \(2016\)](#) and showed that pairwise ABCD schemes and discrete beam combiner (such as the zig-zag array) are more sensitive than multi-axial all-in-one solutions. This points towards IO based beam combiners. In particular, the advantage of the 3D capabilities of ULI as opposed to lithography for the inscription of waveguides become even more important for such a high number of telescopes as the number of undesired waveguide crossovers would strongly increase in planar structures.

As pointed out in Sec. 1.2, IO are the ideal solution to a space based interferometer mission as they do not need maintenance and are low in mass and size. Due to the absence of atmospheric absorption, GLS based IO would be particularly beneficial as they could be used to route and combine light from 1 to 10  $\mu\text{m}$ . While currently no space-based interferometric missions are planned, efforts towards a photonics based space mission are carried out. The PicSat mission ([Nowak et al. 2016](#)) is devoted to observe the transit of the giant planet  $\beta$  Pictoris using a 2 kg nanosatellite that is equipped with a 3.5 cm aperture injecting light into a single-mode fiber, which is then detected by an avalanche photodiode. This is a first step towards photonic miniaturization in space. Together with the rise of miniaturized IO devices in astronomical instrumentation in general ([Yerolatsitis et al. 2017](#); [Gatkine et al. 2017](#)), this may pave the way towards lightweight integrated nanosatellite missions.

To summarize, this work has demonstrated the successful operation of IO for beam combination in the mid-IR and demonstrated the feasibility of a four-telescope beam combiner. In the view of the previously mentioned projects, I see great potential for mid-IR IO to make a significant contribution to the core technology of future ground- and space-based observatories in general and interferometers in particular.

## Bibliography

- Adam, J.-L., Calvez, L., Trolès, J., & Nazabal, V. 2015, *International Journal of Applied Glass Science*, 6, 287
- ALMA Partnership, Brogan, C. L., Pérez, L. M., et al. 2015, *ApJ*, 808, L3
- Antonucci, R. 1993, *ARA&A*, 31, 473
- Armitage, P. 2010, *Astrophysics of Planet Formation* (Cambridge University Press)
- Arriola, A., Gross, S., Ams, M., et al. 2017, *Opt. Mater. Express*, 7, 698
- Arriola, A., Mukherjee, S., Choudhury, D., Labadie, L., & Thomson, R. R. 2014, *Optics Letters*, 39, 4820
- Baudet, E., Gutierrez-Arroyo, A., Baillieul, M., et al. 2017, *Advanced Device Materials*, 3, 23
- Benisty, M., Berger, J.-P., Jocu, L., et al. 2009, *A&A*, 498, 601
- Beresna, M., Gecevičius, M., & Kazansky, P. G. 2014, *Adv. Opt. Photon.*, 6, 293
- Burtscher, L. & Tristram, K. R. W. 2013, *The Messenger*, 154, 62
- Buscher, D., Baron, F., & Haniff, C. 2009, *Publications of the Astronomical Society of the Pacific*, 121, 45
- Buscher, D. F. 2015, *Practical Optical Interferometry* (Cambridge University Press)
- Carrasco-González, C., Henning, T., Chandler, C. J., et al. 2016, *ApJ*, 821, L16
- Chauvin, G., Lagrange, A.-M., Dumas, C., et al. 2004, *A&A*, 425, L29
- Coudé du Foresto, V., Perrin, G., & Boccas, M. 1995, *A&A*, 293, 278
- Creech-Eakman, M. J., Romero, V., Payne, I., et al. 2016, in *Proc. SPIE*, Vol. 9907, *Optical and Infrared Interferometry and Imaging V*, 990705
- Crespi, A., Lobino, M., Matthews, J. C. F., et al. 2012, *Applied Physics Letters*, 100, 233704
- Davis, K. M., Miura, K., Sugimoto, N., & Hirao, K. 1996, *Optics Letters*, 21, 1729

- Dekker, P., Ams, M., Marshall, G. D., Little, D. J., & Withford, M. J. 2010, *Opt. Express*, 18, 3274
- Diener, R., Minardi, S., Tepper, J., Nolte, S., & Labadie, L. 2016, *Proc. SPIE*, 9907, 990731
- Diener, R., Tepper, J., Labadie, L., et al. 2017, *Opt. Express*, 25, 19262
- Dominik, C. & Tielens, A. G. G. M. 1997, *ApJ*, 480, 647
- Dullemond, C. P. & Monnier, J. D. 2010, *ARA&A*, 48, 205
- Eaton, S. M., Zhang, H., Herman, P. R., et al. 2005, *Opt. Express*, 13, 4708
- Éric Thiébaud & Young, J. 2017, *J. Opt. Soc. Am. A*, 34, 904
- Gatkine, P., Veilleux, S., Hu, Y., Bland-Hawthorn, J., & Dagenais, M. 2017, *Opt. Express*, 25, 17918
- Gattass, R. R., Cerami, L. R., & Mazur, E. 2006, *Opt. Express*, 14, 5279
- Glezer, E. N., Milosavljevic, M., Huang, L., et al. 1996, *Optics Letters*, 21, 2023
- Glindemann, A. 2011, *Principles of Stellar Interferometry* (Springer-Verlag Berlin Heidelberg)
- Goel, K. & Chang, W. 1987, *IEEE Journal of Quantum Electronics*, 23, 2216
- Goldsmith, H.-D. K., Ireland, M., Ma, P., Cvetojevic, N., & Madden, S. 2017, *Opt. Express*, 25, 16813
- Gravity Collaboration, Abuter, R., Accardo, M., et al. 2017, *A&A*, 602, A94
- Greene, T. P. 2001, *American Scientist*, 89, 316
- Gross, S., Jovanovic, N., Sharp, A., et al. 2015, *Optics Express*, 23, 7946
- Gross, S. & Withford, M. J. 2015, *Nanophotonics*, 4, 20
- Hewlett, S. J., Love, J. D., & Steblina, V. V. 1996, *Optical and Quantum Electronics*, 28, 71
- Hillen, M., Kluska, J., Le Bouquin, J.-B., et al. 2016, *A&A*, 588, L1
- Hillenbrand, L. A., Strom, S. E., Vrba, F. J., & Keene, J. 1992, *ApJ*, 397, 613
- Hnatovsky, C., Taylor, R., Simova, E., et al. 2006, *Applied Physics A*, 84, 47
- Hönig, S. F., Watson, D., Kishimoto, M., & Hjorth, J. 2014, *Nature*, 515, 528
- Huélamo, N., Lacour, S., Tuthill, P., et al. 2011, *A&A*, 528, L7
- Hunsberger, R. G. 1982, *Integrated Optics Theory and Technology* (Springer-Verlag New York)
- Itoh, K., Watanabe, W., Nolte, S., & Schaffer, C. B. 2006, *MRS Bulletin*, 31, 620–625
- Johansen, A., Oishi, J. S., Mac Low, M.-M., et al. 2007, *Nature*, 448, 1022

- Kataoka, A., Tanaka, H., Okuzumi, S., & Wada, K. 2013, *A&A*, 557, L4
- Keldysh, L. V. 1965, *JETP*, 20
- Kluska, J., Benisty, M., Soulez, F., et al. 2016, *A&A*, 591, A82
- Kopparapu, R. K., Ramirez, R., Kasting, J. F., et al. 2013, *ApJ*, 765, 131
- Korkishko, A. & Fedorov, V. A. 1999, *Ion Exchange in Single Crystals for Integrated Optics and Optoelectronics* (Cambridge International Science Publishing Ltd), 532
- Kraus, A. L. & Ireland, M. J. 2012, *ApJ*, 745, 5
- Labadie, L., Labeye, P., Kern, P., et al. 2006, *A&A*, 450, 1265
- Labadie, L., Martín, G., Anheier, N. C., et al. 2011, *A&A*, 531, A48
- Labeyrie, A., Lipson, S. G., & Nisenson, P. 2006, *An Introduction to Optical Stellar Interferometry* (Cambridge University Press), 360
- Le Bouquin, J.-B., Berger, J.-P., Lazareff, B., et al. 2011, *A&A*, 535, A67
- Lebouquin, J.-B. J., Berger, J.-P., Labeye, P. R., et al. 2004, in *Proc. SPIE*, Vol. 5491, *New Frontiers in Stellar Interferometry*, ed. W. A. Traub, 1362
- Leinert, C., Graser, U., Przygodda, F., et al. 2003, *Ap&SS*, 286, 73
- Ma, P., Choi, D.-Y., Yu, Y., et al. 2013, *Optics Express*, 21, 29927
- Malbet, F., Kern, P., Schanen-Duport, I., et al. 1999, *A&A*, 138, 135
- Mariotti, J.-M. 1992, *Coherent Combined Instrumentation for the VLT Interferometer*. VLT Report No. 65.
- Martin, G., Heidmann, S., Rauch, J.-Y., Jocou, L., & Courjal, N. 2014, *Optical Engineering*, 53, 034101
- Matter, A., Labadie, L., Augereau, J. C., et al. 2016, *A&A*, 586, A11
- Mayor, M. & Queloz, D. 1995, *Nature*, 378, 355
- McCaughrean, M. J. & O'dell, C. R. 1996, *AJ*, 111, 1977
- Meany, T., Gräfe, M., Heilmann, R., et al. 2015, *Laser & Photonics Reviews*, 9, 363
- Meeus, G. 2011, *Earth, Moon, and Planets*, 108, 45
- Mennesson, B., Millan-Gabet, R., Serabyn, E., et al. 2014, *ApJ*, 797, 119
- Millour, F. 2008, *NewAR*, 52, 177
- Minardi, S., Lacour, S., Berger, J.-P., et al. 2016, in *Proc. SPIE*, Vol. 9907, *Optical and Infrared Interferometry and Imaging V*, 99071N

- Monnier, J. D., Ireland, M. J., Kraus, S., et al. 2016, in Proc. SPIE, Vol. 9907, Optical and Infrared Interferometry and Imaging V, 99071O
- Nowak, M., Lacour, S., Lapeyrère, V., et al. 2016, in Proc. SPIE, Vol. 9904, Space Telescopes and Instrumentation 2016: Optical, Infrared, and Millimeter Wave, 99044L
- Ollivier, M. & Maurel, M. C. 2014, BIO Web of Conferences, 2, 00001
- Osellame, D., Cerullo, G., & Ramponi, R. 2012, Femtosecond Laser Micromachining (Berlin, Heidelberg, Springer-Verlag)
- Osellame, R., Maselli, V., Vazquez, R. M., Ramponi, R., & Cerullo, G. 2007, Applied Physics Letters, 90, 231118
- Parker, J. M. 1989, Annual Review of Materials Science, 19, 21
- Penninckx, D. & Beck, N. 2005, Appl. Opt., 44, 7773
- Petrov, R. G., Malbet, F., Weigelt, G., et al. 2007, A&A, 464, 1
- Pollack, J. B., Hubickyj, O., Bodenheimer, P., et al. 1996, ICARUS, 124, 62
- Renard, S., Malbet, F., Benisty, M., Thiébaud, E., & Berger, J.-P. 2010, A&A, 519, A26
- Ródenas, A., Martin, G., Arezki, B., et al. 2012, Optics Letters, 37, 392
- Saviauk, A., Minardi, S., Dreisow, F., Nolte, S., & Pertsch, T. 2013, Applied Optics, 52, 4556
- Schaffer, C. B., Brodeur, A., & Mazur, E. 2001, Measurement Science and Technology, 12, 1784
- Seddon, A. B. 2011, International Journal of Applied Glass Science, 2, 177
- Shimotsuma, Y., Kazansky, P. G., Qiu, J., & Hirao, K. 2003, Phys. Rev. Lett., 91, 247405
- Snyder, A. & Love, J. 1983, Optical Waveguide Theory, Science paperbacks (Springer US), 391
- Soummer, R., Perrin, M. D., Pueyo, L., et al. 2014, ApJ, 786, L23
- Szemendera, L., Grossard, L., Delage, L., & Reynaud, F. 2017, Monthly Notices of the Royal Astronomical Society, 468, 3484
- Tepper, J., Labadie, L., Diener, R., et al. 2017a, A&A, 602, A66
- Tepper, J., Labadie, L., Gross, S., et al. 2017b, Optics Express, 25
- Toyoshima, M. 2006, J. Opt. Soc. Am. A, 23, 2246
- van Boekel, R., Min, M., Leinert, C., et al. 2004, Nature, 432, 479
- van Uden, R. G. H., Correa, R. A., Lopez, E. A., et al. 2014, Nature Photonics, 8, 865
- Vigreux-Bercovici, C., Bonhomme, E., Pradel, A., et al. 2007, Applied Physics Letters, 90, 011110

Weidenschilling, S. J. 1995, *icarus*, 116, 433

Wyatt, M. C., Panić, O., Kennedy, G. M., & Matrà, L. 2015, *Ap&SS*, 357, 103

Yerolatsitis, S., Harrington, K., & Birks, T. A. 2017, *Opt. Express*, 25, 18713

Youdin, A. N. & Goodman, J. 2005, *ApJ*, 620, 459

Zhao, M., Monnier, J. D., Che, X., et al. 2011, *PASP*, 123, 964



## Acknowledgements

I acknowledge the financial support of this undertaking by the Bundesministerium für Bildung und Forschung (BMBF) through the Advanced Laser Writing for Stellar Interferometry (ALSI) project.

Personally, I would, first of all, like to thank Prof. Lucas Labadie for supervising this work, long but interesting discussions over sometimes apparently trivial and sometimes apparently difficult matter as well as for his professional and personal advices over the last three years. Also, I would like to thank Prof. van Loosdrecht for being second supervisor, Prof. David Gross for serving as president of the committee of the (upcoming) PhD defense and Dr. Nadeen Sabha as the fourth committee member.

During the completion of this thesis, I received lots of valuable scientific advise from the colleagues at PH1 institute. Thank you for this. In particular, for the support during the final phase of this thesis, I would like to thank Juan Andrés Cahuasquí, Fabio Eupen, Balaji Muthusubramanian, Dr. Nadeen Sabha, Dr. Rebekka Grellmann, Dr. Gerold Busch, Dr. Christian Straubmeier, Dr. Álvaro Sánchez-Monge, Thomas Gretzinger and Mathis Börner.

I thank Romina Diener and Dr. Stefano Minardi for the fruitful collaborative work between Cologne and Jena/Potsdam. I also like to thank all secretaries for helping me with travel matters, orders, room bookings et cetera. In particular, I thank Anke Pyschny, Tanja Bodendorf, Stefanie Simon and Mariia Soloviova. I thank Dr. Frank Schlöder for fiddling with IT matters and Falafel King for obvious reasons.

I thank my parents and Karen for having supported me through my studies.



## Selbständigkeitserklärung

Ich versichere, dass ich die von mir vorgelegte Dissertation selbständig angefertigt, die benutzten Quellen und Hilfsmittel vollständig angegeben und die Stellen der Arbeit – einschließlich Tabellen, Karten und Abbildungen –, die anderen Werken im Wortlaut oder dem Sinn nach entnommen sind, in jedem Einzelfall als Entlehnung kenntlich gemacht habe; dass diese Dissertation noch keiner anderen Fakultät oder Universität zur Prüfung vorgelegen hat; dass sie – abgesehen von unten angegebenen Teilpublikationen – noch nicht veröffentlicht worden ist, sowie, dass ich eine solche Veröffentlichung vor Abschluss des Promotionsverfahrens nicht vornehmen werde. Die Bestimmungen der Promotionsordnung sind mir bekannt. Die von mir vorgelegte Dissertation ist von Prof. Dr. Lucas Labadie betreut worden.

Köln, den 22.10.2017

(Jan Tepper)

### Publikationen

Es folgt eine Auflistung der peer-reviewed Publikationen, die dieser kumulativen Arbeit zugrunde liegen. Es sind jeweils die Beiträge der Koautoren, mit Fokus auf den Beiträgen des Promovenden J. Tepper, aufgelistet. Bei allen drei folgenden Beiträgen handelt es sich um peer-reviewed Veröffentlichungen. Die anonymen Referees haben jeweils einige Hinweise zum Manuskript gegeben, die in die endgültige Version mit eingeflossen sind, hier aber unerwähnt bleiben.

- *Integrated optics prototype beam combiner for long baseline interferometry in the L and M bands*; **J. Tepper**, L. Labadie, R. Diener, S. Minardi, J.-U. Pott, R. Thomson and S. Nolte; *A&A* Vol. 602, A66 (2017).

Alle in der Publikation enthaltenen Messungen wurden vom Erstautor J. Tepper durchgeführt und ausgewertet. Der für die Arbeit notwendige optische Aufbau wurde ebenfalls vom Erstautor selbstständig aufgebaut. Die untersuchten Sample wurden von R. Diener, Universität Jena, hergestellt. Die Koautoren haben hilfreiche Kommentare zur Fertigstellung des Manuskripts beigesteuert. Die Erlaubnis zum Abdruck dieser Arbeit ist eingeholt worden und eingefügt.

- *Ultrafast laser inscription in ZBLAN integrated optics chips for mid-IR beam combination in astronomical interferometry*; **J. Tepper**, L. Labadie, S. Gross, A. Arriola, S. Minardi, R. Diener and M.J. Withford; Optics Express Vol. 25, Issue 17, 2017.

Alle in der Publikation enthaltenen Messungen wurden vom Erstautor J. Tepper durchgeführt und ausgewertet. Der für die Arbeit notwendige optische Aufbau wurden ebenfalls vom Erstautor selbstständig aufgebaut. Die untersuchten Sample wurden von S. Gross, Macquarie Universität, hergestellt. Die Koautoren haben hilfreiche Kommentare zur Fertigstellung des Manuskripts beigesteuert. Das Copyright Transfer Agreement der Optical Society (OSA) genehmigt den Autoren die Wiederverwendung in dieser Arbeit.

- *Towards 3D-photonic, multi-telescope beam combiners for mid-infrared astrointerferometry*; R. Diener, **J. Tepper**, L. Labadie, T. Pertsch, S. Nolte and S. Minardi; Optics Express Vol. 25, Issue 16, 2017.

Die experimentellen Ergebnisse wurden von R. Diener in Jena für das zig-zag array und J. Tepper für das ABCD Sample in Köln erzeugt. Die untersuchten Sample wurden von R. Diener, Universität Jena, hergestellt. J. Tepper hat als Koautor mit Kommentaren zur finalen Version des Manuskripts beigetragen. Das Copyright Transfer Agreement der Optical Society (OSA) genehmigt den Autoren die Wiederverwendung in dieser Arbeit.

#### Weitere nicht peer-reviewed Publikationen

- *Advances in broadband-integrated optic beam combiners for mid-IR astronomical interferometers*; **J. Tepper**, R. Diener, L. Labadie, S. Minardi, R. Thomson and S. Nolte; SPIE Proceedings Vol. 10110, Photonic Instrumentation Engineering IV, 2017.
- *Four-channel interferometry with a zig-zag array of mid-infrared integrated waveguides*; R. Diener, **J. Tepper**, S. Nolte, L. Labadie and S. Minardi, SPIE Proceedings Vol. 10106, Integrated Optics: Devices, Materials, and Technologies XXI, 2017.
- *Increasing the spectral coverage of interferometric integrated optics: K/L and N-laser-written beam combiners*; **J. Tepper**, R. Diener, L. Labadie, S. Minardi, B. Muthusubramanian, J.-U. Pott, S. Nolte, A. Arriola, G. Madden, D. Choudhury, W. N. MacPherson and R. Thomson; SPIE Proceedings Vol. 9907, Optical and Infrared Interferometry and Imaging V, 2016.
- *Fringe tracking at longer wavelengths using near- and mid-IR integrated optics devices*; B. Muthusubramanian, L. Labadie, J.-U. Pott, **J. Tepper**, S. Minardi and R. Diener, SPIE Proceedings Vol. 9907, Optical and Infrared Interferometry and Imaging V, 2016.
- *All-in-one 4-telescope beam combination with a zig-zag array of waveguides*; R. Diener, S. Minardi, **J. Tepper**, S. Nolte and L. Labadie; SPIE Proceedings Vol. 9907, Optical and Infrared Interferometry and Imaging V, 2016.

# Astronomy and Astrophysics

Editor in Chief: T. Forveille

## T. Forveille

Astronomy & Astrophysics  
Observatoire de Paris  
61, avenue de l'Observatoire  
75014 Paris, France

Tel.: 33 0(1) 43 29 05 41  
Fax: 33 0(1) 43 29 05 57  
e-mail: [aanda.paris@obspm.fr](mailto:aanda.paris@obspm.fr)  
Web: <http://www.aanda.org>

merging  
Annales d'Astrophysique  
Arkiv for Astronomi  
Bulletin of the Astronomical Institutes  
of the Netherlands  
Bulletin Astronomique  
Journal des Observateurs  
Zeitschrift für Astrophysik  
Bulletin of the Astronomical Institutes  
of Czechoslovakia

Paris, October 19, 2017

## Reprint Permission

### Material:

Article by Tepper et al. 2017, A&A, 602, A66

### To be used in:

PhD thesis, University of Köln

### Permission granted to:

Jan Tepper  
[tepper@ph1.uni-koeln.de](mailto:tepper@ph1.uni-koeln.de)

I hold copyright on the material referred to above, and hereby grant permission for its use as requested herewith.

The article should be reproduced in the same format as that published in A&A (for example, in an appendix). In particular, the present permission rules do not allow copy-and-pasting parts of the article into the main text of the thesis.

Credit should be given as follows:

Credit: Author, A&A, vol, page, year, reproduced with permission © ESO.



Thierry Forveille  
A&A Editor-in-Chief

## Copyright OSA

Dear Jan Tepper,

Thank you for contacting The Optical Society.

For the use of material from **[1]** Jan Tepper, Lucas Labadie, Simon Gross, Alexander Arriola, Stefano Minardi, Romina Diener, and Michael J. Withford, "Ultrafast laser inscription in ZBLAN integrated optics chips for mid-IR beam combination in astronomical interferometry," *Opt. Express* 25, 20642-20653 (2017) and **[2]** Romina Diener, Jan Tepper, Lucas Labadie, Thomas Pertsch, Stefan Nolte, and Stefano Minardi, "Towards 3D-photonics, multi-telescope beam combiners for mid-infrared astrophysics," *Opt. Express* 25, 19262-19274 (2017):

As long as the copyrighted material is included within the body, section or chapter, of the thesis, and is not posted separate from the thesis, OSA considers your requested use of its copyrighted materials to be permissible within the author rights granted in the Copyright Transfer Agreement submitted by the requester on acceptance for publication of his/her manuscript. It is requested that the **Author Accepted** (or preprint) version be the version included within the thesis and that a complete citation of the original material be included in any publication. This permission assumes that the material was not reproduced from another source when published in the original publication.

The **Author Accepted** version is the preprint version of the article that was accepted for publication but not yet prepared and/or formatted by The Optical Society or its vendors.

While your publisher should be able to provide additional guidance, OSA prefers the below citation formats:

For citations in figure captions:

[Reprinted/Adapted] with permission from ref [x], [Publisher]. (with full citation in reference list)

For images without captions:

Journal Vol. #, first page (year published)

An example: *Opt. Express* 25, 19262 (2017)

Let me know if you have any questions.

Best Wishes,

Rebecca Robinson

Rebecca Robinson

October 19, 2017

Authorized Agent, The Optical Society

# Lebenslauf

## Persönliche Angaben

Name: Jan Tepper  
Anschrift: Scheffelstraße 6  
50935 Köln  
Email: tepper@ph1.uni-koeln.de  
Geburtsdatum und -ort: 12.10.1988 in Geseke  
Staatsangehörigkeit: deutsch

## Ausbildung

Jun 2008 Abitur, Städtisches Gymnasium Erwitte  
Okt 2008 - Jun 2011 Bachelor of Science (Physik), Technische Universität Dortmund  
Okt 2011 - Mai 2014 Master of Science (Physik), Technische Universität Dortmund  
Aug 2012 - Dez 2012 ERASMUS Auslandsssemester (Physik, Englisch), Universität Stockholm  
Dez 2014 - Dez 2017 Promotionsstudium (Experimentalphysik), Universität zu Köln

## Berufserfahrung

Okt 2009 - Jul 2012 Tutor und Übungsgrupperleiter, TU Dortmund  
Jan 2013 - März 2013 Praktikant, Infineon Technologies, Warstein  
Sep 2014 - Nov 2014 Associate Consultant, Simon-Kucher & Partners, Köln  
Dez 2014 - Dez 2017 Wissenschaftlicher Mitarbeiter und Übungsgruppenleiter, Universität zu Köln